Technical University of Munich
TUM School of Engineering and Design

Proximate Time Optimal Control for Linear Permanent Magnet Actuators with Speed and Position Estimation

Ali El Hafni

Complete reprint of the dissertation approved by the TUM School of Engineering and Design of the Technical University of Munich for the award of the

Doktor der Ingenieurwissenschaften (Dr.-Ing.)

Chair: Prof. Dr. Jan Torgersen

Examiners:

1. Prof. Dr.-Ing. Dr. h.c. Ralph Kennel
2. Prof. Dr.-Ing. Dieter Gerling
3. Prof. Dr. Marcelo Lobo Heldwein

The dissertation was submitted to the Technical University of Munich on 08.01.2025 and accepted by the TUM School of Engineering and Design on 10.10.2025.

Abstract

This thesis focuses on the control of short-stroke direct current linear actuators with permanent magnet movers for point-to-point motion. These actuators are widely utilized in industrial applications such as refrigeration compressors, valve actuation, and vibration testing. A mathematical model of the actuator is developed, employing a second-order polynomial approximation to represent nonlinear parameters. A novel method is proposed for online estimation of electrical parameters at standstill. Furthermore, speed and position estimation based on induced voltage, and relying solely on current measurement feedback, is investigated for point-to-point motion. A proximate time-optimal nonlinear position controller is cascaded with a linear current controller to achieve fast actuation and soft landing.

Zusammenfassung

Diese Dissertation befasst sich mit der Regelung von Gleichstrom-Linearantrieben mit kurzem Hub und Permanentmagnetläufern für Punkt-zu-Punkt Bewegungen. Solche Antriebe finden häufig Anwendung in der Industrie, beispielsweise in Kältemittelkompressoren, der Ventilsteuerung und der Vibrationsprüfung. Ein mathematisches Modell des Antriebs wird entwickelt, wobei die nichtlinearen Parameter durch eine Näherung mittels eines Polynoms zweiten Grades beschrieben werden. Eine neuartige Methode zur Online-Schätzung der elektrischen Parameter im Stillstand wird vorgeschlagen. Darüber hinaus wird ein Ansatz zur Geschwindigkeits- und Positionsschätzung untersucht, der ausschlielich auf induzierter Spannung basiert und durch Strommessungen korrigiert wird, um Punkt-zu-Punkt-Bewegungen zu realisieren. Ein nahezu zeitoptimaler nichtlinearer Positionsregler wird mit einem linearen Stromregler kaskadiert, um eine schnelle Betätigung und eine sanfte Landung zu erreichen.

Contents

Abstract iii

Zusammenfassung v

Contents vii

List of Figures xi

List of Tables xv

Acronyms xvii

1 Introduction 1
- 1.1 Electromechanical Actuation . . . 1
- 1.2 Aim of the Project . . . 5

2 State of the Art 7
- 2.1 Linear Electromagnetic Actuators . . . 7
  - 2.1.1 Design and Applications . . . 7
    - 2.1.1.1 Loudspeaker Systems . . . 8
    - 2.1.1.2 Valve Actuators . . . 9
    - 2.1.1.3 Compressors . . . 9
    - 2.1.1.4 Power Control and Protection . . . 11
    - 2.1.1.5 Vibration Testing . . . 11
- 2.2 Control of Linear Electromagnetic Actuators . . . 12
  - 2.2.1 Soft Landing . . . 13
  - 2.2.2 Sensorless Control . . . 13

3 Actuator Modelling 17
- 3.1 Coils and Magnets . . . 17
  - 3.1.1 Coils . . . 17
  - 3.1.2 Permanent Magnets . . . 20
  - 3.1.3 Coil Magnet Equivalence . . . 22
  - 3.1.4 Forces . . . 22
    - 3.1.4.1 Excitation Force . . . 22
    - 3.1.4.2 Reluctance Force . . . 29
    - 3.1.4.3 Cogging Force . . . 32

3.2 Hybrid Model 32
3.2.1 Analytical Model 32
3.2.2 Finite Element Method (FEM) Model 33
3.3 Excitation 41
3.3.1 Single Phase Voltage Source Inverter 41
3.3.2 Pulse Width Modulation (PWM) 42
3.3.3 Deadtime 43
3.3.4 Exponential Response 44
3.4 Disturbances and Load 46
3.4.1 Friction 46
3.4.2 Eddy Current Damping Force 47
3.4.3 Load Forces 48

4 Test Bench **51**
4.1 Physical Setup 51
4.1.1 Actuator 51
4.1.2 Inverter 52
4.1.3 Control System 52
4.1.4 Position Sensor 53
4.2 Measurements 56
4.2.1 Static Inductance Measurements 56
4.2.2 Static Force Measurements 57
4.2.3 Force/Back electromotive force (e.m.f.) Constant 58

5 Parameter and State Estimation **63**
5.1 Electrical Parameters 63
5.2 Force Constant Approximation 65
5.3 Damping Coefficient 66
5.4 Speed Estimator 68
5.4.1 Speed Estimation from Position Sensor 69
5.4.1.1 Linear Regression 69
5.4.1.2 Kalman Filter 70
5.4.2 Speed Estimation from Actuator Model 72

6 Controller Design **75**
6.1 Linear Control 75
6.1.1 Cascaded Control 76
6.1.2 State Space Control 77
6.1.3 Trajectory Generation 77
6.2 Time Optimal Control 79
6.2.1 The Double Integrator 79
6.2.2 Proximate Time Optimal Control 80
6.2.3 Proximate Time Optimal Control of the Actuator 83

6.3 Experimental Results 85
6.3.1 Position Control with Position Sensor 85
6.3.2 Position Control without Position Sensor 87

7 Conclusion and Future Work 89

Bibliography 91

A Appendix 97
A.1 Exponential Model 97
A.2 Elliptic Integrals 98
A.2.1 General Form of Elliptic Integrals 98
A.2.2 Types of Elliptic Integrals 98
A.2.3 Complete Elliptic Integrals 99
A.2.4 Applications 99

List of Figures

1.1 Growth of electric motors usage in the automotive sector in the performance related category. 2
1.2 Electric motors in automotive applications. 2
1.3 Diagram of an engine showing the camshaft, valves, and pistons. 3
1.4 Shock absorber. 4
1.5 Bose automobile suspension system. 4

2.1 Transforming a rotating induction motor to a linear one [1]. 8
2.2 Illustration of a Loudspeaker. 9
2.3 Electromagnetic valve for mass flow control. 10
2.4 Electromagnetic gas exchange actuator for internal combustion engines [2]. 10
2.5 Inverter Linear Compressor from LG [3]. 11
2.6 Relay principle: 1. Coil, 2. Armature, 3. Moving contact [4]. 12
2.7 CAD drawing of the designed actuator [5]. 12
2.8 Diagram of a field oriented controller. 14

3.1 2D drawing of the actuator. 18
3.2 Magnetic field around a current carrying wire. 18
3.3 Magnetic field created by a current carrying loop. 19
3.4 A coil composed of several loops in the axial and radial direction. 20
3.5 Coil in a magnetic circuit. 21
3.6 Hysteresis curve of a hard magnetic material. 21
3.7 Modelling a permanent magnet in a magnetic circuit. 22
3.8 Equivalence between coils and magnets. 23
3.9 Two current carrying loops. 25
3.10 Force on current carrying loop due to a magnetic field from another loop. 25
3.11 Coil and magnet representation using the filament or the shell method. . . 28
3.12 Force on magnet moving between two coils. 29
3.13 Simple magnetic circuit to illustrate the reluctance force. 30
3.14 Axi-symmetric 2D Model of the E core actuator. 34
3.15 Results of an FEM simulation of the E core actuator showing flux density. 35
3.16 Self, mutual flux linkage, and flux linkage due to the permanent magnet in each coil when 1 A current is flowing. 35
3.17 Total inductance of the actuator. 36
3.18 Total reluctance force acting on the actuator as a function of current and position. 37
3.19 Cogging force acting on the actuator as a function of position. 37

3.20 Excitation force due to each coil and their sum acting on the mover when 1 A (left) and −1 A (right) current is flowing through the coils. 38
3.21 Total excitation force acting on the actuator as a function of current and position. 39
3.22 High level model of the actuator with the three subsystems, electrical, magnetic, and mechanical. 39
3.23 Electrical subsystem. 40
3.24 Signal flow diagram of the actuator. 40
3.25 Single phase voltage source inverter. 41
3.26 Switching legs of a single phase PWM inverter and the resulting voltage. . 43
3.27 Switching legs of a single phase PWM inverter and the resulting voltage with deadtime assuming positive current. 44
3.28 Switching legs of a single phase PWM inverter and the resulting voltage with deadtime assuming negative current. 45
3.29 Qualitative illustration of the friction force as a function of speed. 47
3.30 Damping force due to induced eddy currents. 48
3.31 Gravitational load force as function of speed. 49
3.32 Actuator driving a piston in a cylinder. 49
3.33 Load force acting on a piston compressing gas as a function of displacement. 50

4.1 Stator (left) and the moving magnet (right). 51
4.2 Mechanical setup of the actuator. 52
4.3 Test bench showing from a top view the actuator and the PWM inverter. 53
4.4 Illustration of the control system. 54
4.5 Signal flow between processor and FPGA. 54
4.6 Simple schematic of an Linear Variable Differential Transformer (LVDT). 55
4.7 Inductance vs. position for different excitation frequencies. 57
4.8 Force on the mover when the actuator is excited with a constant current of 2 A. 58
4.9 Force on the mover for different positive current excitation values. 59
4.10 Force on the mover for different negative current excitation values. 59
4.11 Force and inductance for different mover positions. 60
4.12 Induced voltage due to external movement. 60
4.13 Force constant (black) from the static force measurements and back e.m.f. constant (red) from the voltage measurements. 61

5.1 Current response in one PWM period at standstill. 64
5.2 Results of the electrical parameter estimation. 65
5.3 Measured force constant (calculated from the static force measurements) and the result of the curve fitting using a second order polynomial. 67
5.4 Real and estimated position based on the estimated damping coefficient. . 69
5.5 Kalman gain matrix parameters. 72
5.6 Comparison of speed estimation of a noisy position signal between the Kalman Filter and linear regression. 73

6.1 Closed loop position control signal flow diagram. 76
6.2 Cascaded position, speed, and current controller. 77
6.3 State space controller. 78
6.4 The double integrator system. 80
6.5 Signal flow diagram of the time optimal control of the double integrator. . 80
6.6 Time optimal simulation of the double integrator system. 81
6.7 Time optimal simulation of the damped double integrator system. 81
6.8 Signal flow diagram of the Proximate Time Optimal Control of Servomechanisms (PTOS) control of the double integrator. 82
6.9 Time optimal (red) vs. PTOS (blue) of the double integrator system. . . 83
6.10 Simulation of PTOS for different values of α (red $\alpha = 0.9$, blue $\alpha = 0.8$, green $\alpha = 0.7$). 84
6.11 Cascaded PTOS position and speed controller, and current PI controller. 84
6.12 Comparison of the results of the two controllers for the up cycle (PTOS in red, LQR in blue, position reference in black). 85
6.13 Comparison of the results of the two controllers for the down cycle (PTOS in red, LQR in blue, position reference in black). 86
6.14 Comparison of the two controllers with estimated position as feedback (PTOS in red, LQR in blue, position reference in black). 87

List of Tables

3.1 Coil and magnet parameters for Figure 3.12. 30
3.2 Analogy magnetic and electric circuits. 31

4.1 Electrical and mechanical ratings of the actuator. 52

5.1 Estimated damping coefficient for different excitation currents. 68

6.1 Procedure to find t_f. 79

Acronyms

AC	Alternating Current.
AMB	Active Magnetic Bearing.
DC	Direct Current.
e.m.f.	electromotive force.
EKF	Extended Kalman Filter.
FEM	Finite Element Method.
FOC	Field Oriented Control.
FPGA	Field Programmable Gate Array.
LTI	Linear Time Invariant.
LVDT	Linear Variable Differential Transformer.
MB	Magnetic Bearing.
MRAS	Model Reference Adaptive System.
PID	Proportional Integral Derivative.
PMSM	Permanent Magnet Synchronous Motor.
PTOS	Proximate Time Optimal Control of Servomechanisms.
PWM	Pulse Width Modulation.
SISO	Single Input Single Output.

1 Introduction

This chapter gives a brief background as well as the aim of this project and the contributions of the thesis.

1.1 Electromechanical Actuation

The noun Actuation is derived from the verb actuate which means "to put into mechanical action or motion" [6]. Since the early nineties a shift from pure mechanical actuation to electromechanical actuation started to formulate. Design engineers were able to improve the performance of their systems by integrating as much electronics as possible. This was facilitated by the fast development of computers, processors, and sensors with regards to increase of execution speed and decrease in costs. A very nice example of that is the Williams FW15C Formula 1 car built by Williams Grand Prix Engineering for the 1993 Formula 1 season [7]. Compared to the other cars during that season, this car featured advanced electronic systems such as active suspension, anti-lock brakes, traction control, telemetry, fly-by-wire controls, pneumatic valve springs, power steering, semi-automatic transmission, a fully automatic transmission and also continuously variable transmission. The racing driver who drove it that season called it "a little Airbus". This came out as a result of Formula 1 being a high performance sport with a lot of funding for research. After their success in motorsports these new technologies start expanding into the consumer section.

The automotive sector is perhaps the best example of the shift from mechanical to electromechanical actuation where the use of electric motors in a car continues to rise constantly, especially with recent emergence of road legal electric vehicles [8]. Figure 1.1 shows the different applications of electric motors in automotive with some examples for each application while Figure 1.2 shows the increase in the usage of electric motors for performance related applications in the automotive industry where a 7% increase in global demand between 2008 and 2012 is reported [8]. As more and more full electric and hybrid vehicles emerge on the road, the global demand for electrical actuation will continue to increase. This will be backed up by the constant increase in performance of processors and decline in costs.

Mechanical actuation by itself has been passive in nature. One example is valve actuation. Valves in combustion engines are mounted on top of cylinders to let fuel in or exhaust gas out. Traditionally, a cam shaft rotates together with the rotation of the engine through a belt connection and exerts a force on the head of one of the valves causing it to open for a fraction of a second. By positioning the actuating part of the shaft at different places around the circumference, the valves are actuated at different timings synchronized with the movement of their cylinder. This is illustrated in Figure

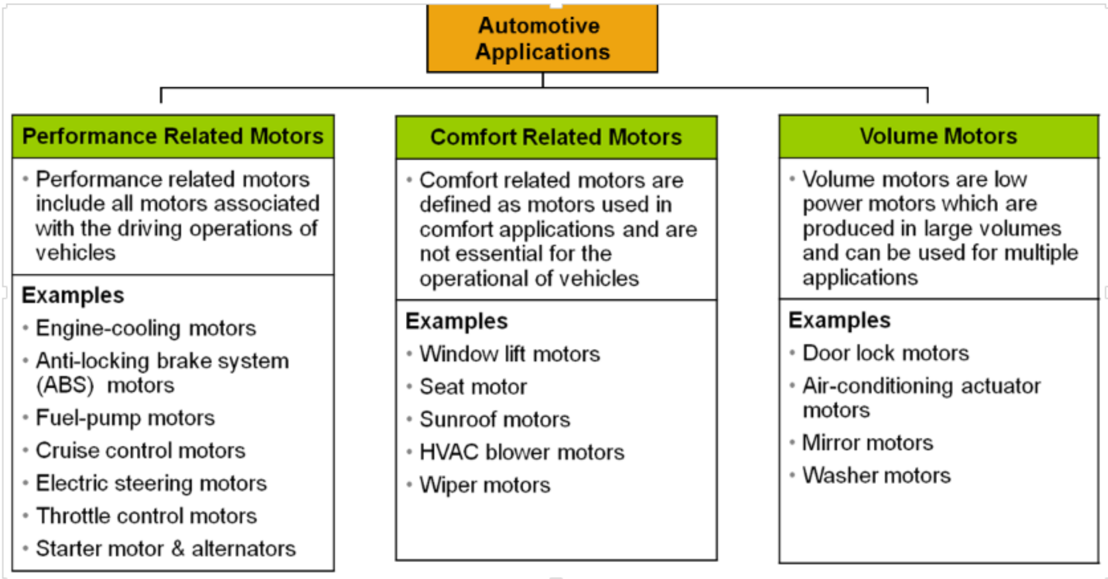

Figure 1.1: Growth of electric motors usage in the automotive sector in the performance related category.

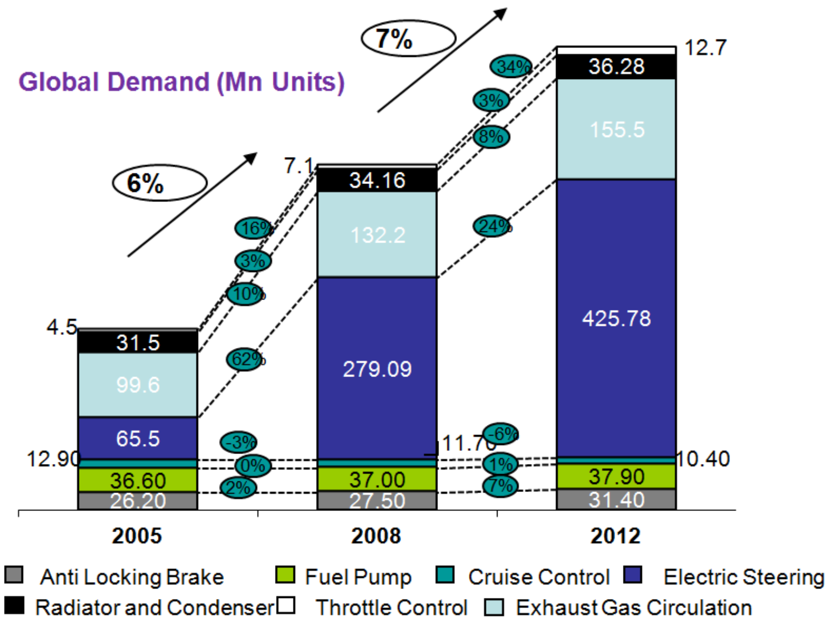

Figure 1.2: Electric motors in automotive applications.

1.3 [9]. It is clear that there is no feedback control on the movement of the valves (this is the mechanical equivalent of an open loop controller) rendering them vulnerable to external conditions and mechanical wear.

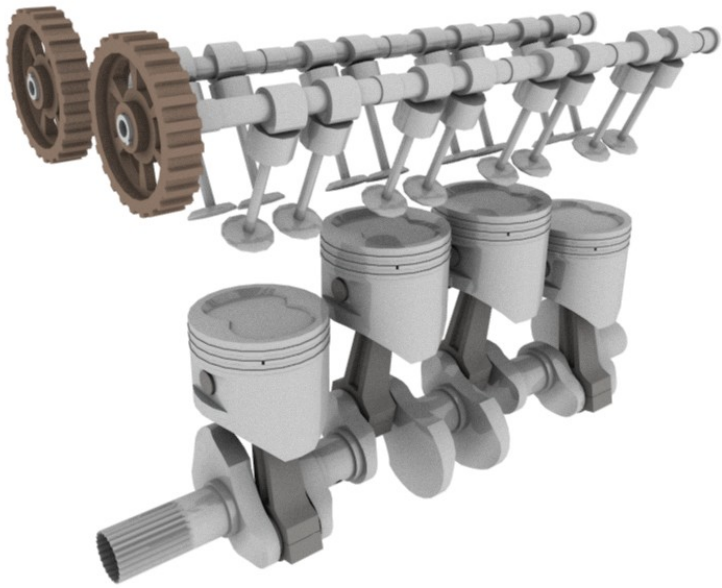

Figure 1.3: Diagram of an engine showing the camshaft, valves, and pistons.

Another example is the shock absorber of a car. Its main function is to smooth the ride through absorbing shocks due to uneven roads. In addition to that, it aims to keep the car body from rolling and pitching excessively as well as maintaining good contact between the tire and the road. Figure 1.4 shows a model of a shock absorber [10].

Nowadays, research has been going on to convert the passive suspension system to a semi-active or a full-active suspension. One leader in this area is the Bose Corporation, famously known for their high quality sound systems. Bose has been for the last 24 years working on a fully active suspension system based on electromagnetic actuators presented in Figure 1.5. A linear electromagnetic actuator is mounted on each wheel. By reading data from sensors and using power amplifiers, the actuators can be made to react to nonuniformities in the road such as bumps and potholes creating a comfortable and smooth ride. Not only that, in cases where the suspension system has to absorb shocks, the actuator acts as a generator and energy is fed back to the supply making the whole system energy efficient. This combination of sensor feedback and actuation gives the driver freedom to tune the system, for example choosing between comfort and sport modes.

There are many other examples, whether in research in academia or in industry, that illustrate this general move from passive pure mechanical actuation to semi-active or fully active actuation by integrating electromagnetic systems together with sensing and amplification.

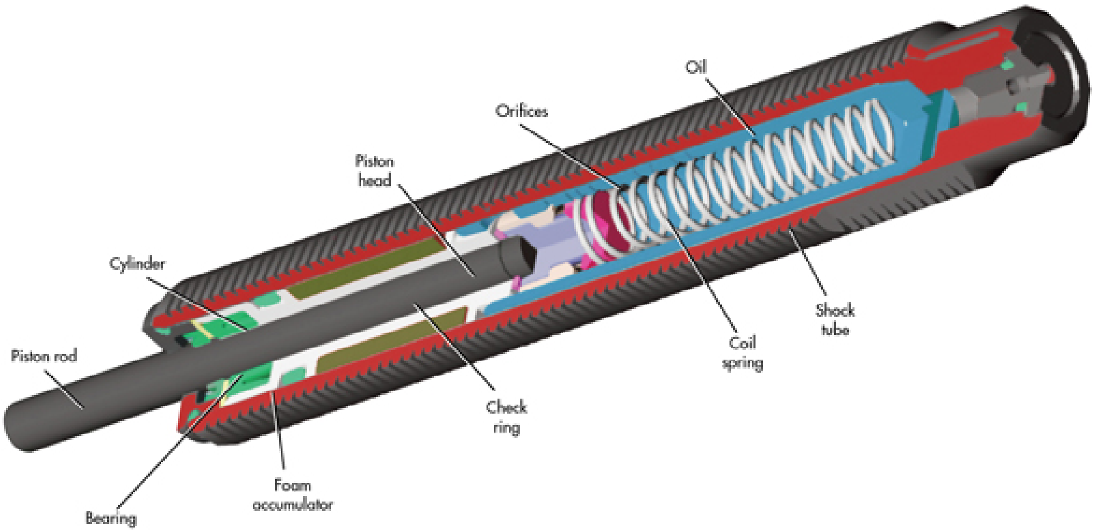

Figure 1.4: Shock absorber.

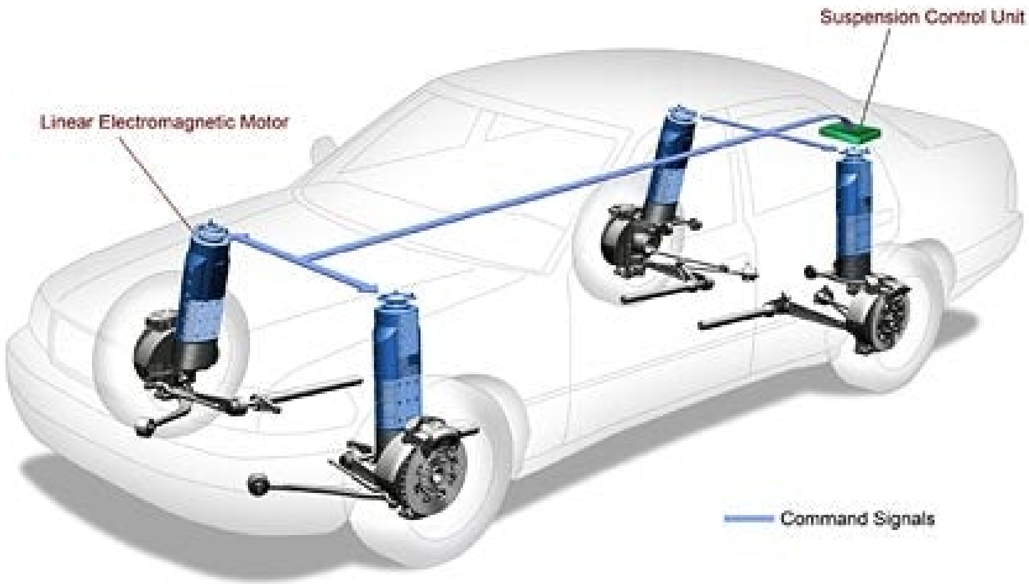

Figure 1.5: Bose automobile suspension system.

1.2 Aim of the Project

Electromagnetic actuators come in different types based on the mover type (moving magnet, moving coil, moving iron), excitation voltage whether Direct Current (DC) or Alternating Current (AC), and movement range. The moving iron type, known in the industry as the solenoid actuator, has a coil as the stator and a plunger as the mover and operates based on the reluctance force. The advantage is the small weight of the mover; on the other hand, movement can be actuated only in one direction and the return force has to be supplied by a spring. Permanent magnet actuators use a permanent magnet either for the mover or for the stator, and operate based on the Lorentz force principle. The advantages of these actuators are the high forces, and the controllability over the whole stroke range in both directions of movement. The disadvantage of the moving magnet type is the weight of the mover. Without feedback control, these actuators can be controlled in a simple on/off or switch manner. The drawback of on/off control is the mechanical wear due to the high velocity impacts the actuator experiences when closed or opened. Since electromagnetic actuation is a general term, from here on electromagnetic actuators refer to linear motors excited mainly by a DC voltage to provide force and movement in a single axis.

The aim of this project is to design a feedback control system for the permanent magnet type linear actuator so that high dynamics can be maintained without increasing mechanical wear and at the same time gain freedom on the control cycle. The requirements on the controller are minimum time transition from one end of the stroke to the other and minimum impact speed which is also referred to as soft landing. Since position sensors add cost and complexity to the system as well as negatively affect the robustness of the system (it has been shown that in electromagnetic actuation, the position sensor is most likely to fail [11]), removing the sensor would bring great cost and robustness benefits. Therefore a second aim of the project was to study whether it is possible to achieve the mentioned requirements without a position sensor.

2 State of the Art

In this chapter, in the first section an introduction to linear electromagnetic actuators will be given. Except for the well industry known solenoid actuator, linear actuators come in many different designs. Therefore, the most common designs will be presented without going deep into each and everyone of them. This will be reserved to the next chapter, where the design and characteristics of the actuator under study will be presented.

In the second section, a literature review on sensorless control is presented. Since sensorless control for rotating AC machines comprises close to 90% of the literature, it would not be fair not to have a dedicated part for it in this thesis.

2.1 Linear Electromagnetic Actuators

In general, electrical machines with movement (to distinguish them from transformers which are also electrical machines) can be translating or rotating. Linear actuators are electrical machines where the mover moves in a linear fashion instead of rotational. In other words, a linear machine is the equivalent of a rotating machine with the stator and rotor cut and rolled on a straight. This concept is illustrated in Figure 2.1. The linear machine can now be regarded as a rotating machine with an infinitely large radius [12].

Thus linear actuators come in many different types and designs (DC, synchronous, and asynchronous) [13]. Compared to their rotating counterparts, the design of linear actuators tends to be more application dependent. In this section, the actuators are divided into different categories based on their design and operating principles.

2.1.1 Design and Applications

Translational motion can often be achieved through direct actuation and without any gear to translate the motion (e.g. rack and pinion). This reduces the costs of linear actuators and makes them more efficient [13]. Different designs of linear actuators differ from each other mainly in the type of force responsible for actuation. There are two main forces which can act on a mover: the reluctance force and the force due to the interaction between two magnetic fields. The actuators commonly found in the industry can be split based on these two principles: the solenoid actuator (based on the reluctance force) and the voice coil actuator (based on the interaction between two magnetic fields). Another group of actuators is the piezoelectric actuator, typically used for very high frequency and small stroke range applications.

Reluctance forces are always present in actuators. Whether they contribute to the main force or work against it depends on the design of the actuator. They arise due to the nature of magnetic fields. A magnetic field will try to take the path with least

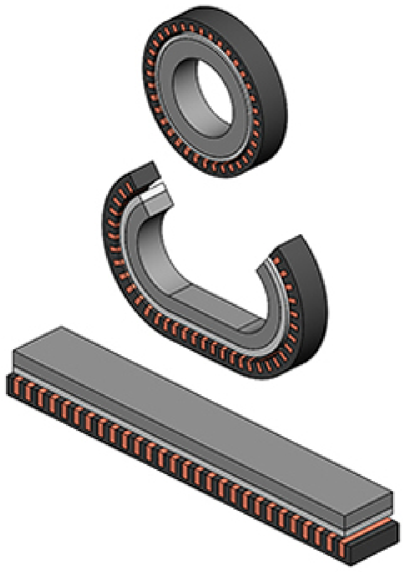

Figure 2.1: Transforming a rotating induction motor to a linear one [1].

reluctance and because the reluctance of air is much higher than that of ferromagnetic material the field will try to minimize the air gap leading to a force acting on the moving plunger.

The other type of forces are forces due to the interaction between two magnetic fields. Opposite magnetic polarities attract while similar polarities repel. A magnetic field is induced either from a current carrying conductor or from a magnetized hard magnetic material. Since the direction and magnitude of a magnetic field produced from a current carrying conductor are controllable, these actuators have the advantage of inducing force in both directions.

2.1.1.1 Loudspeaker Systems

To produce sound waves, a membrane has to vibrate at a high frequency. Thus, electrical energy has to be transformed to mechanical energy and this is where an electrodynamic actuator comes in place. Since in loudspeaker systems movement has to be controlled in both directions, electrodynamic, or voice coil actuators are used. These work on the principle of the interaction of two magnetic fields. Figure 2.2 shows a rough illustration of a typical loudspeaker or a moving coil actuator. The moving membrane is fixed to the coil and together they form the moving part of the actuator. The stator is comprised of a permanent magnet housed in a ferromagnetic structure. If the coil is excited with current, a magnetic field is induced. This magnetic field interacts with the magnetic field from the permanent magnet to produce force which acts on the moving coil. By controlling the amplitude and direction of the current, the movement of the membrane can be controlled to produce the desired sound.

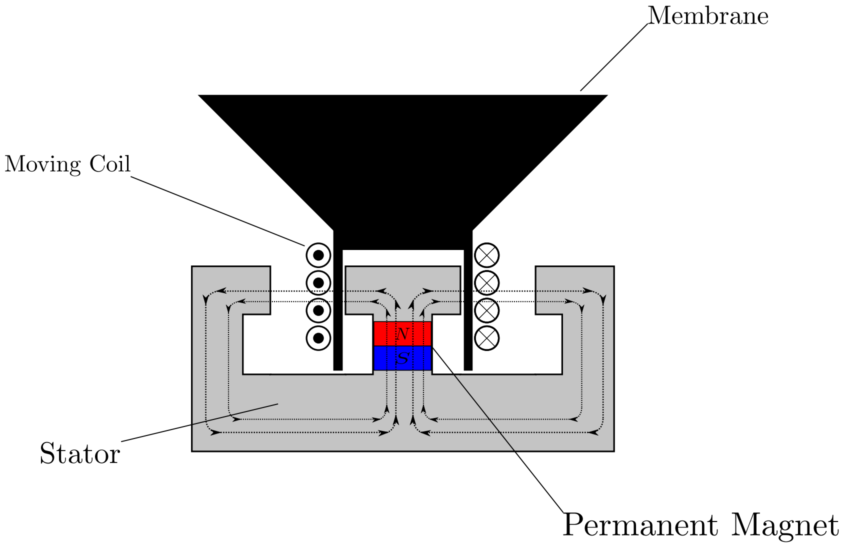

Figure 2.2: Illustration of a Loudspeaker.

2.1.1.2 Valve Actuators

Linear actuators are also used to regulate the flow of liquids and gases in the form of valve actuators. In [14], an optimal design for a mass flow controller based on a solenoid actuator to improve the response characteristics and efficiency is presented. The mass flow controller is used in applications where an accurate gas flow must be controlled and is composed of three parts: flow sensor, valve and controller. The heart of the valve actuator is an electromagnetic linear actuator which controls the error between the required and real mass flow rate. The setup is shown in Figure 2.3.

In [2], a variable valve timing actuator for fluid exchange control in internal combustion engines is presented along with an advanced control algorithm. Traditional valve control in internal combustion engines is purely mechanical where the valve train is directly connected to the camshaft and rotates with the rotation of the motor which leads to a loss of freedom on the opening and closing cycles of the valves. By using solenoid actuators, one has total control on the valve cycles as well as higher dynamics and lower mechanical wear. The design in [2] is shown in Figure 2.4. Two electromagnets, above and below the armature, are for holding the valve in the open and close position respectively, where as the valve is held in the equilibrium position by a spring when the electromagnets are not energized.

2.1.1.3 Compressors

Compressors used in refrigeration applications have also started the transformation from using rotational to translational motors. This was predicted since compressors are basically reciprocating machines. If a rotating machine is used, movement has to be mechanical transformed from rotating to translating which increases losses and decreases

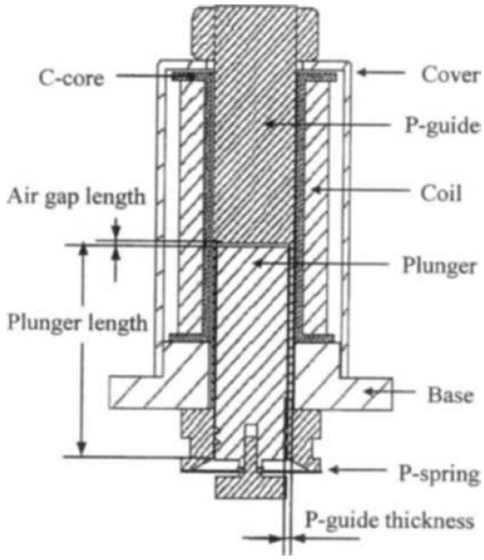

Figure 2.3: Electromagnetic valve for mass flow control.

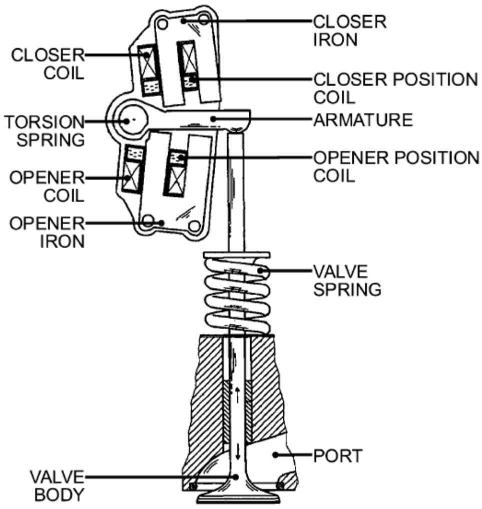

Figure 2.4: Electromagnetic gas exchange actuator for internal combustion engines [2].

efficiency. By employing linear actuators, these losses can be massively reduced due to reduction in mechanical complexity.

One of the biggest consumer electronics manufacturer, LG, has produced one of first linear compressors for their refrigeration products [3]. The new technology termed Inverter Linear Compressor technology, is according to the Association for Electrical, Electronic and Information Technologies (VDE) 32% more efficient compared to traditional compressors as well as 25% quieter. The design of the new compressor is shown in Figure 2.5.

Figure 2.5: Inverter Linear Compressor from LG [3].

2.1.1.4 Power Control and Protection

Another area of applications for linear actuators is power protection such circuit breakers, relays, and contactors. Circuit breakers are used to cut current supply, for example in the case of an emergency or for over-current protection. Contactors and relays serve the same purpose but in response to a command from control electronics. They are all mainly based on solenoid actuators. A coil is energized which leads to a reluctance force acting on an armature. The force moves the armature in a way that a circuit is closed and current can flow. A mechanical spring acts against the armature so that when the coil is not energized the circuit is open. This is illustrated in Figure 2.6.

2.1.1.5 Vibration Testing

In [5], the design of a linear actuator for vibration testing for automotive applications is presented. The stator is made up of two coils and four permanent magnets and the

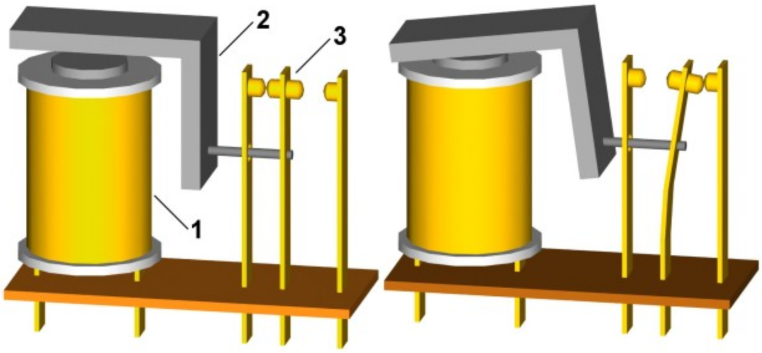

Figure 2.6: Relay principle: 1. Coil, 2. Armature, 3. Moving contact [4].

mover is made up of two plates connected together. The designed actuator is shown in Figure 2.7. Since the reluctance force is only an attractive force, the plates can be moved by energizing one of the coils at the same time. Having two coils give the possibility for a movement in both directions.

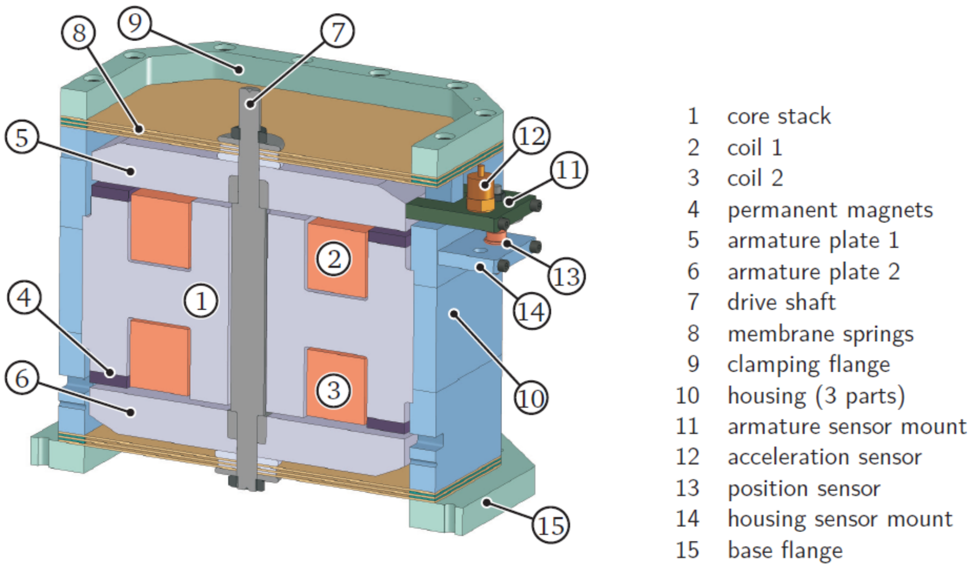

Figure 2.7: CAD drawing of the designed actuator [5].

2.2 Control of Linear Electromagnetic Actuators

In this section, a literature review on the control of linear electromagnet actuators will be presented with emphasis on position control for soft landing and sensorless control.

2.2.1 Soft Landing

This work deals with control of linear actuators for point to point motion control. The requirements for such applications is to realize a certain motion profile of the mover between two fixed points (for example, the opening and closing of a valve actuator). One such requirement would be shortest travel time with minimum speed impact, meaning the mover should travel from one end to the other in the shortest time possible and at the same time reach the end point with minimum speed possible to minimize impact. This is due to the fact that high impact leads to higher noise and faster mechanical wear. This is called "soft landing" [15] since the moving part "softly" lands on its end position.

Flatness based control or tracking is one of the most implemented method in literature to achieve soft landing [2, 16, 17, 18]. The common approach is to generate the required trajectories based on flatness for the output, states, and input of the actuator, and to control using two degree of freedom controller (feedforward and feedback) the actuator to follow the trajectory and reject disturbances. The disadvantage of this approach is the requirement of a good model of the actuator, often not a simple task due to the nonlinearities as well as parameter change during operation. In [15], iterative learning control is implemented to achieve soft landing of electromechanical actuators in camless engines. This is a well suited method for reciprocating applications. The downside of such methods are the high implementation complexity when the controller is implemented on low cost industrial microcontrollers.

In [19], model predictive position control is used for linear actuators in automotive applications. Model predictive control for electric drives is an attractive approach due to its flexibility in integrating the requirements in the cost function [20]. Methods such as the finite set model predictive control [21] make use of the discrete nature of DC-DC converters needed to apply a controllable input voltage on actuators. The disadvantage of the model predictive control is again the requirements of a very good model, in addition to powerful microcontrollers.

2.2.2 Sensorless Control

Sensorless control for electric drives has been an ongoing research topic for more than three decades now. As new control methods for rotating electric motors emerged, the requirements for feedback from the motor also increased. Perhaps the most utilized feedback control method for rotating electric motors is the Field Oriented Control (FOC). In FOC, an AC motor can be controlled like a DC motor. Figure 2.8 shows the basic structure of an FOC controller [22]. Without going deep into the control structure, it is just important to show that feedback of current and position of the motor is essential for the controller to work. This requires that at least two current sensors be installed (to measure two of the three phase currents of the motor since the third phase current can be calculated from the other two) and one position sensor, also called an encoder or resolver [23] which feeds back the current position of the rotor. Current sensors are very robust and usually installed inside the 3-phase inverter. Position sensors on the other hand require special installation and care since they are installed on the machine and attached to the rotor. This makes them vulnerable to the environment surrounding the machine such high temperatures, humidity, vibrations or damage. In addition to that, the extra cost they bring to purchase and install them has led researchers and the industry to look for alternatives.

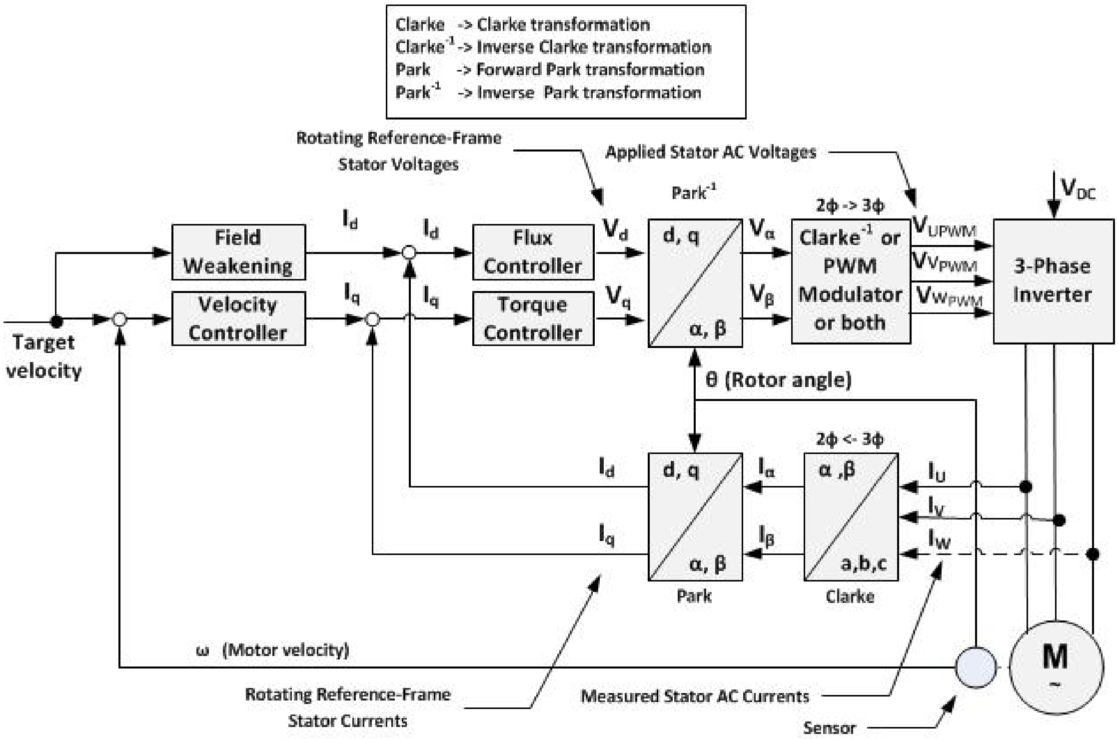

Figure 2.8: Diagram of a field oriented controller.

The term sensorless control is not agreed upon from all groups since technically a current sensor is still present. There are other terms such as transducerless position estimation [24] or self-sensing [25] since the machine itself is used as a resolver. In this thesis, the term sensorless control will be mainly used.

In general, sensorless control or position estimation methods can be split into two main categories: model based estimation and saliency based estimation. As the name says, model based estimation methods rely on a mathematical model of the machine. Based on the input and states (mainly current speed and position) at the current time instant the states of the motor for the next time state are predicted. Since there are always mismatches between the physical and mathematical model of a plant there will be errors between the real and estimated states. These are then corrected by measuring the measurable states by feeding back the error to a controller with a certain gain. When the error goes to zero, the real and estimated states are the same, and the speed and position can be used as feedback to the main controller (for example FOC). The most famous model based estimators are the Luenberger Observer [26], Extended Kalman

Filter (EKF) [27], and Model Reference Adaptive System (MRAS) [28]. Such methods are mainly back e.m.f. estimators from which the speed can be directly calculated due to the direct relation between them and the position can be calculated through integration. The shortcoming is that at low to zero speed ranges the back e.m.f. signal to noise ratio is too small so that the speed and position cannot be estimated. This is where the other group of estimators are used.

Saliency based estimation methods rely on the position dependent magnetic characteristics of the motor (such as inductance) to estimate the position. These methods are always linked with a high frequency injection scheme where an extra high frequency low amplitude signal is used to excite the machine (in addition to the main torque or force producing signal) after which the resulting current response is demodulated and the position dependent characteristics are extracted from which the position is estimated. This mapping from inductance to position allows the position to be estimated even at standstill or low speed conditions where the model based methods fail.

Sensorless control for electric drives has been around for almost three decades now. Key estimation methods for zero to low speed ranges such as the "INFORM" method [29], or the high frequency injection methods [24, 30] have been developed and improved throughout the years. In [31], a comprehensive review of sensorless control for rotating electrical machines is presented. For high speed regions, a model based estimator such as the famous Kalman filter can be used.

Compared to rotating electrical machines, sensorless control for electromagnetic linear actuators is not very abundant in literature. Rahman et al. [32] were the first ones to investigate position estimation for solenoid actuators. A dedicated circuit is designed to measure the current rise $\frac{di}{dt}$ in a PWM period, which depends on the inductance which itself depends on the position. Through measurements of voltage, current, and current rise, the inductance is estimated and with the help of a lookup table is matched to the position of the mover. Experimental results are provided for a frequency of 1 Hz. The main drawback of this method is the additional dedicated circuit. In [33], an external capacitor is connected to the coil (between one terminal and ground) making the coil circuit an LC circuit, and by measuring the phase difference between the main exciting voltage signal and the capacitor voltage, inductance variation can be estimated since at resonant frequency this phase difference depends heavily on the inductance. Maridor et al. [34] proposed to excite the actuator with an additional high frequency signal at a frequency equal to the resonance frequency of the actuator, at which the change of impedance vs. position is the highest. The amplitude of the current signal is then estimated by first calculating the average over a window and taking the sum of square difference between the value at each time instant and the calculated average. This sum of square represents then the position. In [35], a similar scheme is proposed where the main difference is in the hardware used for excitation. In [36], one coil is energized with the fundamental excitation while the other coil is excited with a high frequency signal. Then a reduced order observer is designed to estimate the position dependent resistance. In [37], a two stage sliding mode observer is proposed for sensorless control of an electromagnetic valve actuator. The observer is a high gain observer which reduces the effects of uncertainties in the model of the actuator as well as external disturbances. In [38], the same author proposes to combine a position observer and velocity estimator. The Lyapunov approach is used to design the position observer while the velocity estimator is a model based estimator.

3 Actuator Modelling

In this chapter, a model of the actuator under study will be presented. The modelling will mainly rely on FEM, although an analytical explanation based on a simplified geometry will be given where possible. The FEM model was built based on the limited information about the actuator provided by the original manufacturer as well as a patent [39] describing the actuator itself.

Figure 3.1 shows a front view sketch of the actuator. As mentioned before the actuator is made up of two coils housed in a cylindrical stator. The coils are connected in anti-series, i.e. the same current flows in both coils but in opposite direction (as shown in the figure). Thus each coil forms an electromagnet by itself, and based on the direction of the current in the coil, the permanent magnet mover is attracted by one coil and repelled by the other doubling the force acting on the mover compared to when there is only one coil. The stator has a cylindrical shape and is made of ferromagnetic material. The mover is composed of a cylindrical permanent magnet with axial magnetization as well as mover back iron (also called pole shoes) composed of ferromagnetic material. The pole shoes help to shape the flux from the permanent magnet to increase the thrust of the actuator.

3.1 Coils and Magnets

We start with main elements of the actuator: the coils in the stator, the magnet in the mover, and the ferromagnetic material in the stator and mover.

3.1.1 Coils

A current carrying conductor will produce a magnetic field around it according to Ampere's circuital law

$$\nabla \times \mathbf{B} = \mu_0 \cdot \mathbf{J}, \tag{3.1}$$

where $\mathbf{B}$ is the magnetic field density, $\mathbf{J}$ is the current density, and μ_0 is the magnetic permeability of free space. The direction of the field is according to the right hand rule and is shown on Figure 3.2.

The magnitude of a magnetic field created around an infinitely long wire is given by

$$B = \frac{\mu_0 I}{2\pi r}, \tag{3.2}$$

where I is the current in the wire and r is the radial distance to the wire.

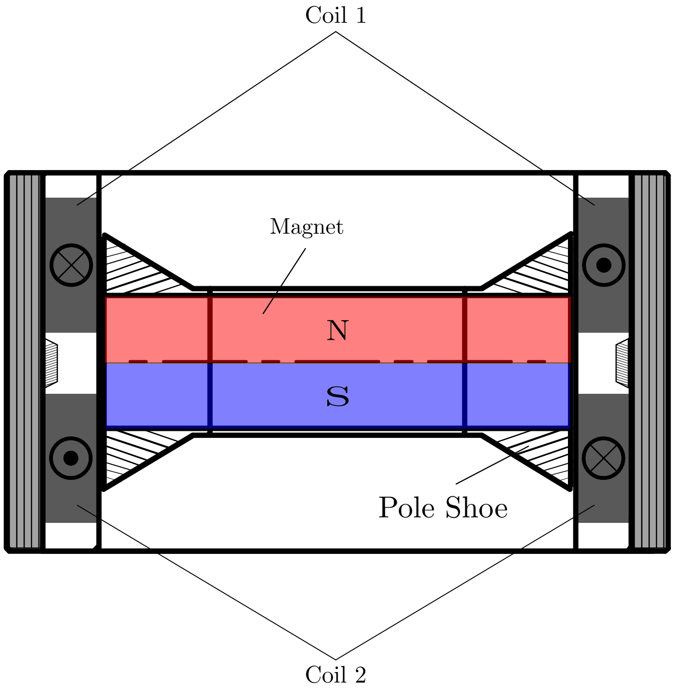

Figure 3.1: 2D drawing of the actuator.

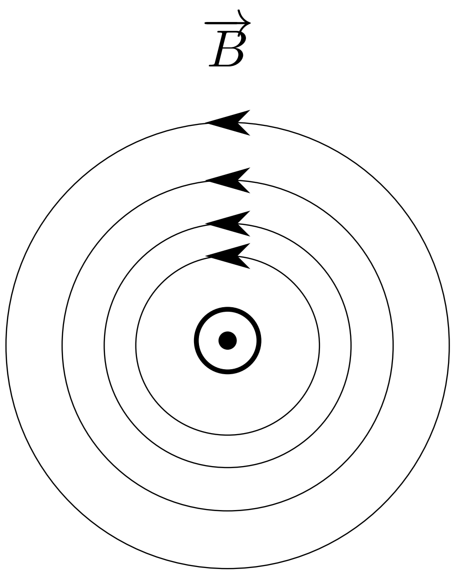

Figure 3.2: Magnetic field around a current carrying wire.

The magnetic field due to a small segment of the wire, $\overrightarrow{dL}$, is given by the Biot-Savart law

$$\overrightarrow{dB} = \frac{\mu_0 I \overrightarrow{dL} \times \overrightarrow{r}}{4\pi r^3}, \tag{3.3}$$

where r is the distance from the small segment $\overrightarrow{dL}$ to a point in space.

This can be used to calculate the magnetic field created by a current carrying loop, as shown in Figure 3.3.

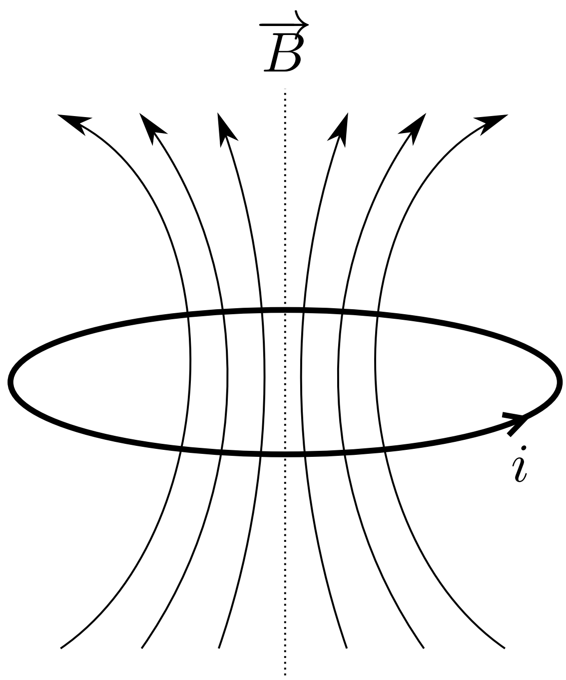

Figure 3.3: Magnetic field created by a current carrying loop.

The magnitude of the field at any point on the axis of the loop in the axial direction is

$$B = \frac{\mu_0 I R^2}{2(R^2 + z^2)^{\frac{3}{2}}}, \tag{3.4}$$

where R is the radius of the loop and z is the distance from a point on the axis to the center of the loop.

A coil is a set of circular loops in the radial and axial direction with each loop carrying the same current I and contributing to the magnetic field produced by the coil (Figure 3.4). Thus the magnetic field at any point on the axis of the coil is a summation of the fields induced by each loop at that point.

The strength of the magnetic field produced by the coil is given by

$$H_c = \frac{N \cdot I}{l_c}, \tag{3.5}$$

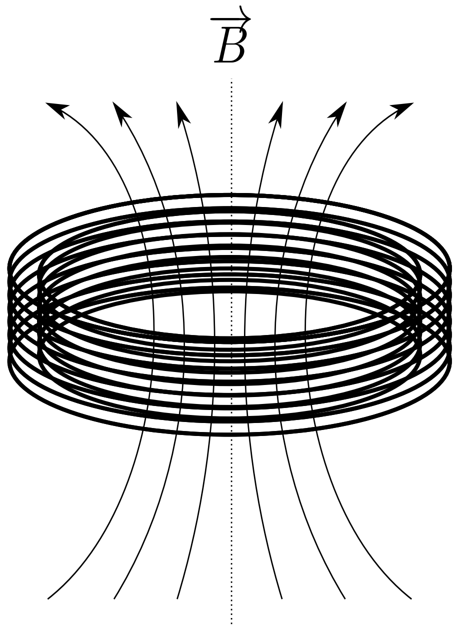

Figure 3.4: A coil composed of several loops in the axial and radial direction.

where N is the number of turns, I is the current through the coil, and l_c is the length of the coil.

A coil with N windings wound around a core of ferromagnetic material with relative permeability μ_r results in a magnetic flux density

$$B = \mu H_c = \mu_r \mu_0 \frac{N \cdot I}{l_c}. \tag{3.6}$$

3.1.2 Permanent Magnets

Permanent magnet are hard ferromagnetic materials with constant magnetization. To produce a permanent magnet a coil is wound around a core of a hard ferromagnetic material. The current in the coil and thus the intensity of the magnetic field is then increased until the core saturates. When the current is removed the core is still magnetized due to a remanent flux density, B_r. This process is illustrated in Figure 3.6.

The permanent magnet is then defined by its remanent flux density, B_r, coercivity, H_c, its geometry, and relative permeability, μ_m, of the ferromagnetic material which is usually close to that of vacuum (1.05). The permanent magnet usually operates in the second quadrant of Figure 3.6. The operating point depends on the reluctance of the magnetic circuit in which the magnet is placed as well as the intensity of the external magnetic field applied to the magnet. A permanent magnet is considered “shorted” when placed in a magnetic circuit with a core with high relative permeability (i.e. replacing the coil in Figure 3.5). The magnetic flux density in the circuit would be then close to

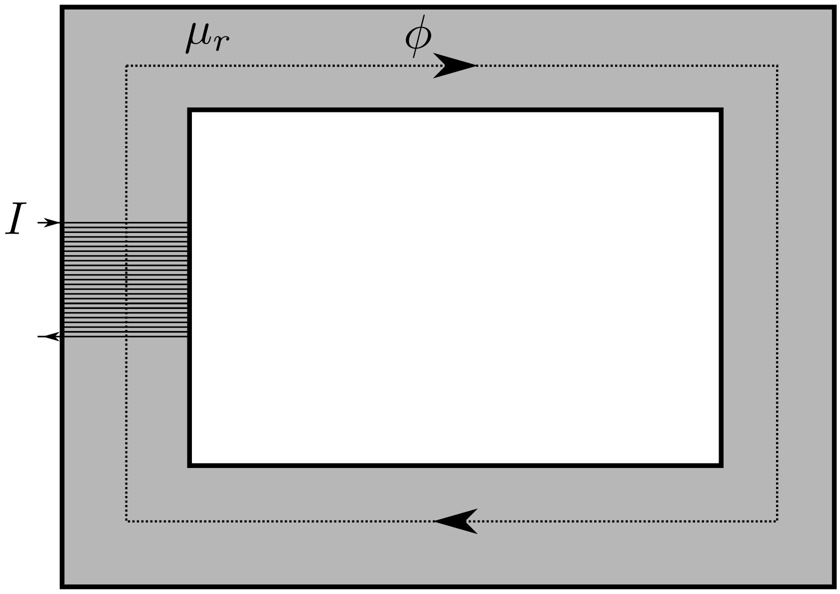

Figure 3.5: Coil in a magnetic circuit.

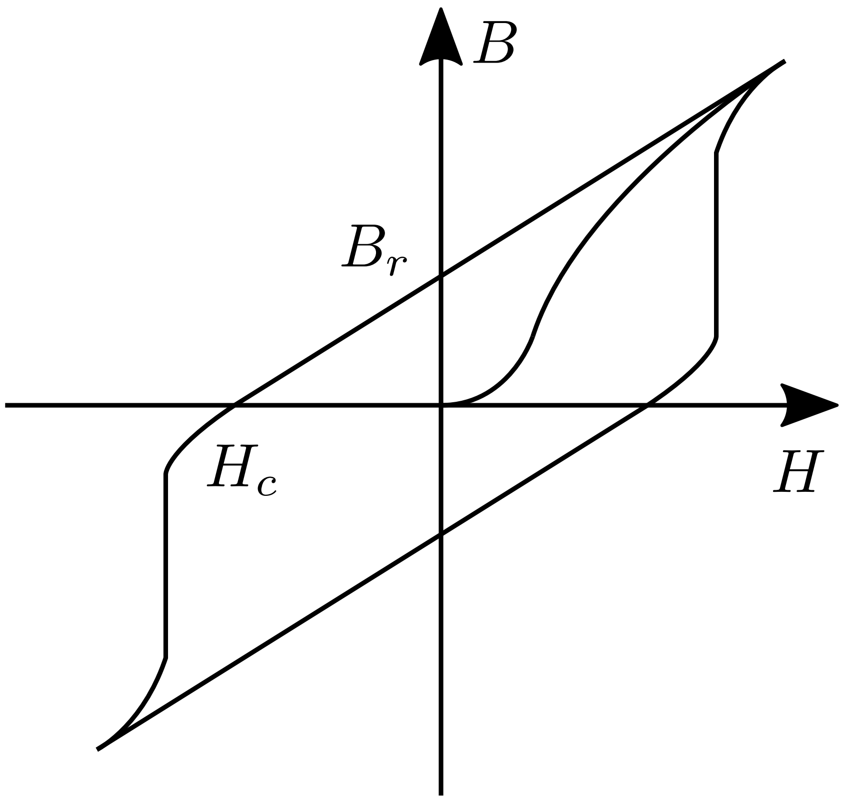

Figure 3.6: Hysteresis curve of a hard magnetic material.

B_r, while a permanent magnet placed in free space would have an operating point less than B_r.

The magnetic flux density of a magnetic circuit due to a permanent magnet in the circuit depends on the reluctance of the circuit. There are two equivalent methods to model a permanent magnet in a magnetic circuit equivalent to electric circuits [40]: the Norton model, a constant magnetomotive force, $\mathcal{F}_m$, in series with an internal reluctance, $\Re_m$ (voltage source in series with an electrical resistance), and the Thevenin model, a constant flux source, ϕ_r, in parallel with an internal reluctance, $\Re_m$ (current source in parallel with an electrical resistance). This is illustrated in Figure 3.7.

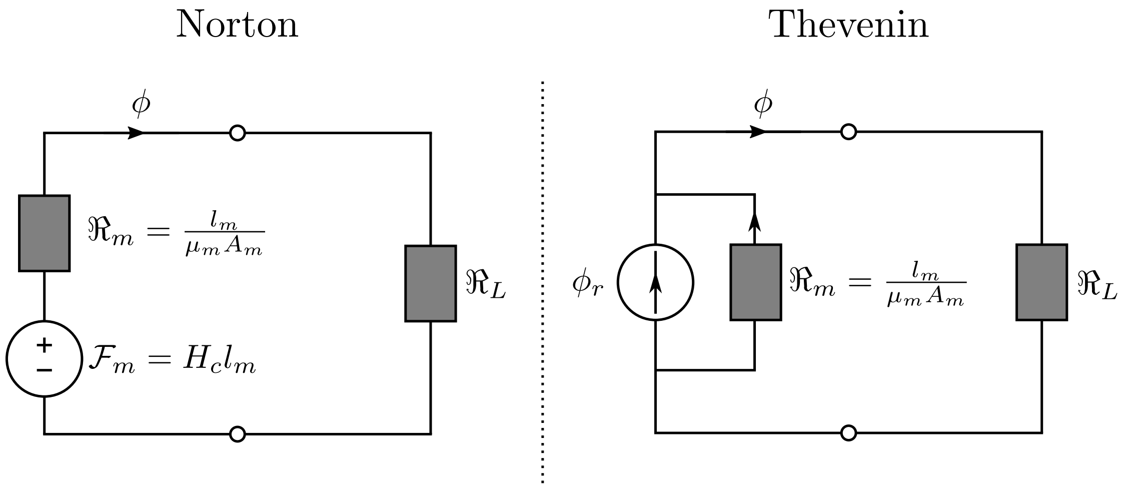

Figure 3.7: Modelling a permanent magnet in a magnetic circuit.

3.1.3 Coil Magnet Equivalence

Based on the previous subsection a permanent magnet can then be modelled as a coil or inversely, such that the magnetomotive forces are the same (Figure 3.8).

In this case a magnet can be modeled as a coil with a current $I = \frac{B_r l_m}{\mu_m N}$. On the other hand, a coil can be modeled as a permanent magnet with remnant flux density $B_r = \frac{\mu_0 N I}{l_c}$.

3.1.4 Forces

There are three forces acting on the mover: the main excitation force, F_E, a reluctance force, F_R, and a cogging force, F_C. In the following subsection, a brief review about the origins and characteristics of these forces will be provided.

3.1.4.1 Excitation Force

Any two permanent magnets, electromagnets, or a combination of both attract or repel each other based on the direction of their magnetic fields. An advantage of electromag-

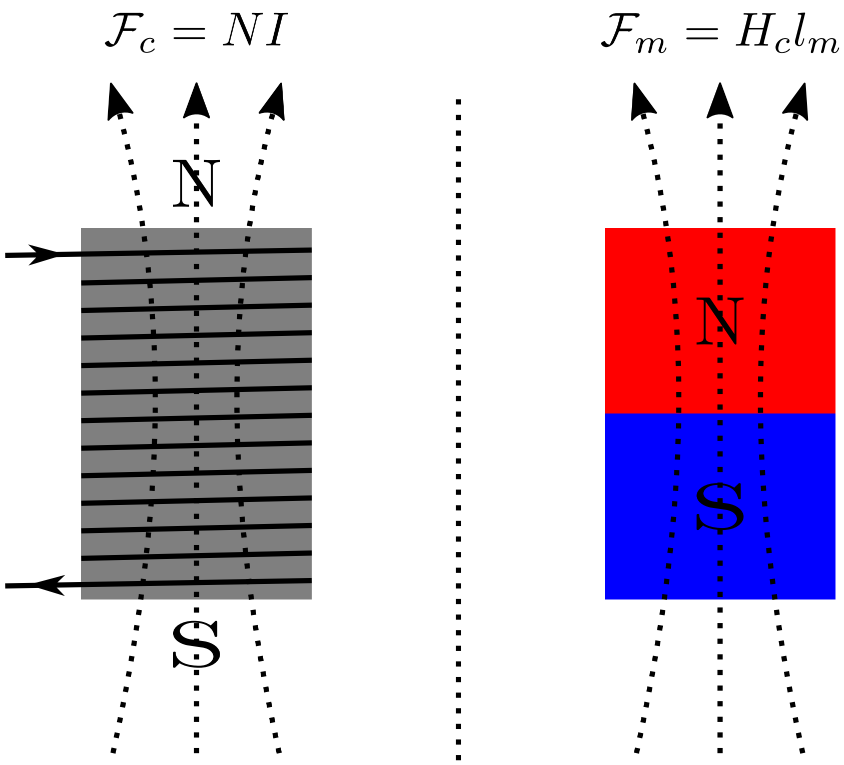

Figure 3.8: Equivalence between coils and magnets.

nets is that the magnetic field intensity depends on the current flowing through the coil, thus providing a control over the direction and intensity of the magnetic field.

According to the Lorentz force, a current carrying wire in a magnetic field will experience a force

$$\overrightarrow{F} = I\overrightarrow{L} \times \overrightarrow{B}. \tag{3.7}$$

Thus, a current carrying loop placed at an axial distance away from another current carrying loop (Figure 3.9) will experience an axial force given by [41] and [42]

$$F_f = \mu_0 I_1 I_2 z \sqrt{\frac{m}{4r_1 r_2}}[K(m) - \frac{m/2-1}{m-1}E(m)], \tag{3.8}$$

where

$$m = \frac{4r_1 r_2}{(r_1+r_2)^2 + z^2}, \tag{3.9}$$

where r_1 and r_2 are the radii of each loop, z is the distance between the loops, and K and E are the complete first and second elliptic integrals, given by

$$K(m) = \int_0^{\frac{\pi}{2}} \frac{d\theta}{\sqrt{1-m^2\sin^2\theta}}, \tag{3.10}$$

and

$$E(m) = \int_0^{\frac{\pi}{2}} \sqrt{1-m^2\sin^2\theta}\, d\theta. \tag{3.11}$$

Figure 3.10 shows the force acting on loop 2 when the loop is moved along the axis of loop 1 when an equal current of 1 A is flowing through each loop (for a given geometry).

Through this formulation, a magnet can be represented with a number of loops only in the axial direction (i.e. a coil with only surface current density), also called a thin coil, while a normal coil is represented with multiple loops in the axial and radial direction (a thick coil) [42].

A magnet can also be represented as a single layer, or a shell, with a surface current density. The equation to calculate the axial force between two cylindrical permanent magnets using this representation was first derived by [43] and later simplified by [44] as

$$F_s = \frac{B_{r1}B_{r2}}{2\mu_0}\sum_{i=1}^{2}\sum_{j=3}^{4}(-1)^{i+j}m_1 m_2 m_3 f_s, \tag{3.12}$$

where B_{r1} and B_{r2} are the remanent flux densities of the two magnets. The function f_z is defined in terms of the complete elliptic integrals of first, second, and third kind (K(m), E(m), and $\prod(n|m)$) as

$$f_s = K(m_4) - \frac{1}{m_2}E(m_4) + (\frac{m_1^2}{m_3^2} - 1)\prod(\frac{m_4}{1-m_2}|m_4), \tag{3.13}$$

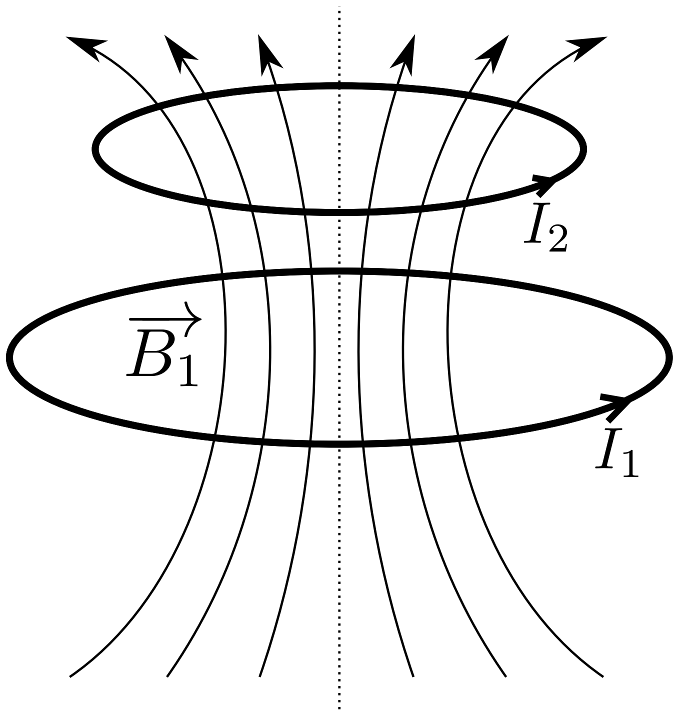

Figure 3.9: Two current carrying loops.

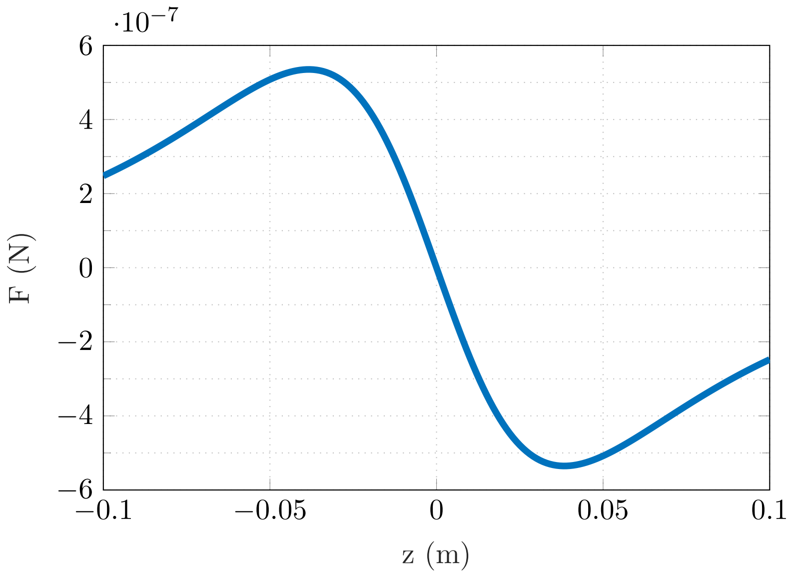

Figure 3.10: Force on current carrying loop due to a magnetic field from another loop.

and

$$
\begin{aligned}
m_1 &= z_i - z_j, && (3.14)\\
m_2 &= \frac{(r_1 - r_2)^2}{m_1^2} + 1, && (3.15)\\
m_3^2 &= (r_1 + r_2)^2 + m_1^2, && (3.16)\\
m_4 &= \frac{4r_1 r_2}{m_3^2}. && (3.17)
\end{aligned}
$$

The geometries of the two magnets are given by the radii r_1 and r_2, and the top and bottom coordinates of the first magnet z_1 and z_2 and the second magnet z_3 and z_4 respectively.

There are four main methods to in literature to calculate the axial force between coaxial magnets and coils [44], two of which will be presented here based on the formulations above: the *filament* method and the *shell* method.

The filament method The *filament* method assumes that a coil is composed of a number of circular loops in both in the radial and axial direction while a permanent magnet is composed of circular loops only in the axial direction. The force is then calculated using the superposition principle, simply by adding the contribution of each filament, using (3.8). The magnet is then approximated as a thin coil with circular loops only in the axial direction with current per turn $I = \frac{B_r l_m}{N_m \mu_0}$, where B_r and l_m are the strength and length of the magnet respectively, and N_m the chosen number of turns.

The axial force between a coaxial coil and magnet modelled with the filament method can then be calculated through [44]

$$
F_F = \sum_{n_m=1}^{N_m} \sum_{n_r=1}^{N_r} \sum_{n_z=1}^{N_z} F_f(r(n_r), R_m, z + L(n_m, n_z)), \tag{3.18}
$$

where

$$
\begin{aligned}
r(n_r) &= r_c + \frac{n_r - 1}{N_r - 1}(R_c - r_c), && (3.19)\\
L(n_m, n_z) &= -\frac{1}{2}(L_m + L_c) + \frac{n_z - 1}{N_z - 1}L_c + \frac{n_m - 1}{N_m - 1}L_m, && (3.20)
\end{aligned}
$$

where R_m is the radius of the magnet, r_c is the inner radius of the coil and R_c the outer radius, L_m is the length of the magnet and L_c that of the coil, z is the axial distance between the center of the magnet and the center of the coil, N_r is the number of turns of the coil in the radial direction and N_z in the axial direction, and N_m is the number of turns of the magnet (only in the axial direction). Based on (3.8), I_1 is the current in the coil and I_2 is the “equivalent” current of the permanent magnet (thin coil) and is given by

$$I_2 = \frac{B_r Lm}{N_m \mu_0}, \tag{3.21}$$

where B_r is the remnant flux density of the magnet.

The shell method The *shell* method assumes that a permanent magnet is composed of only one shell or layer with a certain surface current density and a coil is composed of different shells or layers on the radial direction. Similar to the *filament* method the force can be calculated using the superposition principle, by adding the contribution of each layer based on (3.12). Using this method, the coil is approximated as a magnet with multiple layers in the radial direction, with a magnet strength $B_r = \frac{\mu_0 NI}{l_c}$, where N is the number of turns of one layer of the coil, I is the current in the coil, and l_c is the length of the coil.

Thus the axial force between a coil and a magnet modeled using the *shell* method is calculated through [44]

$$F_S = \frac{1}{N_r} \sum_{n_r=1}^{N_r} F_s(R_m, r(n_r), L_m, L_c, z) \tag{3.22}$$

where

$$r(n_r) = r_c + \frac{n_r - 1}{N_r - 1}(R_c - r_c) \tag{3.23}$$

and F_z is the force calculated using (3.13). In this case, B_{r1} is the remnant flux density of the permanent magnet and B_{r2} is the "equivalent" remnant flux density of the modeled coil (with current I, number of windings in the axial direction N_z, and length L_c) and is given by

$$B_{r2} = \frac{\mu_0 N_z I}{L_c}. \tag{3.24}$$

Figure 3.11 illustrates the difference between the two methods for the actuator under study.

To summarize, the *filament* method starts from the force exerted by one circular loop on another and uses the superposition principle to calculate the the force between two coils (each coil has loops in the radial and axial directions), whereas the *shell* method is based on the force between two magnets. Which method to use for an actuator which is composed of a coil and magnet depends on which approximation: approximating a magnet as a thin coil, i.e. loops only in the axial direction (*filament* method), or approximating a coil as a magnet with multiple layers in the radial direction (*shell* method).

Figure 3.12 shows the axial force acting on a magnet when the magnet is axially moved between two coils which have equal but opposite currents (arrangement shown in Figure 3.11. The force is calculated using the above two methods. The stroke z is the position of the center of the magnet, with the $z = 0$ the center of the first coil and $z = 30$, that of

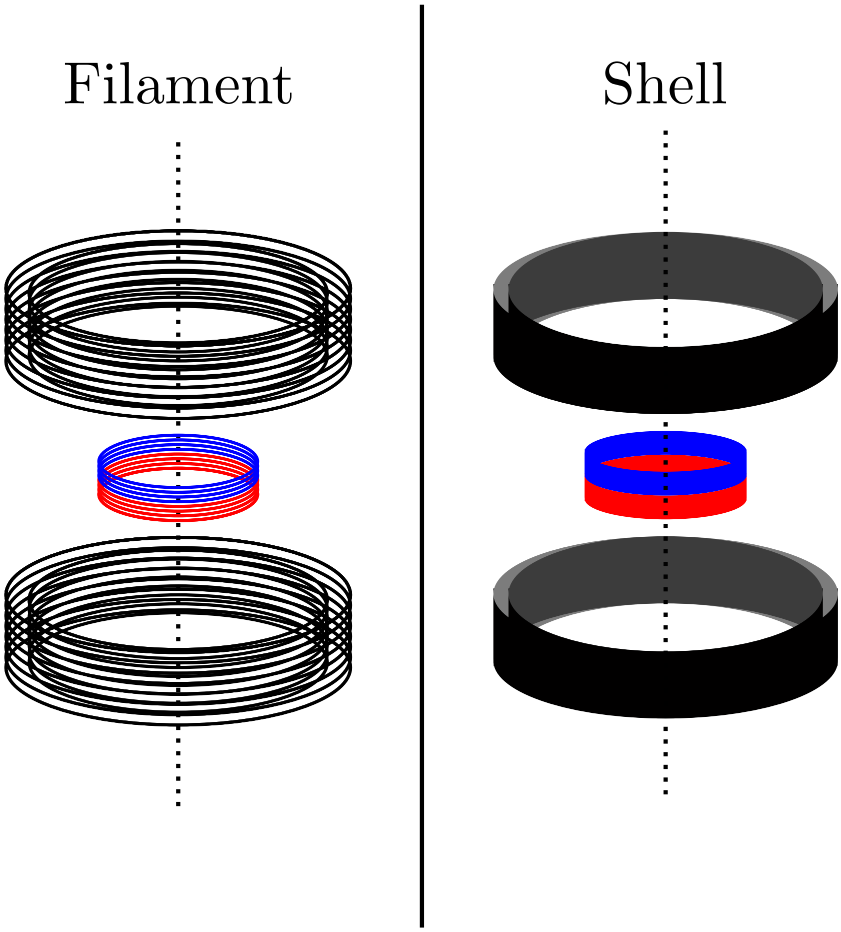

Figure 3.11: Coil and magnet representation using the filament or the shell method.

the second coil. The results show that the two methods differ at the middle of the stroke (when the force is maximum) with the *shell* method being closer to the real model [44]. The parameters used to generate Figure 3.12 are listed in Table 3.1.

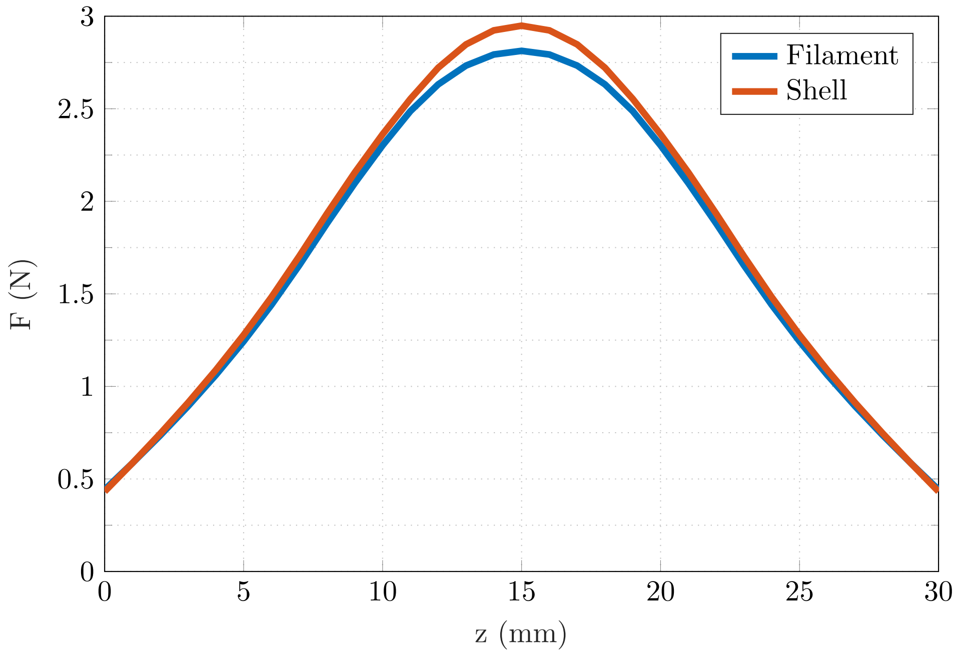

Figure 3.12: Force on magnet moving between two coils.

3.1.4.2 Reluctance Force

As shown in Figure 3.1, the mover is composed of a disc shaped permanent magnet sandwiched between two pieces of ferromagnetic material of high relative permeability. Thus the reluctance path (and the total reluctance) of the magnetic field generated by one coil due to a current in the coil changes based on the position of the mover. This leads to a reluctance force exerted by the coil on the mover which acts to minimize the reluctance and attracts the mover to the coil.

Simple Magnetic Circuit A simple magnetic circuit is shown in Figure 3.13 which is similar to Figure 3.5 with an added air gap.

The reluctance path of the magnetic flux induced by the coil is then composed of the reluctances of the ferromagentic material and the two air gaps and is given by

$$\Re = \frac{l}{\mu_0 \mu_r A}, \tag{3.25}$$

where l is the length of the reluctance element being calculated, A is the cross sectional area, and μ_r is the relative permeability of the material. The reluctance of the air gap is then

Table 3.1: Coil and magnet parameters for Figure 3.12.

Parameter	Value
R_c	25 mm
r_c	21 mm
L_c	26 mm
N_z	25
N_r	4
R_m	20 mm
L_m	11 mm
N_m	11
Current, $\lvert I \rvert$	1 A
B_{rm}	1.11 T

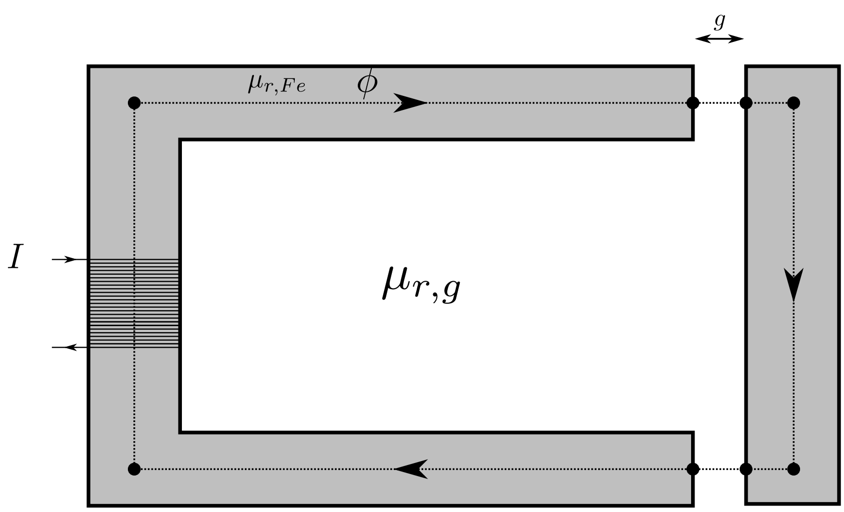

Figure 3.13: Simple magnetic circuit to illustrate the reluctance force.

$$\Re_g = \frac{g}{\mu_0 \mu_{r,g} A}, \tag{3.26}$$

and depends on the length of the air gap g while the reluctance elements of the ferromagnetic material is constant and equal to

$$\Re_c = \frac{l_{Fe}}{\mu_0 \mu_{r,Fe} \cdot A}, \tag{3.27}$$

$\mu_{r,Fe}$ is the relative permeability of the ferromagnetic material. The relative permeability of the air gap is equal to 1.

The total reluctance is the summation of all reluctances of the different elements (the paths can be separated based on the nodes shown in Figure 3.13. Magnetic circuits can be analogous to electric circuits as shown in Table 3.2.

Table 3.2: Analogy magnetic and electric circuits.

Electrical quantity	Magnetic quantity
Voltage, U	MMF, Θ
Current, I	Flux, Φ
Resistance, R	Reluctance, $\Re$
Ohm's Law, $U = R \cdot I$	$\Theta = \Re \cdot \Phi$
Conductivity, σ	Permeability, μ

The MMF is $\Theta = N \cdot I$, and the flux is then

$$\phi = \frac{\Theta}{\Re_{\sum}} = \frac{N \cdot I}{\Re_g + \Re_c}. \tag{3.28}$$

The inductance is given by

$$L = \frac{N \cdot \phi}{I}, \tag{3.29}$$

and the stored magnetic energy is

$$W_m = \frac{1}{2} \cdot L \cdot I^2. \tag{3.30}$$

Thus when the coil is excited with a current I a force is exerted on the moving part towards the main core (in this case left) in order to minimize the air gap. This force can be calculated from the change in magnetic energy

$$F = \frac{dW}{dx} = \frac{1}{2} \cdot I^2 \cdot \frac{dL}{dg}. \tag{3.31}$$

Unlike the excitation forces, reluctance forces are then attractive only. An actuator based only on the reluctance force (solenoids) requires a spring to bring the mover back to the original position.

3.1.4.3 Cogging Force

The cogging force is also a reluctance force which acts on the moving magnet, but due only to the magnetic field of the permanent magnet (not the excitation of the coil). Hence, the magnitude of the force depends only on the position of the mover and will try keep the magnet in the central position of the actuator.

Similar to the reluctance force due to the excitation of a coil, the magnetic field of a permanent magnet will try to take the path with minimum reluctance leading to a force acting on the moving part. Similarly, this force can be calculated from the change in magnetic energy using (3.31).

3.2 Hybrid Model

The modelling approach taken here is a hybrid model that combines analytical together with FEM modelling. First, the analytical equations of the coils in the actuator are presented. After that, an FEM model of the actuator is created from which the parameters of the model are calculated based on the current in the coils and position of the mover. Then finally, using curve fitting methods, these parameters are defined as a function of current and position and used in a full simulation model.

3.2.1 Analytical Model

As previously presented, the stator of the actuator under study is made up of two coils connected in antiseries form, so that the same current is flowing in both coils but in opposite direction. The mover is a disc shaped permanent magnet hollow in the middle, sandwiched between two pole shoes of ferromagentic material. In this configuration, the coils exert a force twice as much as when only one coil is available.

Due to symmetry it is possible then to study each coil on its own, and apply symmetry to analyze the second coil.

Starting with Kirchhoff's voltage law, the voltage drop on one coil is the resistive voltage drop in addition to the induced voltage in the coil due to a changing magnetic field. This can be represented with equation (3.32),

$$u(t) = R \cdot i(t) + \frac{d\Lambda(t)}{dt}, \tag{3.32}$$

where

- u is the voltage drop across the coil
- R is the resistance of the coil
- i is the current through coil
- Λ is the flux linkage in coil
- t is the time variable

Let 1 denote the first coil and 2 denote the second coil. The Flux Linkage in one coil depends on current i and position x is composed of three components:

$$\Lambda_1(i,x) = \Lambda_{11}(i,x) + \Lambda_{21}(i,x) + \Lambda_{pm,1}(x), \tag{3.33}$$

where

- Λ_{11} is the flux linkage in coil 1 due to the current through coil 1
- Λ_{21} is the flux linkage in coil 1 due to the current through coil 2
- $\Lambda_{pm,1}$ is the flux linkage in coil 1 due to the permanent magnet (PM) in the mover
- x is the position of the mover

The derivative of each component with time is then

$$\frac{d\Lambda(i,x)}{dt} = \frac{\partial\Lambda(x,i)}{\partial i}\cdot\frac{di}{dt} + \frac{\partial\Lambda(x,i)}{\partial x}\cdot\frac{dx}{dt}. \tag{3.34}$$

The derivative of the flux linkage becomes

$$\begin{aligned}\frac{d\Lambda_1}{dt} &= \left(\frac{\partial\Lambda_{11}(x,i)}{\partial i} + \frac{\partial\Lambda_{21}(x,i)}{\partial i}\right)\cdot\frac{di}{dt}\\ &+ \left(\frac{\partial\Lambda_{11}(x,i)}{\partial x} + \frac{\partial\Lambda_{21}(x,i)}{\partial x} + \frac{d\Lambda_{pm,1}(x)}{dx}\right)\cdot\frac{dx}{dt}\end{aligned} \tag{3.35}$$

Assume work in the linear region, linear dependence of flux linkage on current, the self and mutual inductance are then

$$\begin{aligned}\frac{\partial\Lambda_{11}(x,i)}{\partial i} &= L_{11}(x)\\ \frac{\partial\Lambda_{21}(x,i)}{\partial i} &= L_{21}(x)\end{aligned} \tag{3.36}$$

3.2.2 FEM Model

In this section, the FEM model of a permanent magnet linear oscillating actuator will be presented.

The FEM model was built based on the Finite Element Method Magnetics software package written by Dr. David Meeker [45]. It is an open source software for solving 2D and axisymmetric magnetic, electrostatic, heat flow, and current flow problems with graphical pre- and post-processors.

Figure 3.14 shows an axi-symmetric 2D Model of the actuator drawn using the graphical pre-processor of the FEM software.

Figure 3.15 shows the result of an FEM simulation using the post-processor of the software package. The coils are excited with a DC current of 1 A. Using the post-processor the total force acting on the mover as well as the flux linkage in the coils

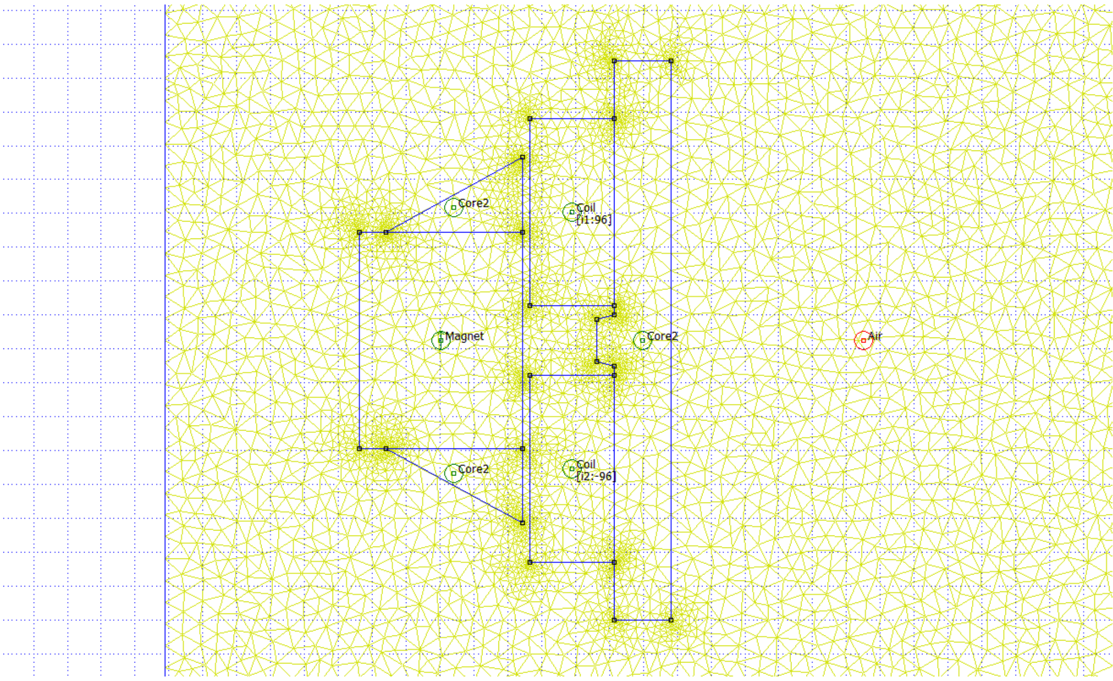

Figure 3.14: Axi-symmetric 2D Model of the E core actuator.

can be calculated. By repeating the simulation for different positions of the mover and calculating the force and flux linkage with and without any current excitation, the forces and total inductance can be derived as will be shown in the next section.

Starting with the flux linkage, the current in one coil is fixed to 1 A and sweeping of the position is performed. The flux linkages against position are shown in Figure 3.16

Since the coils are in series, the total inductance can be calculated using (3.36) and summing the self and mutual inductances. The result is shown in Figure 3.17.

At each instant in time, there are three types of axial electromagnetic forces acting on the mover, in addition to the frictional and load forces:

- $F_{e,1}(i,x)$ and $F_{e,2}(i,x)$, the excitation force due to current in coil 1 and coil 2 respectively
- $F_{\Re,1}(i,x)$ and $F_{\Re,2}(i,x)$, reluctance force due to current in coil and coil 2 respectively
- $F_c(x)$, the cogging force due to the permanent magnet
- F_K and F_S, static and kinetic friction
- F_L, load force

The first type is the main moving force referred here as the excitation force, or the force due to the interaction between the magnetic field from the permanent magnet and

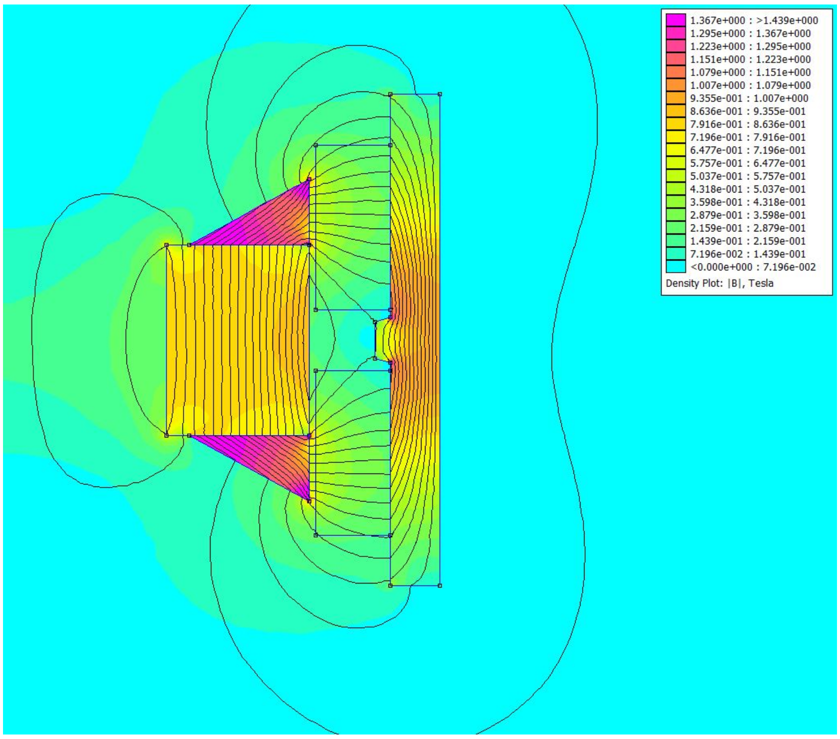

Figure 3.15: Results of an FEM simulation of the E core actuator showing flux density.

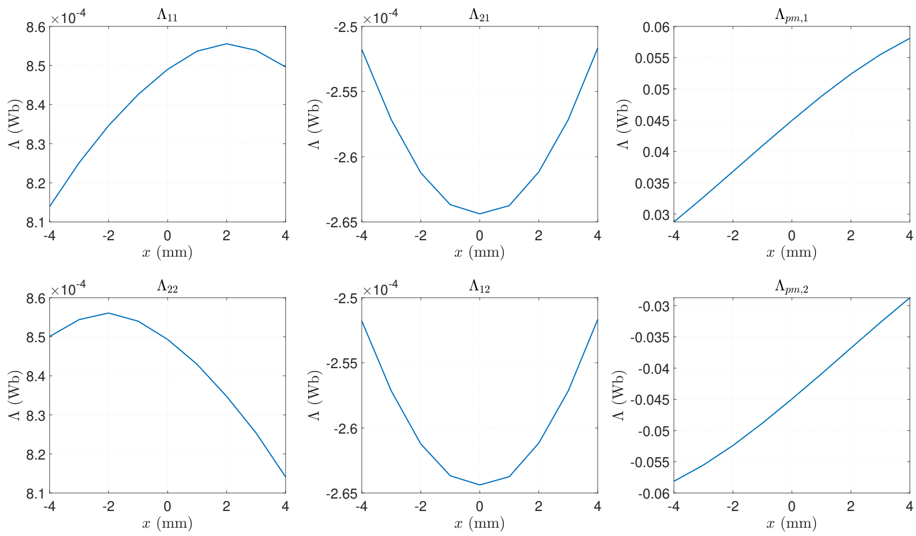

Figure 3.16: Self, mutual flux linkage, and flux linkage due to the permanent magnet in each coil when 1 A current is flowing.

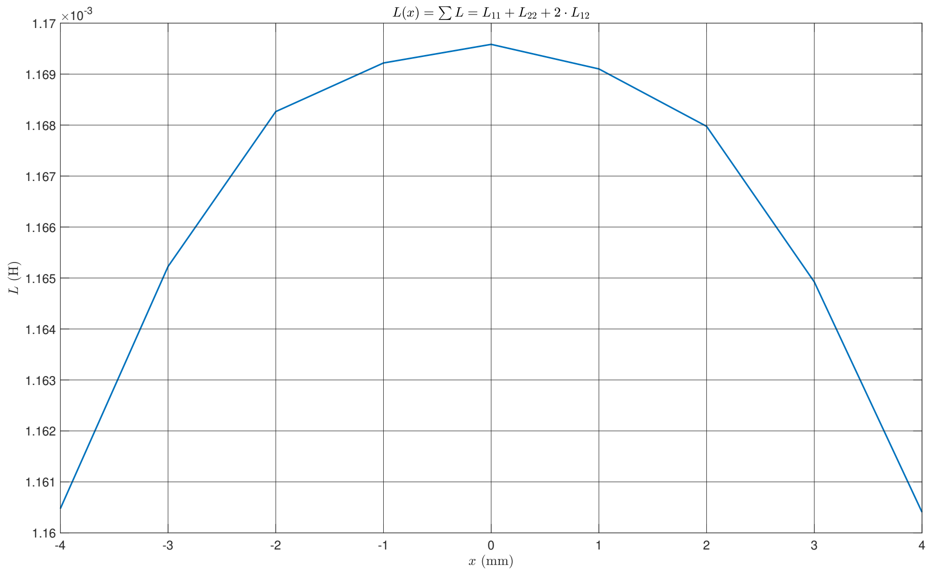

Figure 3.17: Total inductance of the actuator.

the magnetic produced by current flowing through the coil. The direction of this force is axial with a direction which depends on the sign of the current, and a magnitude which depends on the magnitude of the current flowing through and the coil and the position of the mover with respect to the coil.

The second type of forces is the reluctance force, which is the force acting on the mover due to only current flowing through the coil. As mentioned before, the mover has two pole shoes of ferromagentic material. This results in an always attractive force (force attracting the mover to the coil) with a magnitude which depends on the current flowing through the coil and the position of the mover with respect to the coil.

The third type is the cogging force, which is the force acting on the mover due to only the permanent magnet in the mover. This kind of force can also be interpreted as a reluctance force which always forces the mover in to the center of the stator, and has a magnitude which depends on the strength of the magnetic field from the permanent magnetic and the position of the mover.

For simulation purposes, the reluctance force can be calculated alone from the total force given by the FEM tool by disabling the permanent magnet in the mover and exciting each coil independently. Figure 3.18 shows a surf plot of the total reluctance force as a function of current and position. It can be seen here that the force has a quadratic dependence on current and a linear dependence on position.

Similarly the cogging force be calculated by moving the mover along the stroke, without exciting the coils. Figure 3.19 shows the cogging force acting on the mover as a function of position. It shows a cubic dependence of the force on position.

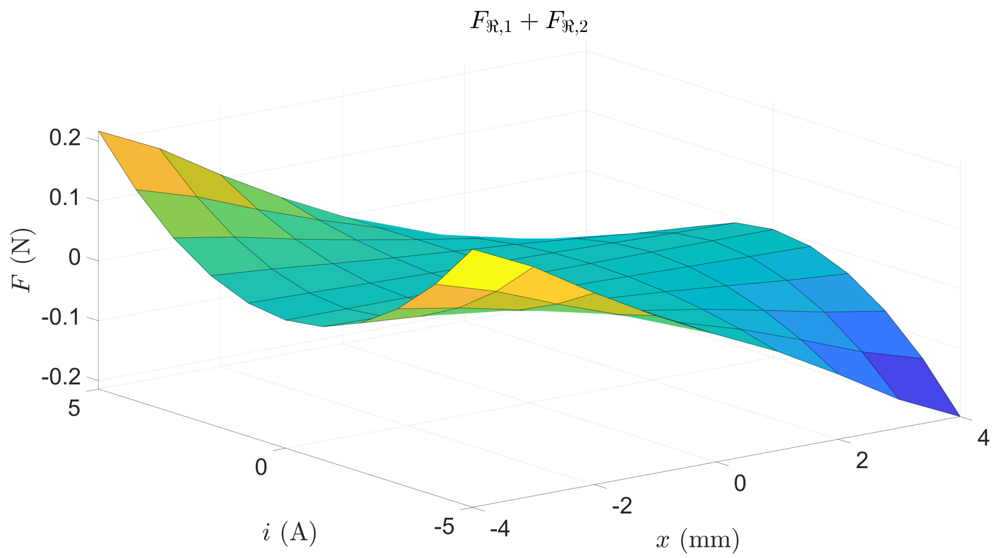

Figure 3.18: Total reluctance force acting on the actuator as a function of current and position.

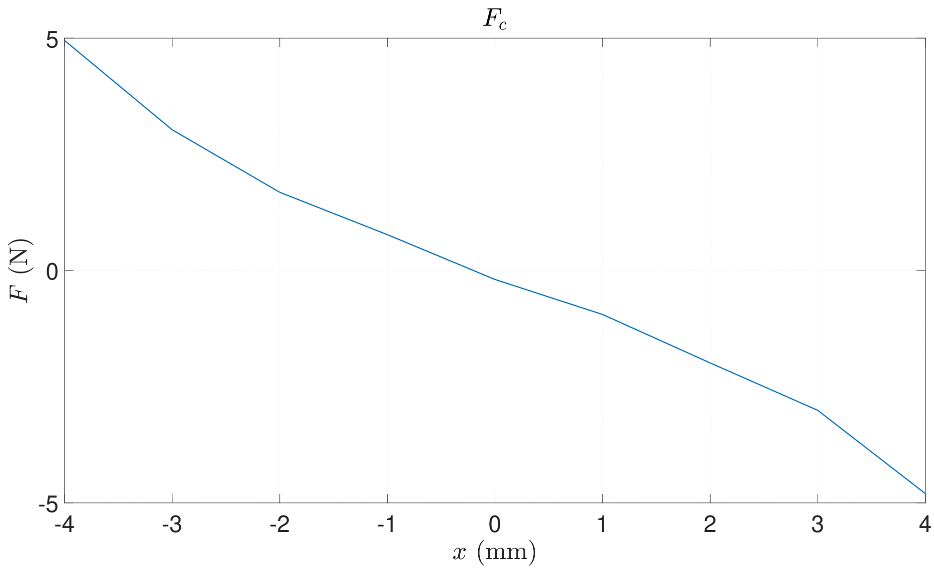

Figure 3.19: Cogging force acting on the actuator as a function of position.

Finally, the excitation force is then calculated as the total force minus the reluctance and cogging forces. Figure 3.20 shows the excitation forces due to each coil and their sum as a function of position when 1 A and −1 A current is flowing through the coils. Figure 3.21 shows the total excitation force acting in the mover as a function of current position. It can be seen that the force has a direct dependency on the current and a quadratic dependency on the position.

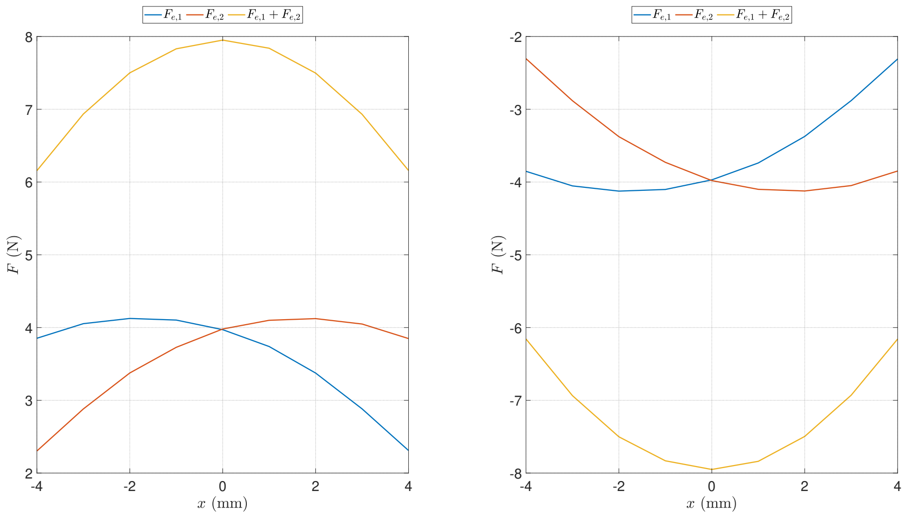

Figure 3.20: Excitation force due to each coil and their sum acting on the mover when 1 A (left) and −1 A (right) current is flowing through the coils.

In summary, the forces can be represented as following with dependency on current and position:

The excitation force can be represented as

$$F_e(i,x) = i(t) \cdot f_e(x) \tag{3.37}$$

where $f_e(x)$ is the force and the back e.m.f. constant, and is of the form $a \cdot x^2(t) + b \cdot x(t) + c$.

The reluctance force can be represented as

$$F_{\Re}(i,x) = x(t) \cdot f_{\Re}(i) \tag{3.38}$$

where $f_{\Re}(i)$ is of the form $a \cdot i^2(t) + b \cdot i(t) + c$.

The cogging force can be represented as

$$F_c(x) = a \cdot x^3(t) + b \cdot x^2(t) + c \cdot x + d \tag{3.39}$$

Then the full model can be derived as

$$\begin{cases} u(t) = R \cdot i(t) + L(x) \cdot \frac{di(t)}{dt} + f_e(x) \cdot v(t) \\ m \cdot \frac{dv(t)}{dt} = i(t) \cdot f_e(x) + x(t) \cdot f_{\Re}(i) + F_c(x) + F_l(t) \\ \frac{dx(t)}{dt} = v(t) \end{cases}$$

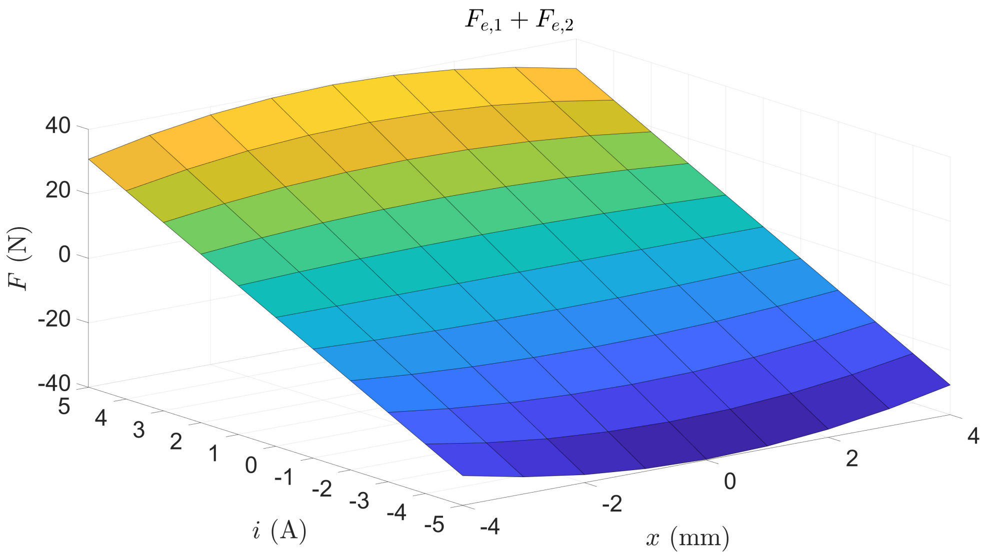

Figure 3.21: Total excitation force acting on the actuator as a function of current and position.

where

- $R = R_1 + R_2$ is the sum of the resistances,
- m is the mass of the mover,
- v is the speed of the mover,
- F_l comprises the disturbance and load forces.

Let the magnetic force F_m be the sum of the excitation, reluctance, and cogging forces acting on the mover, the actuator can be divided into three subsystems as shown in Figure 3.22 where the electrical subsystem is shown in Figure 3.23. Figure 3.24 shows a signal flow diagram of the actuator from the input voltage u to the output position x.

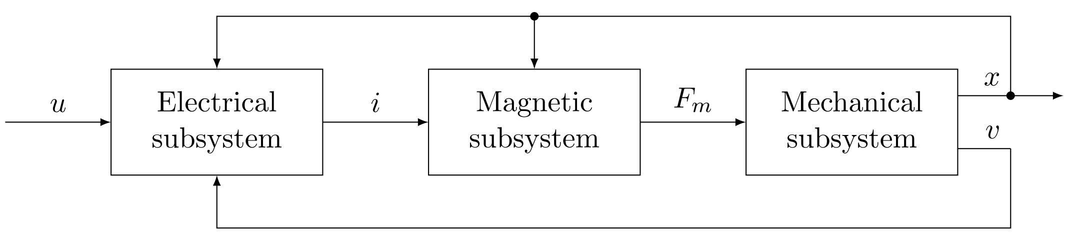

Figure 3.22: High level model of the actuator with the three subsystems, electrical, magnetic, and mechanical.

Let the current, speed, and position be the states of a state space model, then the actuator can be modelled in state space as

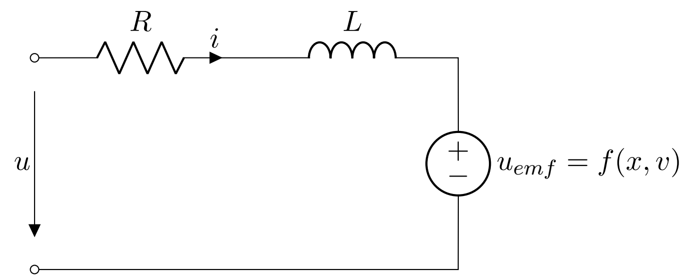

Figure 3.23: Electrical subsystem.

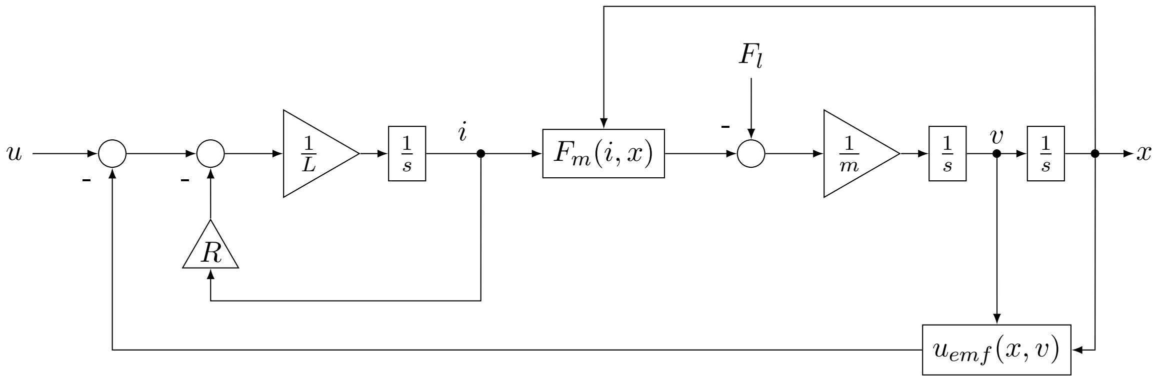

Figure 3.24: Signal flow diagram of the actuator.

$$\begin{cases} \frac{di(t)}{dt} = -\frac{R}{L(x)} \cdot i(t) - \frac{f_e(x)}{L(x)} \cdot v(t) + \frac{u(t)}{L(x)} \\ \frac{dv(t)}{dt} = \frac{1}{m} \cdot (i(t) \cdot f_e(x) + x(t) \cdot f_{\Re}(i) + F_c(x) - F_l(t)) \\ \frac{dx(t)}{dt} = v(t) \end{cases} \tag{3.40}$$

3.3 Excitation

In order to control the speed and position of the mover, the current in the coils of the actuator which translates directly to a magnetic force would need to be controlled to a desired value throughout the stroke range. In this section, the single phase voltage source inverter is introduced and the PWM strategy to control the inverter and eventually the current in the actuator.

3.3.1 Single Phase Voltage Source Inverter

The standard in the electric drives field is PWM control of a voltage source inverter, the voltage across an electrical machine is varied by switching of semiconductor switches. Figure 3.25 shows the diagram of a single phase voltage source inverter.

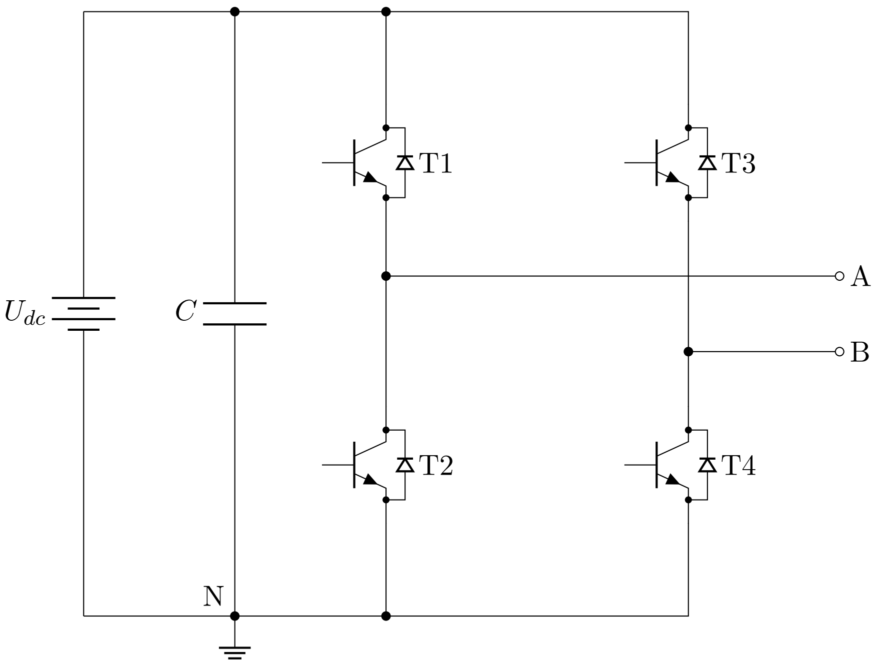

Figure 3.25: Single phase voltage source inverter.

The four switches, $T1$ to $T4$ are the semiconductor switches which can be switched on and off by applying a voltage at the gate or removing it. The actuator is connected to the terminals A and B. The diodes across the switches are the body diodes. These provide a path to the current when a switch is open and there is still energy in the inductor of the actuator which needs to be dissipated.

3.3.2 PWM

The input voltage $u(t)$ derived in the model in (3.40) can be applied through the voltage source inverter. Such an inverter applies one of three voltages at the terminals of the actuator: U_{dc}, 0, or $-U_{dc}$. If the controller is calculating the reference voltage at a fixed sampling rate (as is usually the case with standard controllers), then the calculated reference voltage cannot change sign within one sampling period. This leads to the fact that during one sampling instant only U_{dc}, 0 or $-U_{dc}$, 0 can be applied, to be called active and zero states, where in an active state either a positive or negative DC link voltage is applied and during a zero state, the terminals of the actuator are short circuited. The duration of each state is then calculated based on the comparison of the reference voltage calculated by the controller compared to a triangular signal. The average voltage applied at the terminals of the actuator is equal to the reference voltage.

There are two PWM types for single phase inverter, unipolar and bipolar modulation [46]. To prevent short circuit, in both PWM control types the switches of each leg, i.e. $T1$ and $T2$, are controlled in a complimentary manner, so that they are never on at the same time.

In bipolar modulation, $T1$ and $T3$ are also controlled in a complimentary manner which means one reference signal is needed (input voltage $u(t)$) to be compared to a carrier signal. The result is that the voltage applied across the actuator terminals is either U_{dc} or $-U_{dc}$ [46].

On the other hand, in unipolar modulation $T1$ and $T3$ are controlled independently where the reference signal $u(t)$ is used to control the Leg A and its negative, $-u(t)$, is used to control Leg B. This leads to the result that the voltage applied across the actuator terminals is U_{dc}, $-U_{dc}$, or 0 [46].

As expected, the downside of the bipolar switching is the increased ripple in the current leading to higher harmonics. In [46], a comparison of the two methods was done in simulation, where it was found that the Total Harmonic Distortion is lower when using the unipolar method. Thus unipolar PWM will was chosen for this project.

Figure 3.26 illustrates the unipolar PWM method for a positive reference voltage. In the figure, the resulting states of each switch can be seen as well as the resulting voltage across the terminals of the actuator.

Since the resulting waveform of the output voltage is a square wave, it can be easily analyzed using Fourier series. Assume the reference voltage u is normalized to the DC-Link voltage (i.e. it has a value between 1 and -1, corresponding to U_{dc} and $-U_{DC}$ respectively), then the output voltage can be expressed as

$$u_{AB}(\theta) = u \cdot U_{dc} + \sum_{n=2,4,6,\ldots}^{\infty} ((-1)^{\frac{n}{2}} \frac{4U_{dc}}{n\pi} \sin(\frac{nu}{2}\pi) \cos(n\theta)). \tag{3.41}$$

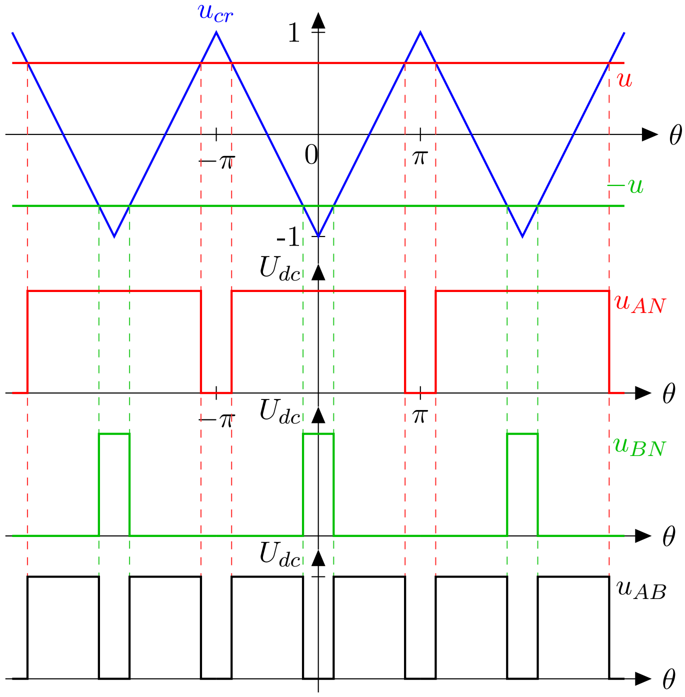

Figure 3.26: Switching legs of a single phase PWM inverter and the resulting voltage.

3.3.3 Deadtime

To prevent a short circuit, the two switches of Leg A or Leg B cannot both be closed at the same time. Moreover, the closing and opening time of a switch is not instantaneous, rather depends on the characteristics of the transistor, applied voltage, load current, etc...thus, one switch cannot be closed until the other switch is full open. This is ensured by delaying the closing of one switch after the intersection of the reference and carrier signals. In [47], the effect of deadtime on the load current is analyzed when a sinusoidal reference voltage is used. The authors also present methods to compensate for the deadtime effects.

Figure 3.27 shows the effect of the deadtime on the output voltage assuming the current in the actuator circuit is positive as in Figure 3.23 (current is flowing outside of leg A and into leg B) and the resulting voltage applied to the actuator. The difference to the case without deadtime can be seen in the dashed lines of u_{AN}, u_{BN}, and u_{AB}. The width of the pulse of the output voltage is reduced by the length of the deadtime which leads to a reduction in the average voltage applied to the actuator. Similarly Figure 3.28 shows the case when the current is negative. The result here is that the width of the pulse of the output voltage increases resulting in an increased average voltage applied to the actuator (compared to the reference voltage).

Depending then on the sign of the current, the reference voltage can be increased or decreased to compensate for the disturbance of the deadtime:

$$\begin{cases} u_{comp} & = u + \Delta u \\ \Delta u & = \text{sign}(i) \cdot \frac{T_{deadtime}}{T_{PWM}} \cdot U_{dc}, \end{cases} \tag{3.42}$$

where u_{comp} is the compensated reference voltage, $T_{deadtime}$ is the deadtime, and T_{PWM} is the length of one PWM period.

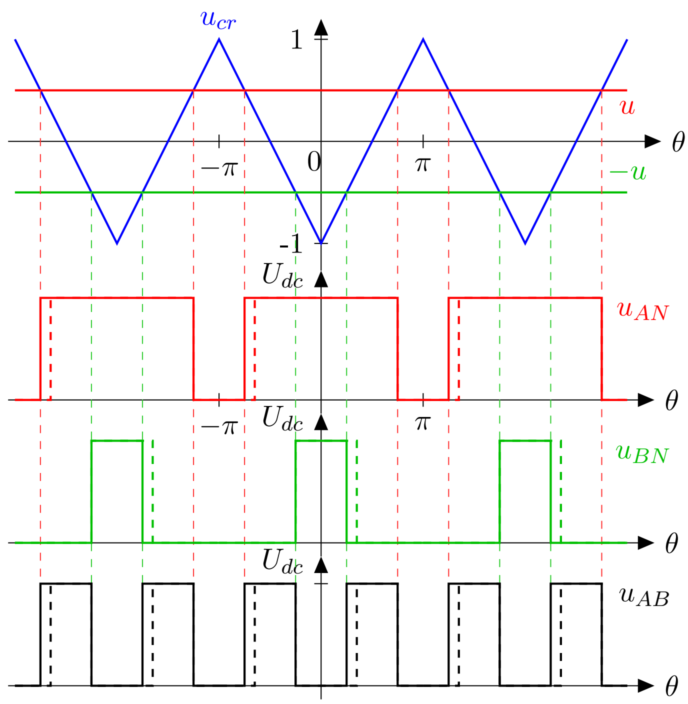

Figure 3.27: Switching legs of a single phase PWM inverter and the resulting voltage with deadtime assuming positive current.

3.3.4 Exponential Response

Based on the electrical model in (3.40), the actuator can be modelled as an R-L circuit in series with a speed dependent voltage source, as shown in Figure 3.23 where the back e.m.f voltage is a function of speed and position ($u_{emf} = f(x, v)$).

As shown in the previous section, the voltage applied to the terminals of the actuator is U_{dc}, $-U_{dc}$, or 0. In the continuous time domain, the model is transferred to the Laplace domain. The current is then calculated as

$$I = \frac{U - f_e(x) \cdot V}{s \cdot L(x) + R} \tag{3.43}$$

For simplicity, taking $u(t) = \pm U_{dc} - f_e(x) \cdot v$ as the input to the R-L series circuit during the active cycle and $u(t) = -f_e(x) \cdot v$ during the zero cycle, the current response is the solution of the first order differential equation:

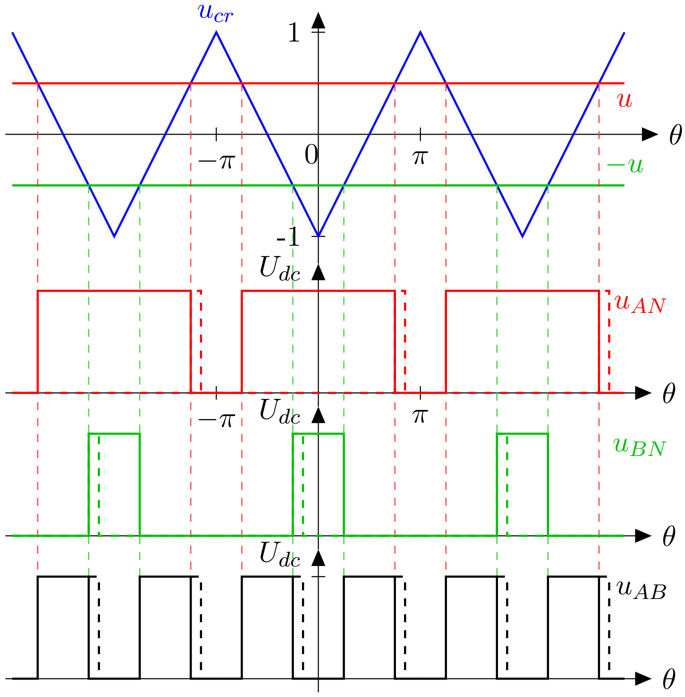

Figure 3.28: Switching legs of a single phase PWM inverter and the resulting voltage with deadtime assuming negative current.

Converting to a discrete form

$$i(k+1) = i(k) \cdot e^{-\frac{R}{L} \cdot T_s} + \frac{u(k)}{R} \cdot (1 - e^{-\frac{R}{L} \cdot T_s}), \tag{3.44}$$

where T_s is the duration of one cycle. This equation describes the current response to an active or zero state.

3.4 Disturbances and Load

In this section, the disturbances which act on the mover as well as the application dependent load will be introduced.

3.4.1 Friction

Next to the load force, the friction force is perhaps the largest disturbance force acting on the mover. Friction force is complicated to model mainly studied in Tribology. However, there are models in the control engineering literature agreed upon to model this phenomena as best as possible. Perhaps the most used model in literature is the one which divides friction into three types: Coulomb, viscous, and the Stribeck [48, 49].

The Coulomb model models the constant part of the friction force, i.e. the part which does not change with speed. This is given by [48]

$$F_{Cl} = \mu_{Cl} \cdot F_n \cdot \mathrm{sign}(v), \tag{3.45}$$

where F_n is the normal force, μ_{Cl} is the friction coefficient, and v is the speed of the mover.

The normal force F_n depends on the mass of the mover, gravitational acceleration, and the angle between the plane of the axis of the mover and a flat surface. The friction constant μ_{Cl} depends on the materials of the mover and the guiding rails, temperature, humidity, etc...the $\mathrm{sign}(v)$ is there since the friction force always opposes the movement.

The second friction force present is the viscous friction and perhaps the most simplest, given by

$$F_v = \mu_v \cdot v, \tag{3.46}$$

where μ_v is the viscous friction constant. At relatively high speeds, this is the most dominant friction force in motion control applications.

The third friction model is the Stribeck model and perhaps the most complicated. It models the friction force at and in the vicinity of zero speed. Figure 3.29 shows qualitatively the resulting total force of friction as a function of speed. At zero speed, there is already a force preventing the movement of the mover. Once the moving force exceeds the stopping force, the friction force acting against the movement drops till the speed reaches what is called the “breakaway speed” after which the friction force is the Coulomb and viscous friction. The viscous friction increases linearly with the speed.

The Coulomb and viscous friction could be identified and compensated for by using a feedforward controller [48], however, the Stribeck friction is too complicated and is

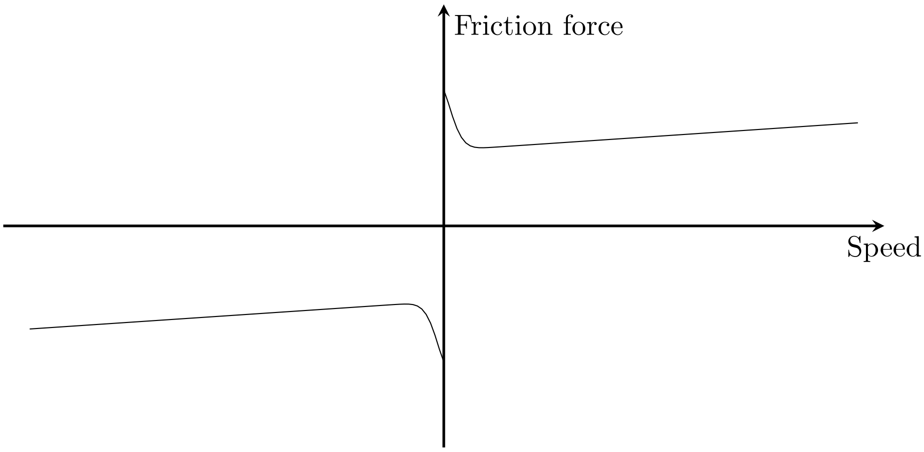

Figure 3.29: Qualitative illustration of the friction force as a function of speed.

usually depending on multiple factors. It can be compensated for using feedback control. Identifying the friction model is not part of this work. It is nevertheless, important to show the effects of friction especially since the actuator operates in an oscillating motion, meaning that the speed will always oscillate between zero and maximum. Figure 3.29 shows the strong discontinuity of the friction force at and in the neighborhood of zero speed.

3.4.2 Eddy Current Damping Force

Another disturbance force which opposes the movement of the magnet is the magnetic force due to induced eddy currents. The moving magnet actuator is basically a magnet moving in a steel cylinder. According to Faraday's and Lenz's law, the changing magnetic field due to the magnet movement induces an e.m.f. which opposes the change in the magnetic field. Stainless steel has a Conductivity typically in the range of $1 \times 10^6\,\mathrm{S/m}$ to $2 \times 10^6\,\mathrm{S/m}$. This implies that a current (eddy currents) will be induced in the stator leading to a magnetic field opposing the change of the magnetic field of the moving magnet and eventually slowing down the magnet. The concept is illustrated in Figure 3.30.

In [50], a study was performed to calculate the force induced by eddy currents on a magnet moving in a conductive tube made of copper. The authors reach the conclusion that in steady state, the force can be simplified in a linear relation with speed in steady state such that

$$F_{ed} = c_{ed} \cdot v, \tag{3.47}$$

where c_{ed} is the damping coefficient and depends on the multiple factors such as material and dimension, and the force is always opposing direction of motion (tries to slow down the mover). Note that the study was done on a copper cylinder and copper usually has a conductivity around thirty times that of stainless steel. In a real world scenario, the

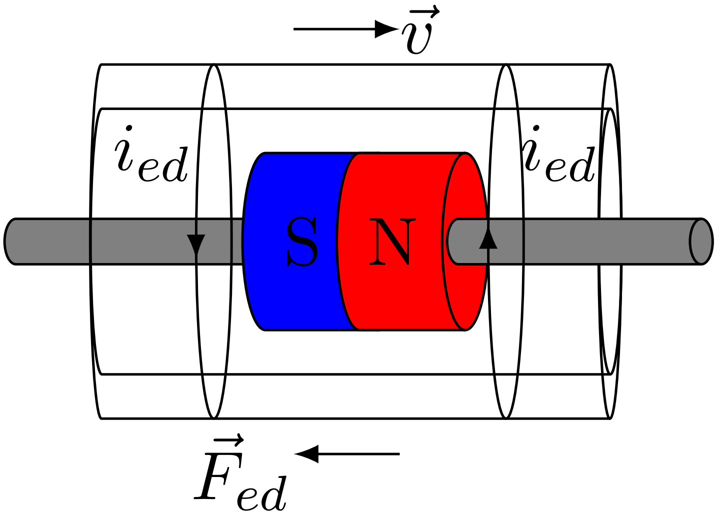

Figure 3.30: Damping force due to induced eddy currents.

force speed relation would be much more complex. Factors such as magnetic saturation and actuator end effects have a big influence on this relation.

3.4.3 Load Forces

As mentioned in the introduction, linear actuators are used in many different applications in the industry. Thus, the load forces acting on the actuator are application dependent and can range from almost no load force (except the mass of the moving object) to constant gravitational force to complex load forces which have dependency on conditions such as temperature, humidity, etc.... in this section, the some of the load forces from common applications will be introduced.

In [5], a linear magnetic actuator was designed for vibration testing. In this case and depending on how the device to be tested is mounted, the only load force could be the gravitational force

$$F_g = m \cdot g \cdot \cos\theta, \tag{3.48}$$

where m is the total mass of the mover (including the device under test), $g \approx 9.81\text{m/s}^2$, and $\theta \neq \frac{\pi}{2}$rad is the angle which the axis of the mover makes with the horizontal surface. Assuming a positive speed is when the mover travels in the positive $y - axis$ direction and assuming the only load force in (3.40) is the gravitational force $F_l = F_g$, the load force as a function of speed is shown in 3.31.

Another application for linear actuators is linear compressors for refrigeration [51]. Traditional compressors use a rotating motor with a crankshaft to convert rotational motion to translational. A piston oscillating inside a cylinder compresses the gas. By replacing the rotating motor with a linear actuator the crank mechanism can be removed

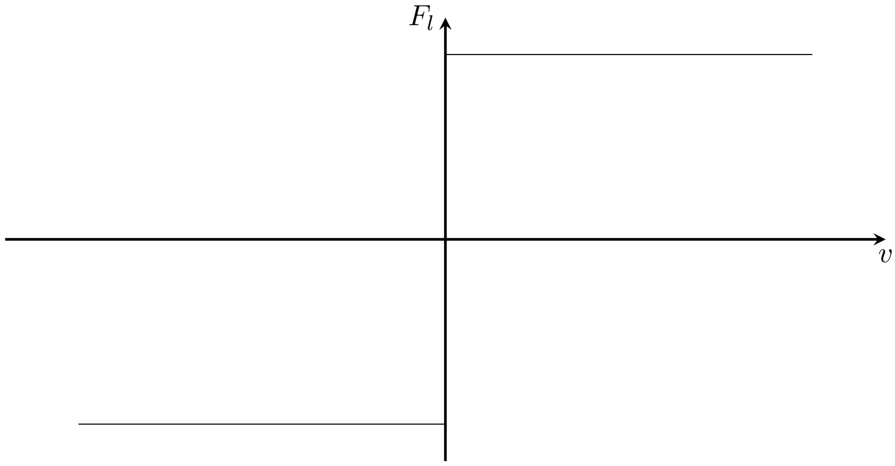

Figure 3.31: Gravitational load force as function of speed.

increasing efficiency and reducing the total cost of the system [51]. It is not the aim of this thesis to go into detail into the operation of compressors, however, it is worth noting the type of load force acting on the actuator in compressor applications.

The ideal gas law is given as

$$P \cdot V = n \cdot R \cdot T, \tag{3.49}$$

where P is pressure, V is volume, n is the number of moles of the gas, R is the ideal gas constant, and T is the temperature. Pressure is related to force by

$$P = \frac{F}{A}, \tag{3.50}$$

where F is the force acting on a surface area A.

If a piston is compressing gas in a cylinder as illustrated in Figure 3.32, the volume of the space in which the gas is compressed gets smaller, leading to increase in pressure (assuming the temperature stays constant). Keeping the surface area constant, the force is then inversely related to the volume.

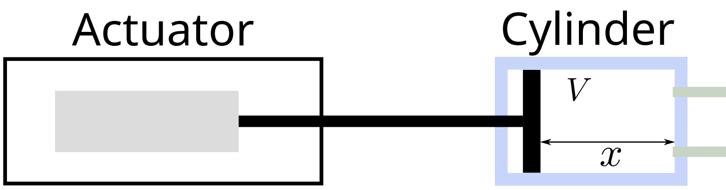

Figure 3.32: Actuator driving a piston in a cylinder.

The volume of the chamber can be calculated as

$$V = A \cdot x, \tag{3.51}$$

where x is the distance between the piston and the cylinder. The force as a function of displacement is then given by

$$F = \frac{n \cdot R \cdot T}{x}, \tag{3.52}$$

and plotted in Figure 3.33.

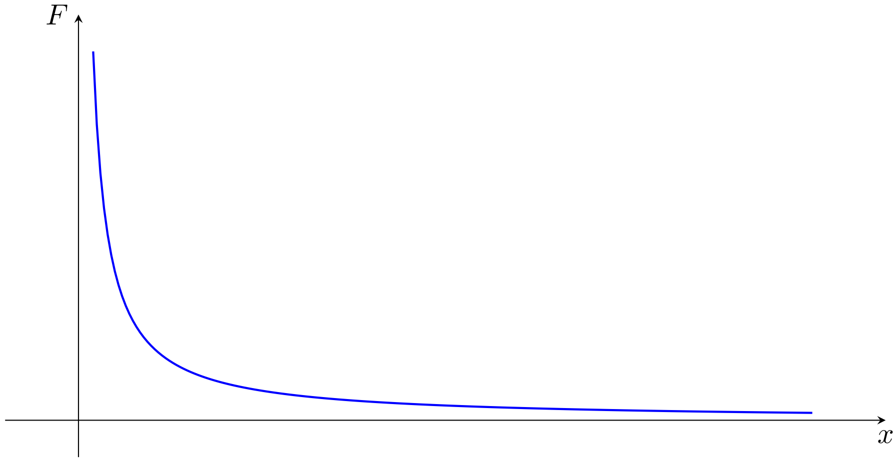

Figure 3.33: Load force acting on a piston compressing gas as a function of displacement.

The simplified model of the load force acting on the actuator in compressor applications shows the nonlinear dependency of the force on the position of the mover. If this model can be identified, then it can be compensated in the controller by using feed-forward control for example, however, in the real world this model depends on many external environmental factors which can change during operation.

4 Test Bench

In this chapter, in the first section, a brief overview of the test bench components will be presented. Then in the second section, the procedure and results of the measurements of the position dependent parameters such as the inductance and force constant are shown.

4.1 Physical Setup

The physical setup is composed of the actuator itself, the voltage source inverter, and the control system.

4.1.1 Actuator

The moving magnet actuator selected for this study is the MMA 6033 [39]. Figure 4.1 shows the stator and the moving magnet with the pole shoes, while Table 4.1 shows the electrical and mechanical ratings of the actuator.

Figure 4.1: Stator (left) and the moving magnet (right).

A plunger is manufactured and fixed to the mover and the whole setup is then housed in a steel structure. The plunger sits and moves on two plastic bearings, one on each side. A position sensor is fixed to the plunger. Figure 4.2 shows the mechanical setup

Table 4.1: Electrical and mechanical ratings of the actuator.

Rated Voltage	48 V
Rated Current	5 A
Maximum Current	30 A
Stroke	8 mm
Force, continuous	38.4 N
Force, peak	259 N
Moving mass (total)	0.2 kg

with all the different parts. The force sensor selected for force measurements is an S type load sensor with rating upto 10 kg.

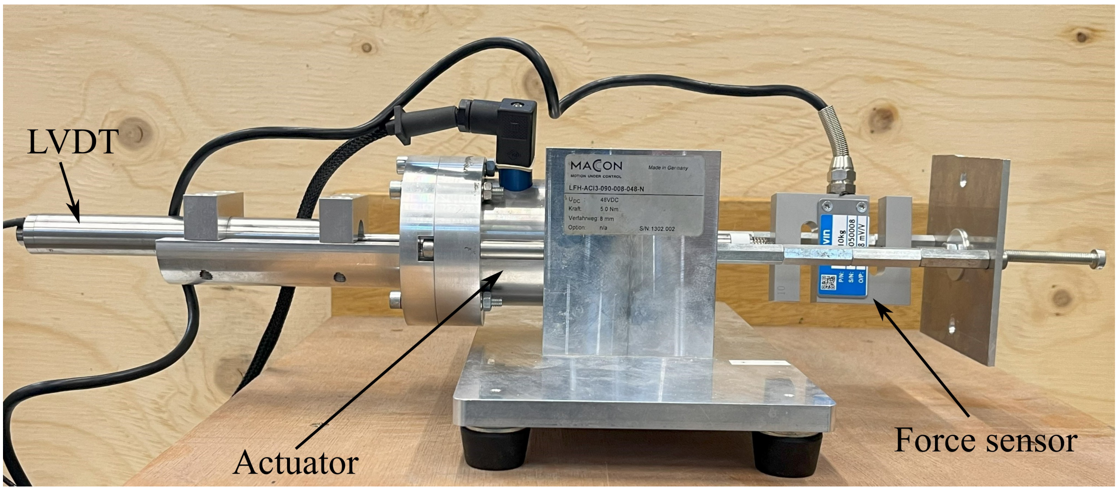

Figure 4.2: Mechanical setup of the actuator.

4.1.2 Inverter

The PWM inverter is an H Bridge IGBT inverter with access to the IGBT switches gates through fiber optical receivers. This allows the control system to control each of the 4 switches independently by sending digital I/O control signals through fiber optic cables.

Figure 4.3 shows a top view of the test bench where the actuator and the PWM inverter can be seen.

4.1.3 Control System

The control system is a real time control system based mainly on a powerful processor and an FPGA. Signal processing can be done either fully on the processor or on the FPGA or both combined. For this project, the main controller is running on the processor while the PWM logic and current measurement at PWM switching instances is running on the

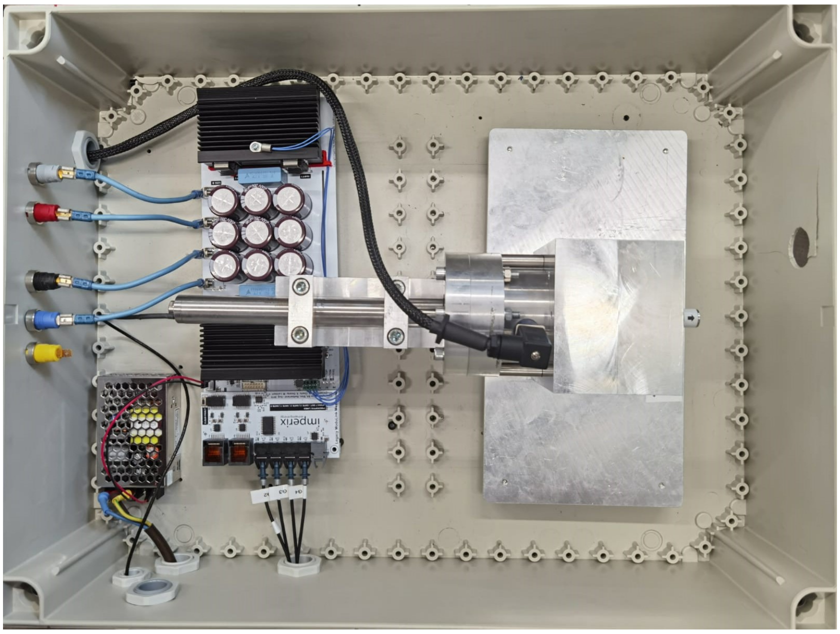

Figure 4.3: Test bench showing from a top view the actuator and the PWM inverter.

FPGA. The processor and the FPGA read the current and position signals, after which the processor is calculating the reference voltage which is sent to the FPGA. Based on the PWM logic as illustrated in Figure 3.26, the digital I/O control signals are sent to the PWM inverter. This is illustrated in Figure 4.4.

Figure 4.5 shows the signal flow between the processor and the FPGA on the control system. The main control and estimator are implemented on the processor where the duty cycles for phases A and B are calculated as well as the timings needed by the counter on the FPGA to measure all four switching currents. These currents are then read by the processor at the next sample time.

4.1.4 Position Sensor

The position sensor used is a LVDT. An LVDT is a type of electromechanical transducer that converts the linear displacement of a movable core into an electrical signal. It is widely used for precise measurement of linear position and displacement. The high accuracy, robustness, and contactless operation make it suitable for a wide range of applications in various industries.

It consists of the following main components:

- Primary Winding: A coil of wire placed in the center of the device, which is energized by an alternating current (AC) source.
- Secondary Windings: Two identical coils placed symmetrically on either side of the primary winding. These are connected in series opposition (differentially).

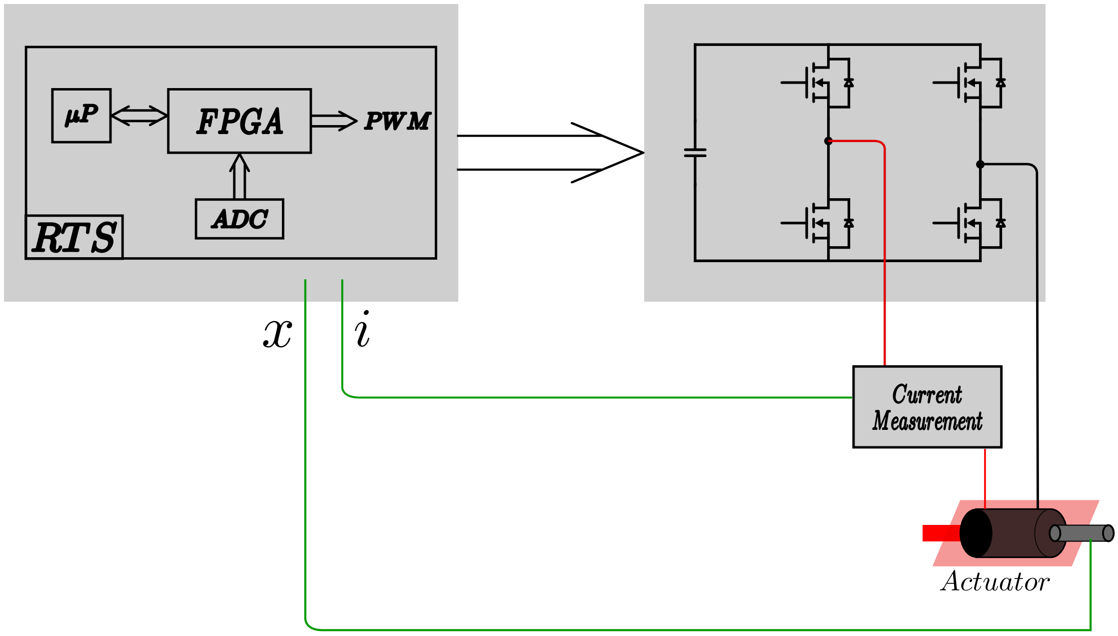

Figure 4.4: Illustration of the control system.

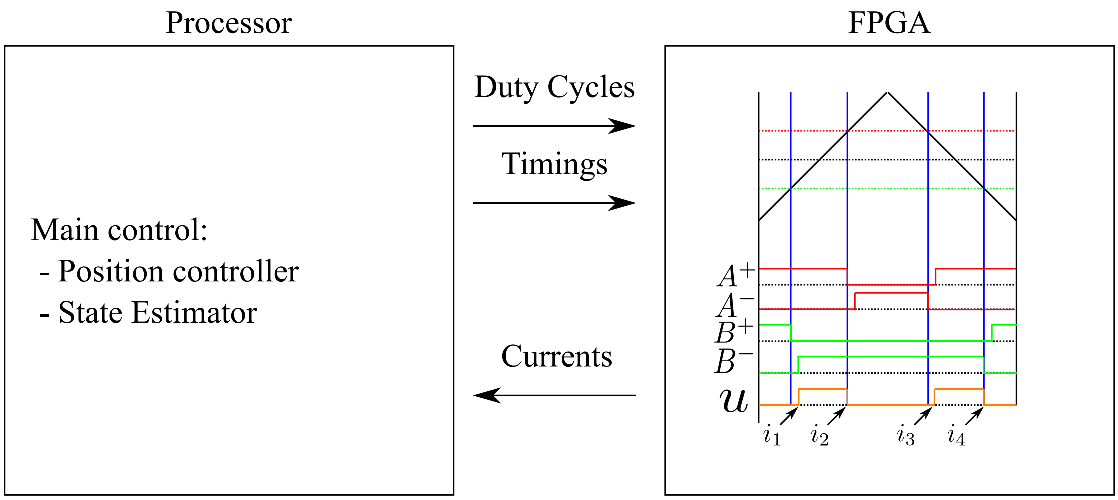

Figure 4.5: Signal flow between processor and FPGA.

- Movable Core: A ferromagnetic rod that moves linearly within the windings. The position of this core determines the output signal.

Figure 4.6 shows a simple schematic of an LVDT with the three main components.

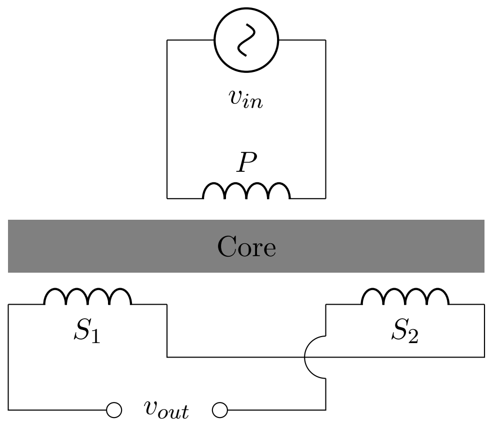

Figure 4.6: Simple schematic of an LVDT.

The operation of an LVDT is based on electromagnetic induction. An AC voltage is applied to the primary winding, creating an alternating magnetic field. This magnetic field induces an electromotive force (EMF) in the secondary windings. The position of the movable core affects the coupling between the primary and secondary windings: when the core is at the center, the induced EMFs in the secondary windings are equal and opposite, resulting in a net output of zero, while when the core moves away from the center, the coupling changes, causing a difference in the induced EMFs which is proportional to the displacement of the core. The differential voltage between the secondary windings is the output signal.

To obtain a usable output, the raw signal from the LVDT needs to be processed through:

- Demodulation: Converting the AC signal to a DC signal.
- Filtering: Removing noise and unwanted frequencies.
- Amplification: Increasing the signal strength for further processing or display.

Other types of linear position sensors include potentiometers, laser interferometers, optical encoders, and magnetostrictive sensors [52]. Compared to other linear sensors, LVDTs provide highly linear output over a wide range of motion. They are durable and can operate in harsh environments. The core does not make physical contact with the windings, reducing wear and tear. Capable of detecting very small displacements. They are used in various applications such as aerospace, industrial automation, medical devices, and robotics.

4.2 Measurements

As show in the previous chapter, the force constant and inductance are position dependent, thus here they will be measured for different positions of the mover. In each measurement, the mover is fixed at a certain position, and excited directly (without the inverter). Voltage, current, and the force on the mover are measured.

4.2.1 Static Inductance Measurements

In order to see the change of inductance with position, here the actuator is excited with a sinusoidal voltage signal. Then by moving the mover incrementally, voltage across the actuator and current through are measured.

By applying a high frequency sinusoidal input voltage

$$u_{hf}(t) = U \cdot \sin(\omega_c t), \tag{4.1}$$

where U is the amplitude of the applied signal and ω_c is the frequency of the applied signal referred here as the carrier frequency. Inserting (4.1) into the first part (electrical) (3.40) and solving for the current (assuming zero speed), we get

$$i_{hf}(t) = A \cdot \sin(\omega_c t) + B \cdot \cos(\omega_c t) + C \cdot e^{-\frac{R}{L}t}, \tag{4.2}$$

where

- $A = \frac{U \cdot R}{R^2 + (\omega_c L)^2}$
- $B = -\frac{U \cdot \omega_c L}{R^2 + (\omega_c L)^2}$
- $C = -B$ when $i(0) = 0$.

Equation (4.2) shows that the current response is composed of two sinusoidal terms and a transient one that decreases exponentially with time with a rate of $\frac{R}{L}$. If the carrier frequency is high enough, the amplitude of the fist term in (4.2), A, becomes very small, and accordingly, it can be neglected. Therefore, the amplitude of the second term can be approximated as

$$B = -\frac{U}{\omega_c \cdot L}. \tag{4.3}$$

Thus after the third term decays to zero, (4.2) becomes

$$i(t) = -\frac{U}{\omega_c \cdot L} \cdot \cos(\omega_c t). \tag{4.4}$$

The inductance is then calculated according to the following relation

$$L = \frac{U}{\omega_c \cdot I}, \tag{4.5}$$

where U is the amplitude of the sinusoidal voltage excitation signal, I is the amplitude of the measured sinusoidal current, and ω is the frequency of the exciting signal.

Figure 4.7 shows the results for frequencies between 5 kHz and 10 kHz. The results confirm the inductance profile, which peaks in the middle between the two electromagnetic coils and decreases in a quadratic form as the mover moves away from the middle.

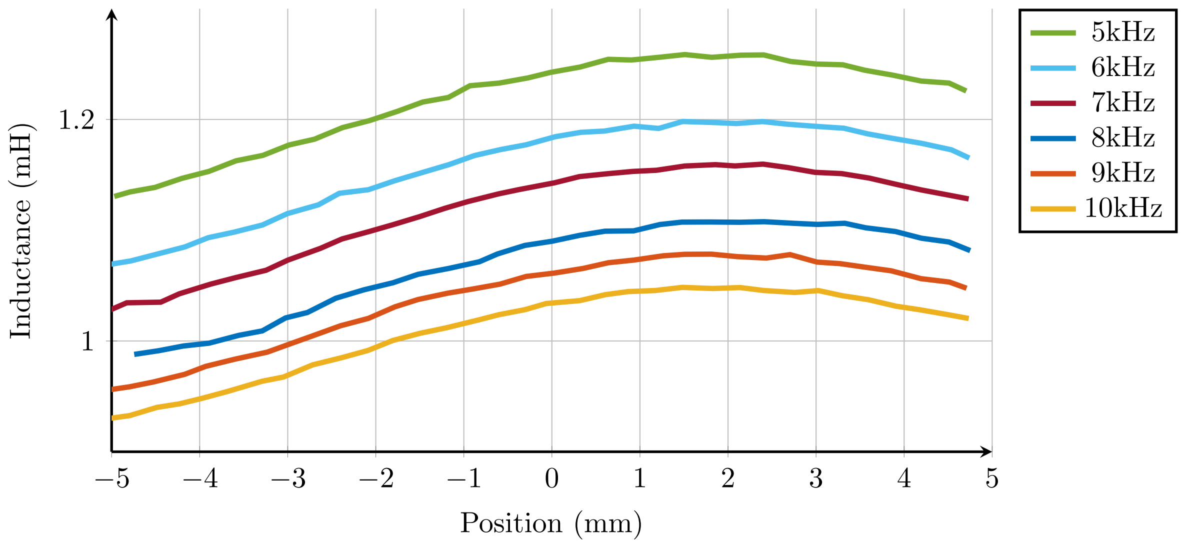

Figure 4.7: Inductance vs. position for different excitation frequencies.

4.2.2 Static Force Measurements

The main source of force acting on the mover is the excitation force (force due to the interaction between the flux produced by the coils and the flux produced by the magnet). As shown in the modelling section, in addition to the excitation force, there is a reluctance force which depends on the current amplitude and position and a cogging force which depends on the position. However, it was not possible to measure each of these forces alone due to limitations of the hardware setup such as: no access to each coil alone, no possibility to remove the magnet from the mover and keep the shoes only (to measure the reluctance force), and the strength of the static friction force compared to the cogging force. Thus the actuator could only be excited with a constant DC current and by using a load cell the force acting on the mover could be measured, which is the summation of the three magnetic forces. The mover is fixed when measuring the force, and the measurements are repeated for multiple positions of the mover.

Firstly to overcome the static friction force, the minimum excitation current/force needs to identified. This was done by increasing the currents in steps and observing the position of the mover. The minimum current is when the mover moves by overcoming the static friction.

To study the effect of the reluctance force on the total force, the current was increased linearly in steps and the total force is measured. Since the cogging force does not depend on the current, it remains constant. In the range where the excitation force is dominant, a linear relationship between current and total force is expected. This linearity starts to degrade when the reluctance force is strong enough. In the middle of the stroke, the reluctance force is expected to be zero.

The reluctance force can be measured by exciting the actuator with a high frequency voltage signal.

The actuator was excited by constant DC current while the mover is moved along the stroke in incremental steps. At each increment, the position and the output of the force sensor are saved and the average of each is taken. The results are shown in Figure 4.8.

The results of the force measurement align with the FEM model presented in the modelling section, with the relation to the form of the excitation force. The force increases gradually from the starting position until around $-1\,\mathrm{mm}$ after which it starts to decrease. With an excitation current of $2\,\mathrm{A}$ however, the reluctance is not present. There seems to be also no effect of the cogging force.

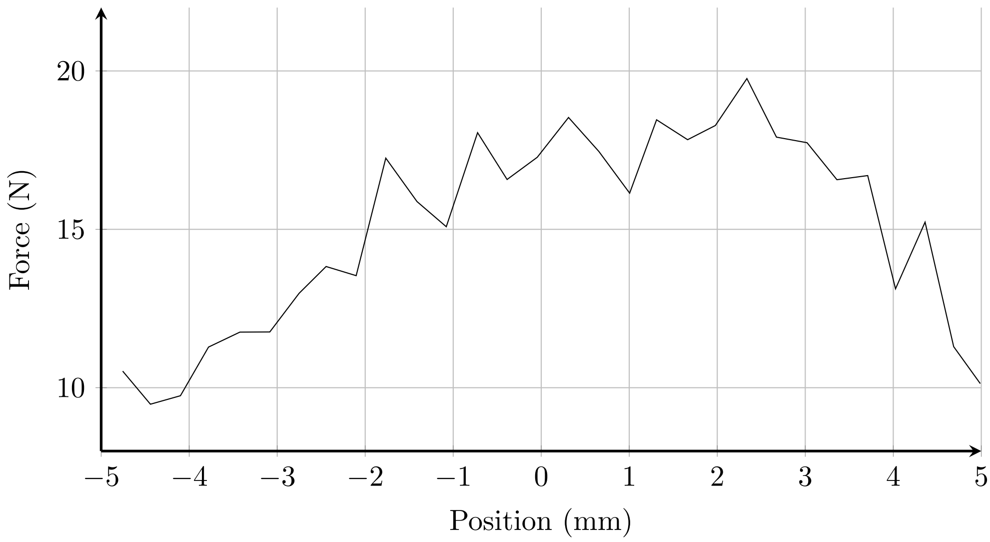

Figure 4.8: Force on the mover when the actuator is excited with a constant current of 2 A.

The same measurements were repeated for different current amplitude. The results for a positive current are shown in Figure 4.9 and for a negative current are shown in Figure 4.10.

Figure 4.11 compares the force and the inductance measurements. The two measurements align with each other and the model presented below, where both parameters peak at a specific position which is middle point between the two coils and decrease as the mover moves away from that point.

4.2.3 Force/Back e.m.f. Constant

The back electromotive force constant $f_e(x)$ from (3.40) was assumed to be constant, and will be referred to as k_e here. For estimating the constant, the actuator was externally moved and the voltage, u, and position, x were measured. Figure 4.12 shows the results of one of the measurements.

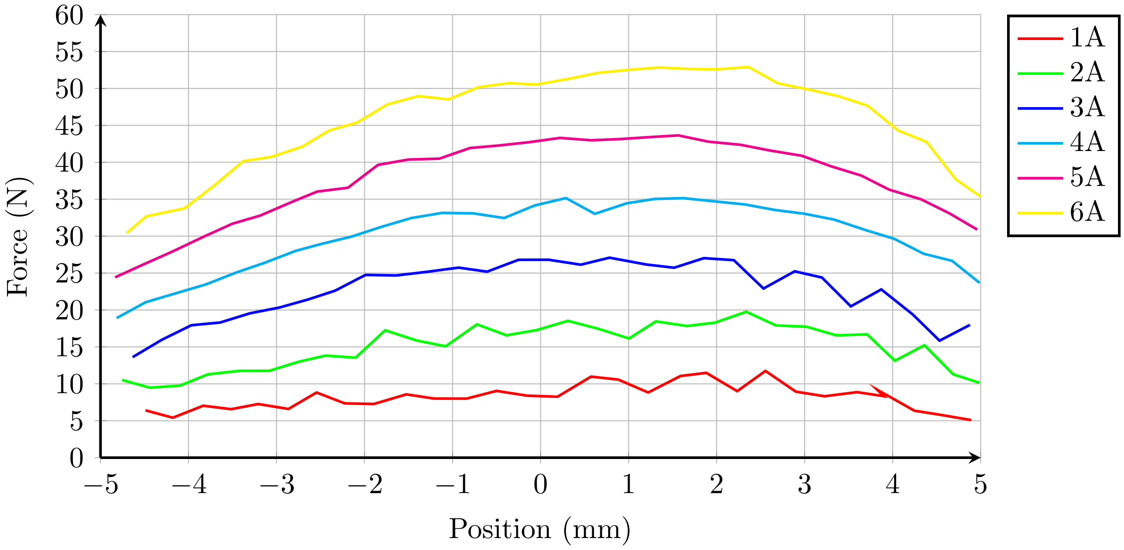

Figure 4.9: Force on the mover for different positive current excitation values.

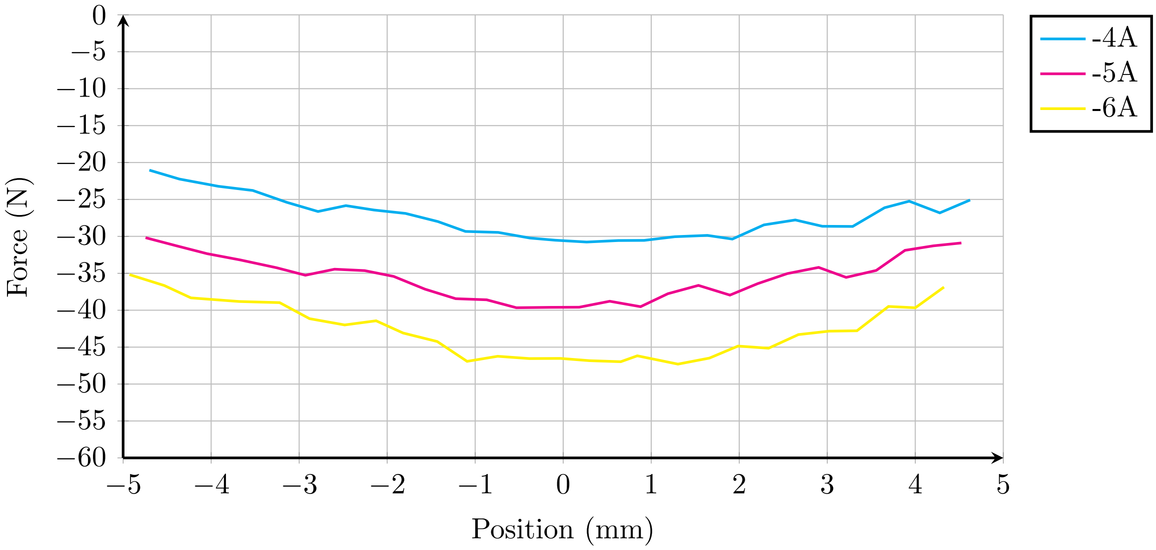

Figure 4.10: Force on the mover for different negative current excitation values.

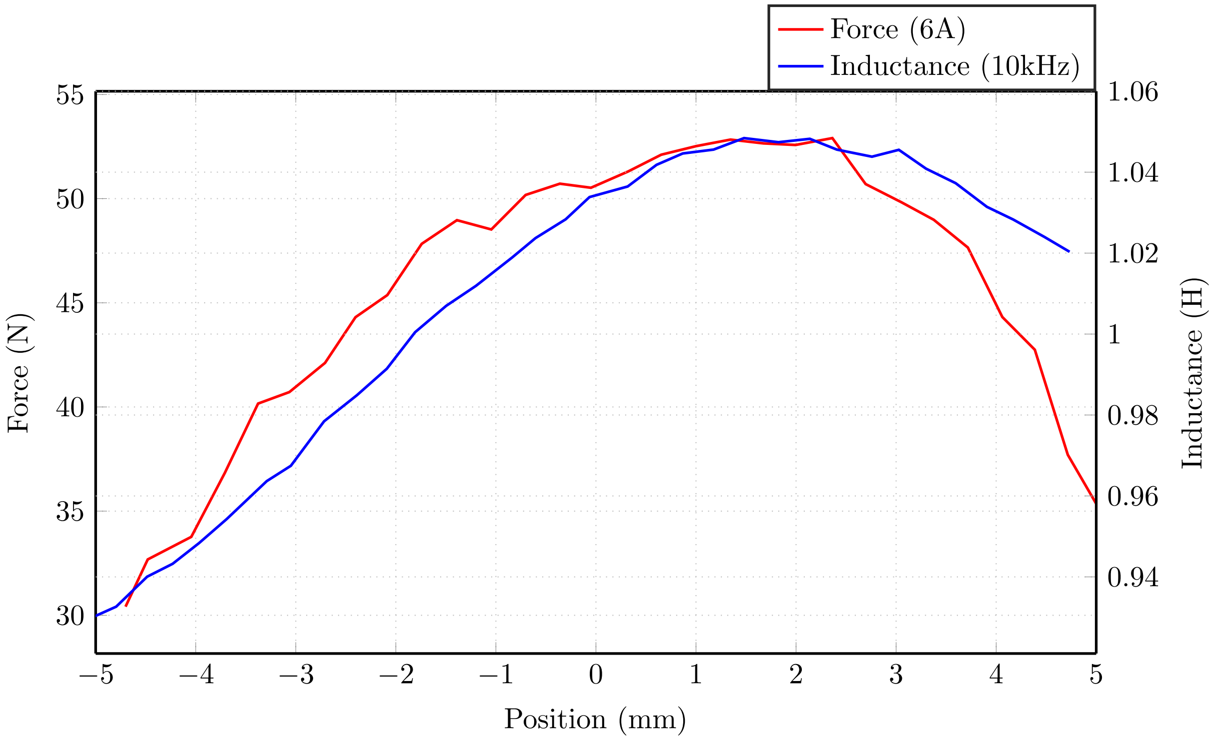

Figure 4.11: Force and inductance for different mover positions.

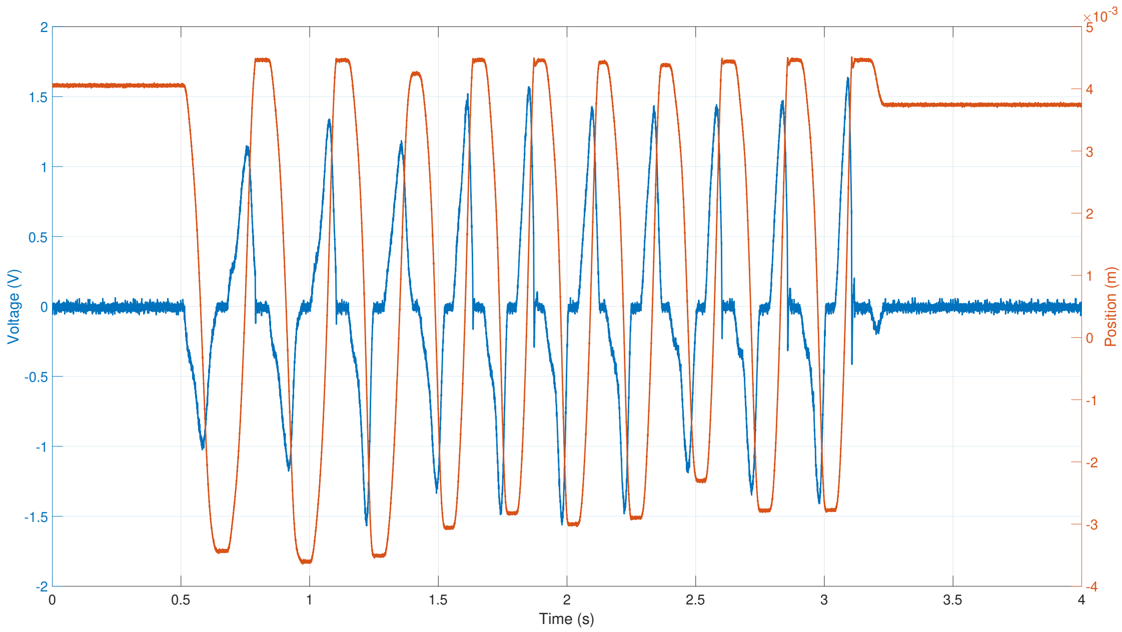

Figure 4.12: Induced voltage due to external movement.

Based on the voltage model

$$u = k_e \cdot \frac{dx}{dt} \tag{4.6}$$

and rearranging and discretizing using backward Euler

$$x_{k+1} - x_k = \frac{T_s}{k_e} \cdot u_k. \tag{4.7}$$

Since the model was assumed to be linear, using least square estimation of the form $y = a \cdot X$, a can be estimated as

$$a = \frac{X^T \cdot y}{X^T \cdot X} \tag{4.8}$$

where $y = [\Delta x(1); \Delta x(2); ...; \Delta x(N)]$ is the vector of delta position measurements, and $X = [u(1); u(2); ...; u(N)]$ is the vector of voltage measurements. The back e.m.f. constant can be estimated as $k_e = \frac{T_s}{a}$ (here T_s is the sampling time of the controller). With this approach the calculated back e.m.f. constant is 8.79 Vs/m. Using the static force measurements from the previous section and by dividing the force by the current, the force constant can be calculated. Since the force and back e.m.f. constant are identical, the two measurements are compared in Figure 4.13.

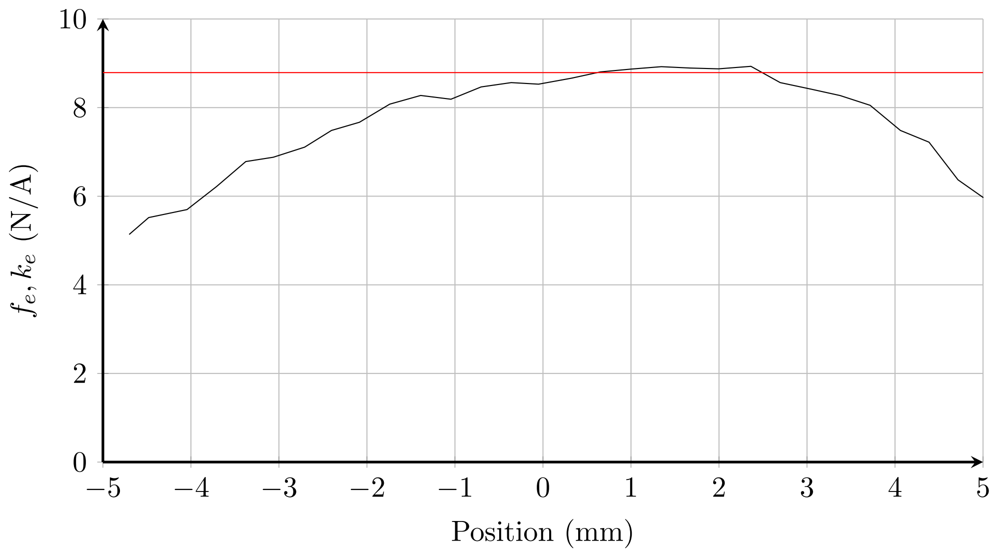

Figure 4.13: Force constant (black) from the static force measurements and back e.m.f. constant (red) from the voltage measurements.

5 Parameter and State Estimation

The speed estimator used in this work is a state space based estimator which relies heavily on the parameters of the model of the actuator. Therefore, before designing the controller and the estimator, it was essential to estimate the electrical and mechanical parameters of the actuator. In this chapter, an online parameter estimation method is introduced to estimate the electrical parameters while the actuator is at standstill. Then the mechanical parameters are estimated offline based on current and position measurements. After that, the state space estimator is introduced to estimate the speed of the actuator which is integrated to get the position signal.

5.1 Electrical Parameters

Electrical parameter estimation is the estimation of the resistance and inductance of the coil in the stator of the actuator. Estimation is usually performed by exciting the machine which an input voltage signal, measuring the resulting current, and fitting the data into a model. This works very well for linear model, or Linear Time Invariant (LTI) systems. Equation (3.44) shows the current response when a constant input voltage is applied. This is the full solution to the first order differential equation, where in most cases in literature usually the first order Taylor series approximation is used instead. In this section, it will clearly shown the benefit of using the full order solution.

Figure 5.1 shows the current response when the actuator is at standstill in one PWM period. Two observations can be made: the exponential model in (3.44), and the ringing effect of the voltage source inverter at the beginning of the switching.

Here it is worth defining the term switching instant based on Figure 5.1: it is the instant at which the input voltage shows a step change, such as at times 5 us, 10 us, 30 us, and 35 us. By measuring the current at exactly these instances, i.e. just before the ringing starts, and knowing the applied voltage and the timing, the model in (3.44) can be used to identify the electrical parameters. Since that model is nonlinear, the linear methods for parameter estimation cannot be used, instead nonlinear methods need to be applied such as the predictor-corrector form of an estimator. Such as estimator starts by predicting the value of the parameter to be estimated, based on previous value and some inputs. This prediction is then compared to real sensor measurement (in this case current) and the error between the prediction and real measurement is used as an input to a controller which drives this error to zero. The error is driven to zero when the estimated parameters converge to their true values.

The switching instant between 5 us and 10 us is called an active state since the DC voltage is applied, and between 10 us and 30 us is a passive state since at standstill zero input voltage is applied. During the passive state the model in (3.44) reduces to

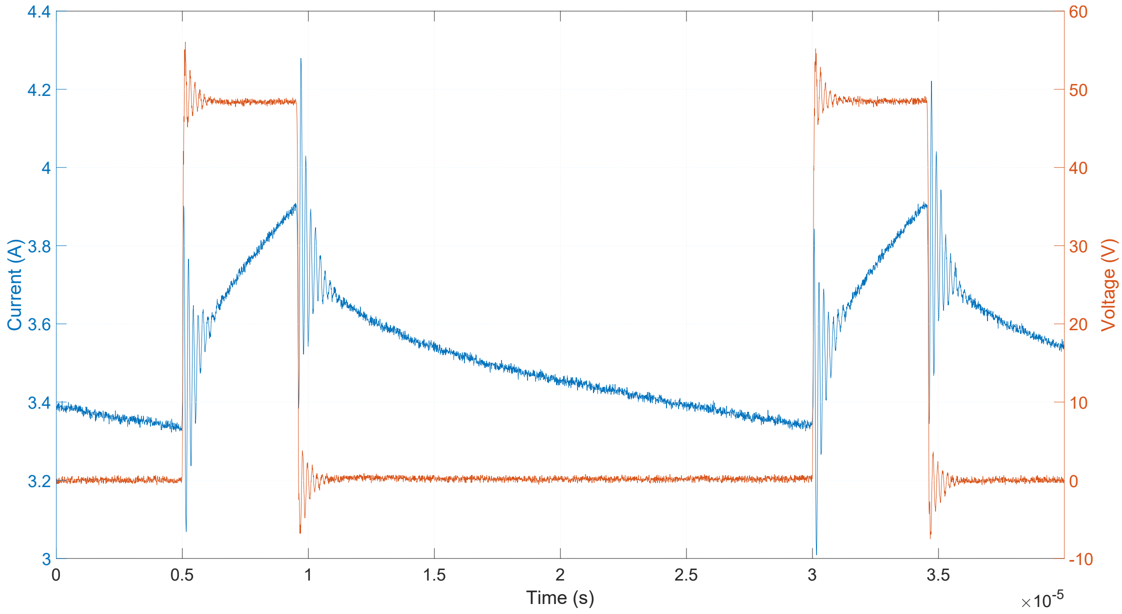

Figure 5.1: Current response in one PWM period at standstill.

$$i(k+1) = i(k) \cdot e^{-\frac{R}{L} \cdot T_s}, \tag{5.1}$$

where $i(k)$ is the current at the beginning of the switching (10 us) and $i(k+1)$ at the end (30 us), and $T_S = 20$ us.

We first start with a guess for the ratio $-\frac{R}{L}$ and use that to predict the current $i(k+1)$. Then this prediction is corrected by measuring the real $i(k+1)$ current, multiplying the difference between the real and estimated currents by controller gain and adding the result to the previous value of the ratio. The new value can then be used in the next active state to estimate again the ratio $-\frac{R}{L}$ as well R itself in the same manner.

Thus during one PWM period, and using the fourth measured switching current from the previous PWM period the prediction correction process can be repeated four times. After multiple PWM cycles, the two estimated parameters, $-\frac{R}{L}$ and R will converge to their true values. This process can be used online during operation of the actuator but only during the phases where the actuator is at standstill (beginning of operation, or in valve control applications where the valve is fixed at fully closed or fully open).

The model in (3.44) requires the use of the exponential function, which is computationally expensive especially on low cost industrial microcontrollers. An alternative would be to use a second order Taylor series approximation of the model as a balance between accuracy and computational load. In addition to that, due to the ringing effect of the inverter, the reference voltage needed for excitation needs to be high enough so that the duration of the active state is larger than the ringing and the second current to be measured has already settled down. Similarly applies to the passive state. This can be taken into account in the calculation. Given the known duration of the ringing, if the length of the active or the passive state is too short, this measurement is skipped.

The results of the estimation are compared to measurements of the resistance and inductance using an LCR meter. Figure 5.2 shows the results where an error of 1.6841% in resistance and 10.0326% in inductance is calculated.

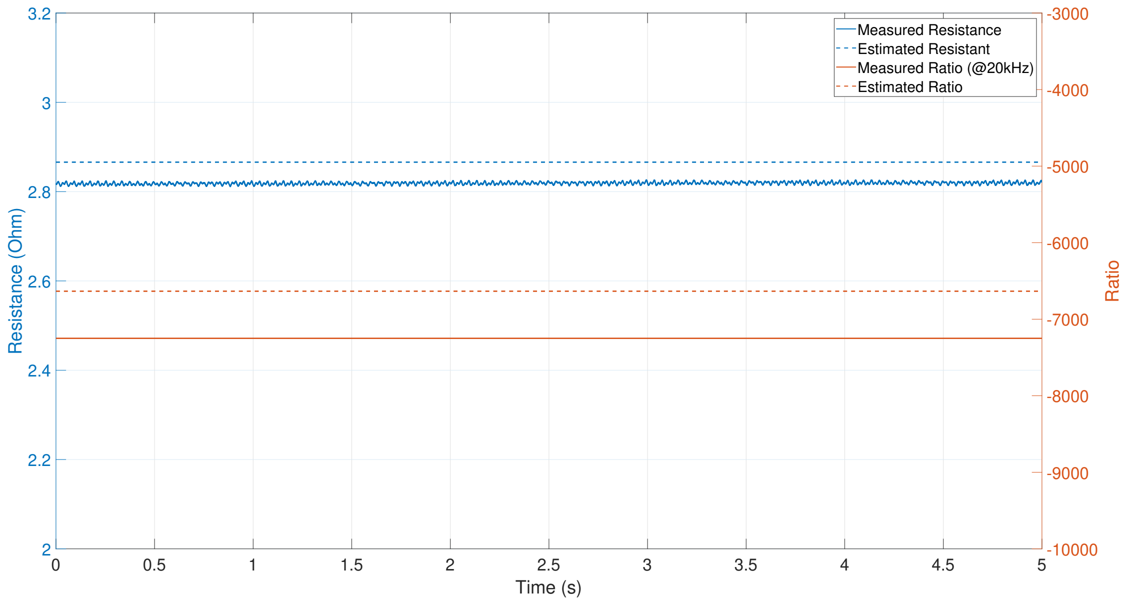

Figure 5.2: Results of the electrical parameter estimation.

5.2 Force Constant Approximation

The force constant can be calculated from the static force measurements presented in Chapter 4, by dividing by the current. As shown in Figures 4.9 and 4.10 and deducted from Chapter 3 the force is position dependent where it is maximum in the middle and decreases as the mover moves away from the middle position. The model for the force exerted in a disc magnet between two current loops shown in Chapter 3 is too complicated to be implemented on an industrial controller. Thus, a good approximation of the force constant is needed, which can be used in the state estimator, and controller design.

Figures 4.9 and 4.10 show that the force profile is more uniform as the current increases. This is expected since at higher forces, the signal to noise ratio of the sensor increases. In addition, the frictional forces are easily overcome at a high force. Thus for the curve fitting process, the force measurements for currents 4 A, 5 A and 6 A and their negative counterparts.

The force constant as a function of position can be approximated by a second order polynomial function in the form of

$$f_e^*(x) = a \cdot x^2 + b \cdot x + c \tag{5.2}$$

where x here is the position in mm. To find the values of the parameters a, b, and c, the Linear Least Squares method can be used since even though a second-order polynomial has non-linear terms (like x^2), the fitting process can still be handled by linear least squares because the unknown coefficients are linear.

First, define the matrix

$$\mathbf{F} = \begin{bmatrix} x_1^2 & x_1 & 1 \\ x_2^2 & x_2 & 1 \\ x_3^2 & x_3 & 1 \\ \vdots & \vdots & \vdots \\ x_n^2 & x_n & 1 \end{bmatrix} \tag{5.3}$$

where $x_1, x_2, \ldots x_n$ are the measured position of each data point.

Let the vector of parameters of the polynomial function be $\beta = \begin{bmatrix} a \\ b \\ c \end{bmatrix}$, and let the vector of measured force constants be $\mathbf{y} = \begin{bmatrix} y_1 \\ y_2 \\ \vdots \\ y_n \end{bmatrix}$. Then β can be calculated as

$$\beta = (\mathbf{F}^T \cdot \mathbf{F})^{-1} \cdot \mathbf{F}^T \cdot \mathbf{y}. \tag{5.4}$$

Figure 5.3 shows the results of a curve fit when approximating the force constant with the second order polynomial

$$f_e^*(x) = -0.1 \cdot x^2 + 0.13 \cdot x + 8.2, \tag{5.5}$$

as a result of the least squares estimation.

The results of the measured force constant shown in Figure 5.3 also show a small deviation between the positive and negative exaction current. This could be due to asymmetry in the manufacturing of the actuator, or due to inaccuracy in the force sensor.

One can fit the data to a higher order polynomial, or to splines and get more accurate results. The second order polynomial is a good compromise between accuracy and complexity.

5.3 Damping Coefficient

As shown in Section 3.4.1, the most dominant frictional force during movement is the viscous friction which is modeled in (3.46) as a linear function of the speed.

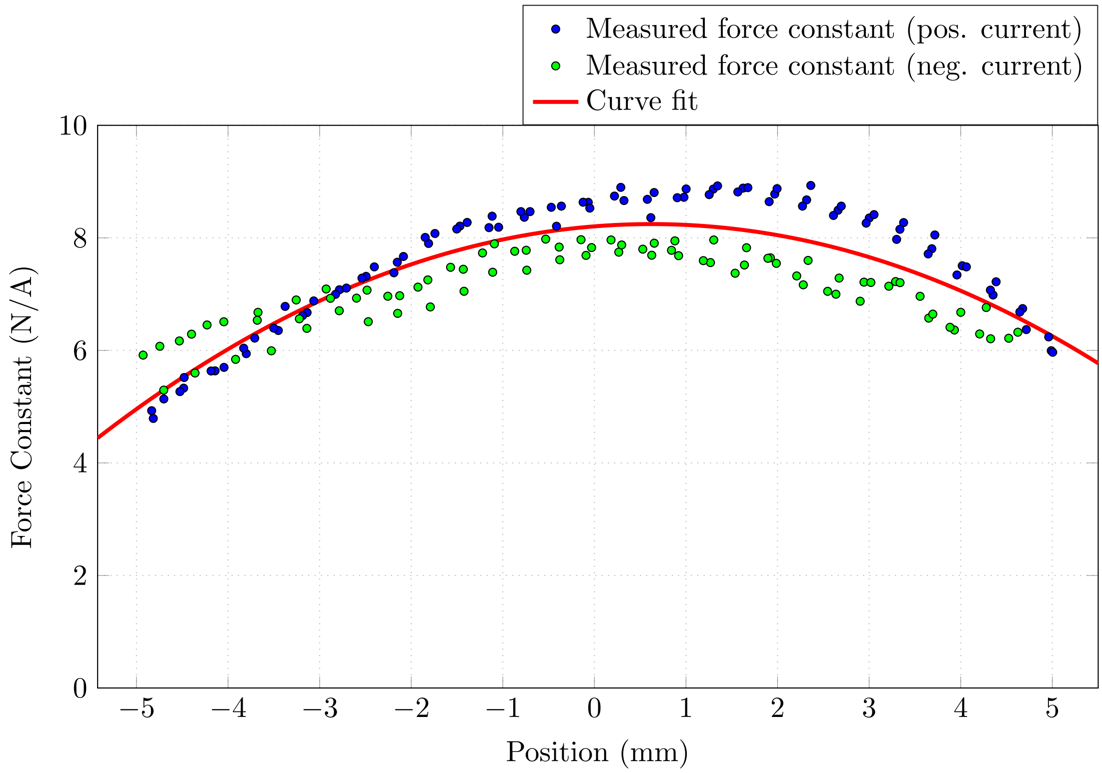

Figure 5.3: Measured force constant (calculated from the static force measurements) and the result of the curve fitting using a second order polynomial.

The simplified mechanical model (at no load and taking only viscous friction into account) of the actuator is

$$\begin{cases} \frac{dv(t)}{dt} = \frac{1}{m} \cdot (f_e(x) \cdot i(t) - \mu_v \cdot v(t)) \\ \frac{dx(t)}{dt} = v(t) \end{cases} . \tag{5.6}$$

In discrete form, (5.6) is

$$\begin{cases} v_{k+1} = (1 - T_s \cdot \frac{\mu_v}{m}) \cdot v_k + T_s \cdot \frac{f_e(x_k)}{m} \cdot i_k \\ x_{k+1} = v_k \cdot T_s + x_k \end{cases} . \tag{5.7}$$

The model in (5.7) can be written in the state space form

$$\begin{bmatrix} v_{k+1} \\ x_{k+1} \end{bmatrix} = \begin{bmatrix} (1 - T_s \cdot \frac{\mu_v}{m}) & 0 \\ T_s & 1 \end{bmatrix} \cdot \begin{bmatrix} v_k \\ x_k \end{bmatrix} + \begin{bmatrix} \frac{T_s}{m} \\ 0 \end{bmatrix} \cdot F_k, \tag{5.8}$$

where $F_k = f_e(x_k) \cdot i_k$ is the input force, and $y_k = \begin{bmatrix} 0 & 1 \end{bmatrix} \cdot \begin{bmatrix} v_{k+1} \\ x_{k+1} \end{bmatrix} + n_k$ is the measured output with measurement noise n_k.

To identify the parameter, μ_v, the actuator is excited with a constant DC current, and the current and position are measured. The input force can be calculated from the measured current and the force constant identified in (5.5). The damping coefficient was identified by minimizing the sum of square errors iteratively between the measured and estimated position. The process was repeated for all tests. Figure 5.4 shows the results of the estimation when the actuator is excited with a current of 4 A. The estimated damping coefficient for that test was calculated to be 61.45 N s/m. Table 5.1 shows the results of the estimation for different currents. It shows how the damping increases as the current increases.

Table 5.1: Estimated damping coefficient for different excitation currents.

Current (A)	μ_v (N s/m)
1	26.64
2	15.47
3	18.57
4	41.07
5	61.45

5.4 Speed Estimator

The closed loop position controller requires the feedback of position, speed, and current signals. The current signal is obtained through the current sensor, which usually installed on the inverter yielding a robust design. The position sensor on the other hand requires a more complex mechanical design since it needs to be coupled with the mover. From these

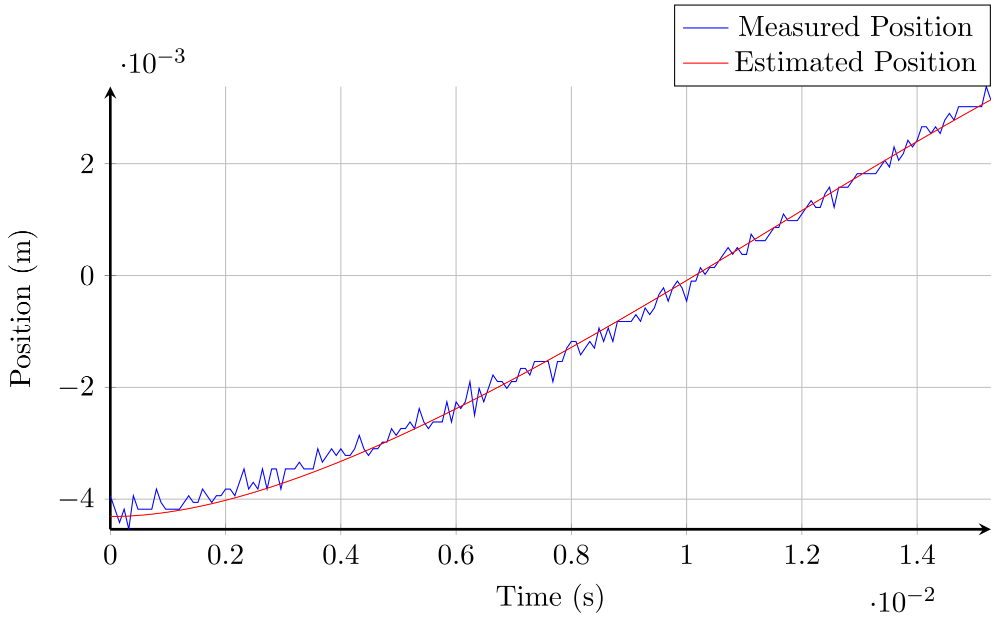

Figure 5.4: Real and estimated position based on the estimated damping coefficient.

two sensors position and current signals are fed back to the controller. Feeding back the speed signal needs more calculation. Speed is the derivative of position, however, the signal from a position sensor cannot be simply derived as this would amplify the white noise contaminating the position signal. Thus in this section, two methods for calculating the speed signal based on an observer are introduced. The first method requires the position sensor, while the second method is based only on the machine model and is used to evaluate the performance of sensorless control. Since both methods rely on model based estimation, first the general estimation method based on the Luenberger Observer is introduced. The difference between the two methods are then the state transition matrices.

5.4.1 Speed Estimation from Position Sensor

To calculate the speed from the position sensor signal, one of two methods can be used: simple linear regression or the Kalman Filter. Both methods assume that the speed is constant and hence the acceleration is zero for a certain period of time. The result is a filtered derivative signal of the position.

5.4.1.1 Linear Regression

Linear regression assumes that the speed is constant for a number of consecutive samples of the position. This implies that the relation between the position and time is linear with a constant slope. As the position signal is contaminated with noise, the slope is estimated by fitting the samples into a straight line using the linear regression method.

Let $\mathbf{T} = [0, 1, ...N-1] \cdot T_s$ be the vector of time samples for a total of N samples, and $\mathbf{X} = [x(k), x(k+1), ...x(k+N-1)]$ be the vector of measured position samples. At each instant, the estimated speed is

$$v_k = \frac{T^T \cdot (\mathbf{X} - x(k))}{\mathbf{X}^T \cdot \mathbf{X}}. \tag{5.9}$$

In other words, this calculation assumes that for an N number of sample points, the speed is constant, and thus the position has a linear relationship with time. The slope of that linear relation is calculated through linear regression.

5.4.1.2 Kalman Filter

The Kalman filter is a recursive algorithm used for estimating the state of a linear dynamic system from a series of noisy measurements. The mathematical formulation of the filter starts with the system model.

The state equation is

$$\mathbf{x}_k = \mathbf{A} \cdot \mathbf{x}_{k-1} + \mathbf{B} \cdot u_{k-1} + \mathbf{w}_{k-1}, \tag{5.10}$$

where $\mathbf{x}_k$ is the state vector at time step k, $\mathbf{A}$ is the state transition matrix, $\mathbb{B}$ is the control input matrix, u_{k-1} is the control input at time step $k-1$, $\mathbf{w}_{k-1}$ is the process noise, assumed to be Gaussian with covariance $\mathbf{Q}$.

Next is the measurement equation

$$\mathbf{z}_k = \mathbf{H} \cdot \mathbf{x}_k + \mathbf{n}_k, \tag{5.11}$$

where $\mathbf{z}_k$ is the measurement at time step k, $\mathbf{H}$ is the observation matrix, $\mathbf{n}_k$ is the measurement noise, assumed to be Gaussian with covariance $\mathbf{R}$.

First the state is predicted as follows:

$$\hat{\mathbf{x}}_k^- = \mathbf{A} \cdot \hat{\mathbf{x}}_{k-1} + \mathbf{B} \cdot u_{k-1}, \tag{5.12}$$

where $\hat{\mathbf{x}}_k^-$ is the predicted state estimate at time step k.

The covariance estimate is also predicted as

$$\mathbf{P}_k^- = \mathbf{A} \cdot \mathbf{P}_{k-1} \cdot \mathbb{A}^T + \mathbf{Q}, \tag{5.13}$$

where $\mathbf{P}_k^-$ is the predicted estimate covariance at time step k.

The measurement residual is the difference between the measurable predicted state and their measured counterparts

$$\mathbf{y}_k = \mathbf{z}_k - \mathbf{H} \cdot \hat{\mathbf{x}}_k^- \tag{5.14}$$

where $\mathbf{y}_k$ is the measurement residual at time step k.

The residual covariance is

$$\mathbf{S}_k = \mathbf{H} \cdot \mathbf{P}_k^- \cdot \mathbf{H}^T + \mathbf{R}, \tag{5.15}$$

and the Kalman gain is

$$\mathbf{K}_k = \mathbf{P}_k^- \cdot \mathbf{H}^T \cdot \mathbf{S}_k^{-1}. \tag{5.16}$$

After the Kalman gain has been calculated, the predicted state can be corrected by

$$\hat{\mathbf{x}}_k = \hat{\mathbf{x}}_k^- + \mathbf{K}_k \cdot \mathbf{y}_k, \tag{5.17}$$

as well as the covariance estimate

$$\mathbf{P}_k = (\mathbf{I} - \mathbf{K}_k \cdot \mathbf{H}) \cdot \mathbf{P}_k^- \tag{5.18}$$

where $\hat{\mathbf{x}}_k$ is the updated state estimate (position and speed), $\mathbf{P}_k$ is the updated estimate covariance, $\hat{\mathbf{x}}_k^-$ is the predicted state estimate and $\mathbf{P}_k^-$ is the predicted estimate covariance before the measurement is taken into account, $\mathbf{y}_k$ is the difference between the actual measurement and the predicted measurement, $\mathbf{S}_k$ is the covariance of the innovation, and $\mathbf{K}_k$ is the Kalman gain, which determines how much the predictions should be corrected based on the measurement.

The Kalman Filter in discrete form can be used to estimate the speed (in this case the filter is a differentiator, so the model matrices will be given the subscript $diff$).

Let the state vector $\mathbf{x}_{diff}$ be

$$\mathbf{x}_{diff} = \begin{bmatrix} x \\ \dot{x} \end{bmatrix} \tag{5.19}$$

where x is the position and $\dot{x}$ is the speed.

The state transition matrix $\mathbf{A}_{diff}$ and observation matrix $\mathbf{H}_{diff}$ are defined as

$$\mathbf{A}_{diff} = \begin{bmatrix} 1 & T_s \\ 0 & 1 \end{bmatrix}, \quad H_{diff} = \begin{bmatrix} 1 & 0 \end{bmatrix} \tag{5.20}$$

where T_s is the sampling time.

The process noise covariance $\mathbf{Q}_{diff}$ and measurement noise covariance $\mathbf{R}_{diff}$ are typically chosen based on the characteristics of the system and sensors

$$\mathbf{Q}_{diff} = \begin{bmatrix} q_1 & 0 \\ 0 & q_2 \end{bmatrix}, \quad R_{diff} = \begin{bmatrix} r \end{bmatrix} \tag{5.21}$$

where q_1, q_2, and r are noise variances.

Using these matrices, the prediction and update steps in the Kalman filter are performed as described above. This results in a filtered estimate of the position and speed, which is less sensitive to noise compared to direct differentiation methods.

Since the state transition matrix, A, the process noise covariance matrix, Q, and the measurement noise covariance matrix, R, are constant, the Kalman gain matrix can be precalculated offline starting from an initial covariance matrix P_0. A simulation is run where at each time step a new P_k and K_k are calculated. The length of the simulation is long enough so that the elements of the matrices converge to a constant value. Figure 5.5 shows the results of a simulation. It shows the change of the Kalman gains with each iteration until both parameters converge to their final values.

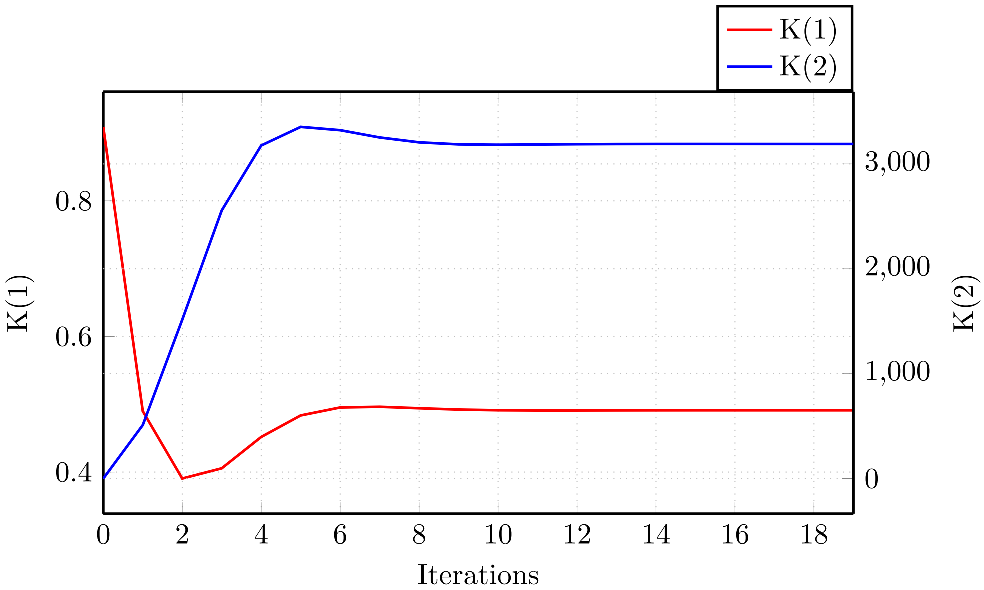

Figure 5.5: Kalman gain matrix parameters.

The calculated gains can then be used to estimate the position and speed. An example is shown in Figure 5.6 where a position signal is generated and contaminated with Gaussian white noise. This Kalman filter with the calculated gains is then used to estimate the speed. The result is compared with estimation using simple linear regression.

5.4.2 Speed Estimation from Actuator Model

To evaluate speed and position estimation without a position sensor, the speed was estimated from the actuator model and current sensor only. For that the Luenberger stater observer is implemented. The Luenberger observer [26] is a state estimator of the predictor corrector type used for estimating the states of an LTI system. Based on a state space model of the system, first the states are predicted, and then the predicted states are corrected using the sensor measurements. The controller part of the estimator drives the error between the measured and estimated state to zero, which drives the unmeasurable states to their correct values. In this project, the Luenberger observer was used mainly as a speed estimator using a linear simplified model of the actuator (parameters in (3.40) assumed constant) and current measurements from a current sensor.

The prediction and correction equations of the Luenberger Observer are identical to the Kalman Filter presented in the previous section. The main difference lies in the calculation of the observer gain. The calculation of the observer gain in the Luenberger is simpler where a combination of pole placement and tuning are used.

The electrical model of the actuator in discrete form is

$$i_{k+1} = (1 - T_s \cdot \frac{R}{L}) \cdot i_k - T_s \cdot \frac{f_e}{L} \cdot v_k + T_s \cdot \frac{1}{L} \cdot u_k. \tag{5.22}$$

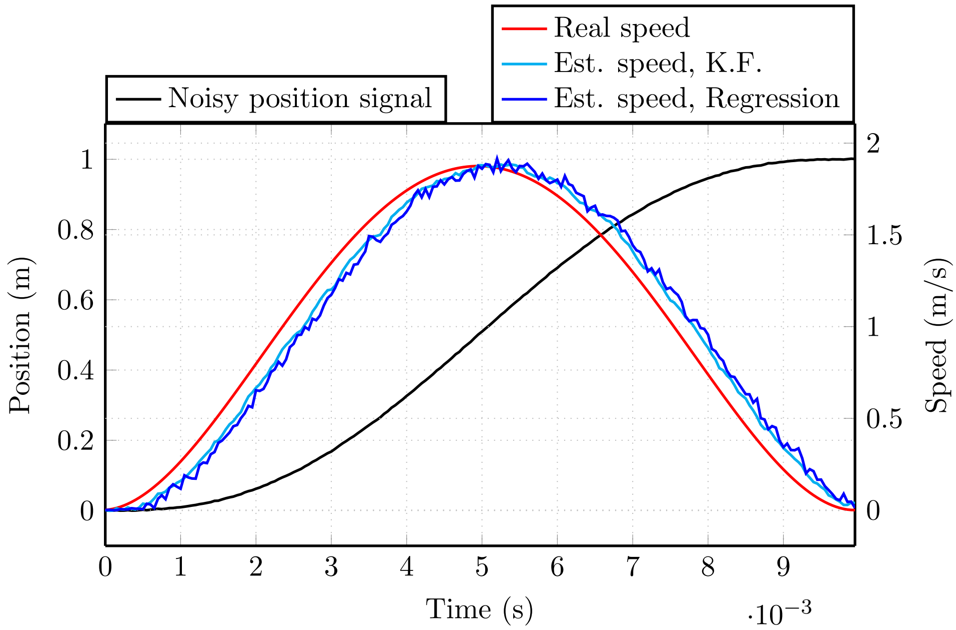

Figure 5.6: Comparison of speed estimation of a noisy position signal between the Kalman Filter and linear regression.

A simple mechanical model where the speed is assumed constant within one sample is

$$\begin{cases} v_{k+1} &= v_k, \\ x_{k+1} &= x_k + T_s \cdot v_k. \end{cases} \tag{5.23}$$

This relies solely on the electrical model (back e.m.f.) to estimate the speed to minimize the error between the measured and estimated current. However, this would introduce a delay in the estimated speed and strongly reduce the estimator dynamics.

The dynamics of the estimated speed can be increased by calculating the speed based on the current and then correcting the estimation. This model has the form

$$\begin{cases} v_{k+1} &= T_s \cdot \frac{f_e}{m} \cdot i_k + v_k, \\ x_{k+1} &= x_k + T_s \cdot v_k. \end{cases} \tag{5.24}$$

After discretization the observer model can be derived. The state vector is comprised of the current, speed, and position states

$$\mathbf{x}_k = \begin{bmatrix} i_k \\ v_k \\ x_k \end{bmatrix}, \tag{5.25}$$

and the state transition matrix is

$$\mathbf{A} = \begin{bmatrix} 1 - T_s \cdot \frac{R}{L} & -T_s \cdot \frac{f_e}{L} & 0 \\ T_s \cdot \frac{f_e}{m} & 1 & 0 \\ 0 & T_s & 1 \end{bmatrix}, \tag{5.26}$$

where here the force and back e.m.f. constants are assumed constant.

The input matrix is

$$\mathbf{B} = \begin{bmatrix} T_s \cdot \frac{1}{L} \\ 0 \\ 0 \end{bmatrix}, \tag{5.27}$$

and the measurement matrix is

$$\mathbf{H} = \begin{bmatrix} 1 & 0 & 0 \end{bmatrix}. \tag{5.28}$$

Due to the simplified mechanical model used in the estimator, at low to zero speeds the back e.m.f. signal is very low that the estimated speed and position signals are inaccurate. Thus the speed and position can only be estimated when the real speed of the actuator is above a certain threshold, or in other words, when the back e.m.f. due to the moving magnet is large enough. This imposes a challenge since the typical motion profile of an actuator is point to point motion, whereby the speed and the beginning and end is typically zero (soft landing). One way to achieve that without a position sensor, is if the speed and position controller switches to open loop control at the beginning and end of the motion. Thus a speed threshold needs to be identified below which the controller switches to open loop, since this threshold depends on the noise in current measurement as well as the accuracy of the actuator model.

6 Controller Design

In the previous sections it was shown that the actuator can be modelled as a Single Input Single Output (SISO) system with the input being the excitation voltage and the output the position of the mover. In this chapter, the design of the controller which controls the mover will be presented. Different types of controllers were investigated based on the general application requirements. As mentioned before, these can be fastest transition time (opening and closing time) and minimum impact speed to minimize mechanical wear. To achieve that, different controllers in the family of linear and nonlinear control systems are investigated.

This chapter starts with the linear control type and introduces the cascaded and the state space controllers. The state controller is then extended with trajectory generation. Then the time optimal nonlinear controller is introduced and designed for control of the actuator. Results of these controllers are then shown in the next chapter.

6.1 Linear Control

Linear controllers are perhaps the most widely used type of control in the industry. They are easy to design and implement, and usually do not take a lot of resources making them ideal for applications where cost is a big factor. They are based on negative feedback where the input to the system is calculated as

$$u = k_P \cdot (x_{ref} - x), \tag{6.1}$$

where k_P is the controller gain, x_{ref} is the reference input, and x is the measured or estimated output.

This simplest form of control is called a proportional gain control since the control input is proportional to the error between the reference and feedback signal. This kind of controller, however, minimizes the error but does not drive it to zero in the presence of any disturbances (such as load forces). To drive the error to zero at steady state, an integral part is needed so that

$$u = k_P \cdot (x_{ref} - x) + k_I \cdot \int (x_{ref} - x) dt, \tag{6.2}$$

where k_I is the integral gain. To reduce overshoot and improve stability, an additional derivative term can be added to the controller

$$u = k_P \cdot (x_{ref} - x) + k_I \cdot \int (x_{ref} - x) dt + k_D \cdot \frac{d(x_{ref} - x)}{dt}, \tag{6.3}$$

where k_D is the derivative gain.

This type of controller is the well established Proportional Integral Derivative (PID) controller whose transfer function is

$$C(s) = \frac{U}{X_{ref} - X} = k_P + \frac{1}{s} \cdot k_I + s \cdot k_D. \tag{6.4}$$

Linear systems analysis assumes that the plant model (relation between the input and output in the frequency domain) is linear. This implies that in the model in (3.40), the inductance and back e.m.f/force constant are assumed to be constant and do not depend on the position. In addition to that, the reluctance and cogging forces are considered disturbances and only the excitation force is considered in the force generation.

The transfer function mapping output to the input is then

$$G(s) = \frac{X}{U} = \frac{f_e}{s \cdot (s^2 \cdot L \cdot m + s \cdot R \cdot m + f_e^2)}. \tag{6.5}$$

Figure 6.1 shows the signal flow diagram of the closed loop position control of the actuator where the closed loop transfer function from the reference position to the output position is

$$H(s) = \frac{X}{X_{ref}} = \frac{C(s) \cdot G(s)}{1 + C(s) \cdot G(s)}. \tag{6.6}$$

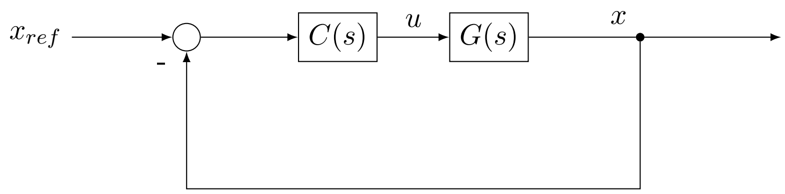

Figure 6.1: Closed loop position control signal flow diagram.

6.1.1 Cascaded Control

In control of electric drives, in addition to the speed and/or position, the current in the motor is always measurable where the current sensor is ideally placed inside the inverter. This gives the advantage that the current can also be used as a feedback signal for an inner current control loop. The controller presented in the previous section is then extended to have one inner current control loop and one outer position control loop. This is what is called a cascaded control where two or more loops are cascaded to form the final controller. The advantages compared to single loop control are better disturbance rejection (since the inner loop can quickly respond to disturbances) and an improved response time of the system. In [53] a study was done to compare the performance of single loop control vs. cascaded control for a third-order system. The authors confirm the superior disturbance rejection performance of the cascaded control.

The single loop controller shown in Figure 6.1 can be extended to the cascaded position, speed, and current controller shown in Figure 6.2. This is the standard controller abundant in the industry where there are three control loops: inner current control loop, middle speed control loop, and outer position control loop. All control loops are based on the proportional integral type of controllers.

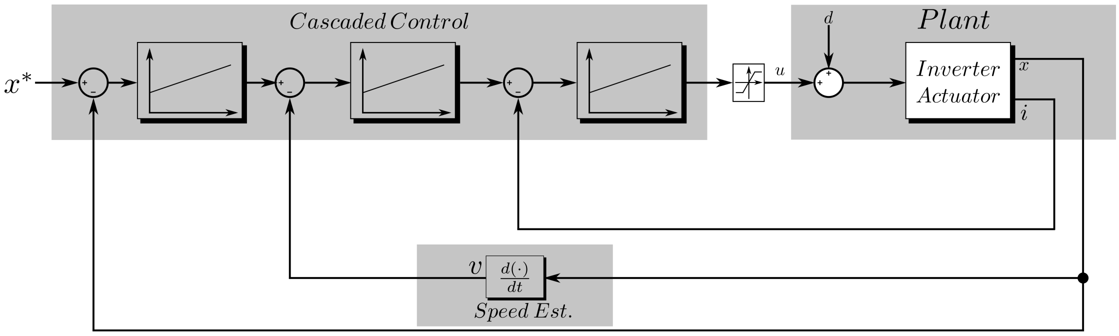

Figure 6.2: Cascaded position, speed, and current controller.

As a rule of thumb, a controller of an outer loop was tuned to have a bandwidth ten times slower than the next inner loop.

Since there is no direct speed signal from the position sensor, the position signal cannot be simply derived due to the amplified noise. Thus the feedback speed signal is the output of the state estimator.

6.1.2 State Space Control

Another controller investigated was the state space controller shown in Figure 6.3. The state space controller is in fact the cascaded controller but when all integrators removed from all three controllers.

In [54], a comparative study of cascaded vs. state space control is done for the control of a DC motor. The authors show that the main advantage of thee state space controller is the faster response time due to the lack of individual computation of each control loop of the cascaded control. The authors argue that this can be improved by using feedforward control for each loop.

6.1.3 Trajectory Generation

The state space controller from the previous section can be extended by controlling the states to follow a precalculated trajectory. There are different ways to generate state trajectories that would fulfill the application requirements. Trajectory generation itself is a big research topic, the reader can refer to the book in [55] for a deeper dive into it.

Here flatness based trajectory generation is used to calculate the trajectories of the input and the states. The trajectory planned should result in trajectories for the input and the states for minimum travel time and which respect the constraints on the input

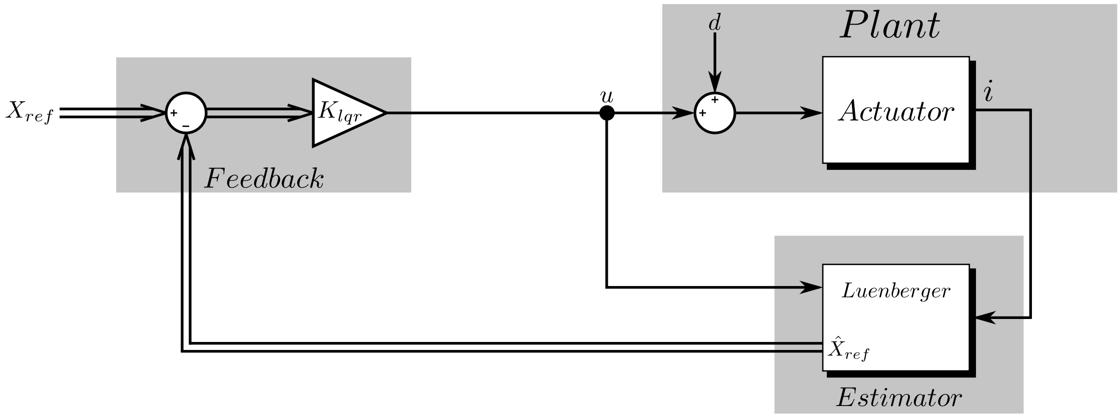

Figure 6.3: State space controller.

and the states. These constraints are lower than the actual constraints in order to keep a reserve for disturbances which are not modeled and the load.

Differential flatness is another form of system inversion, normally used to transfer non-linear systems to linear ones [56]. A system is differentially flat, if the inputs and the states of the system can be expressed as a function of the output and its derivatives, here called the flat output. Flatness based control is important where feedforward and tracking controllers are implemented [57, 58, 59, 60] and specifically for electromagnetic actuators [2, 17, 16, 18]. The main differences lie in the parametrization of the flat output where often polynomials or B-Splines [59] are used.

Let y be the flat output which is the position of the mover. Then, the third state of the state vector, x, is the position

$$s(t) = y(t). \tag{6.7}$$

The second state, the speed, is simply the derivative of the position

$$v(t) = \frac{dy(t)}{dt}. \tag{6.8}$$

The third state, the current, can be expressed as a function of the acceleration based on (3.40).

Each state can represented as a function of the output and its derivatives. The second step is to parametrize the output in a smooth differentiable function. The flat output has to be at least n-times differentiable [57], where n is the number of the states. Here, a polynomial reference trajectory of fifth order is chosen that does not violate the constraints. As a function of time, it is represented as

$$y(t) = a_5 \cdot t^5 + a_4 \cdot t^4 + a_3 \cdot t^3 + a_2 \cdot t^2 + a_1 \cdot t + a_0. \tag{6.9}$$

The target is to find the values of the constants in (6.9) such that the resulting trajectory would satisfy the initial and final conditions, and does not violate the constraints on the input and the states, in the minimum time.

Let the initial position, speed, and acceleration be zero: $y(0) = y^{(1)}(0) = y^{(2)}(0) = 0$. This leads to $a_2 = a_1 = a_0 = 0$.

The mover is required to reach its final position, y_f, at time, t_f, with minimal speed and acceleration which implies $y_f^{(1)} = y_f^{(2)} = 0$. Then we can form a system of 3 equations as

$$\begin{cases} y(t_f) = a_5 \cdot t_f^5 + a_4 \cdot t_f^4 + a_3 \cdot t_f^3 = y_f \\ y^{(1)}(t_f) = 5 \cdot a_5 \cdot t_f^4 + 4 \cdot a_4 \cdot t_f^3 + 3 \cdot a_3 \cdot t_f^2 = 0 \\ y^{(2)}(t_f) = 20 \cdot a_5 \cdot t_f^3 + 12 \cdot a_4 \cdot t_f^2 + 6 \cdot a_3 \cdot t_f = 0 \end{cases} \tag{6.10}$$

If t_f is known, then (6.10) becomes a system three equations and three unknowns, and we can solve for the constants a_5, a_4, and a_3. The final time, t_f, should be minimized without violating the constraint on the input voltage, u, and the current, i. To find t_f, the procedure presented in [59] is used and illustrated in Table 6.1.

Table 6.1: Procedure to find t_f.

Initialize	Let $t_1 = 0$ and choose feasible t_2
Step 1	Choose $t_f = \frac{t_2 - t_1}{2}$.
Step 2	Solve (6.10) for a_5, a_4, and a_3.
Step 3	Calculate the trajectories for u and i.
Step 4	Check if $u < U_{max}$ and $i < I_{max}$.
Step 5	If yes, let $t_2 = t_f$; else $t_1 = t_f$.
Step 6	Go back to Step 1 or stop if accuracy is met.

6.2 Time Optimal Control

The requirements on the valve actuation applications are usually minimum time transition from one state to another (open to close and vice versa). In addition to that, impact shall be avoided at the end of the transition to minimize mechanical wear. Such requirements often lead to bang-bang and minimum time controllers. In this section, the concept of time optimal control will be introduced, starting from a simple double integrator and going into the actuator control.

6.2.1 The Double Integrator

A double integrator system can be represented as two integrators cascaded together in series, where each integrator represents the state of the system, for example speed and position. A simple dynamic system is a "block on ice" where a block with a mass m is pushed with a force f on an ice surface with zero friction, leading to an acceleration a, speed v, and position x. This is a single input single output system with the force f as an input and the position x as an output and is represented by the set of equations

$$\begin{cases} \frac{dx(t)}{dt} = v, \\ \frac{dv(t)}{dt} = \tau \cdot f, \end{cases} \tag{6.11}$$

where $\tau = \frac{1}{m}$ is the mechanical time constant. Such a system can be represented in Figure 6.4.

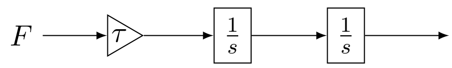

Figure 6.4: The double integrator system.

By applying Pontraygin's Maximum Principle, the time optimal control for the double integrator leads to a bang-bang solution [61] where the input switches from zero to, maximum to minimum, and minimum to zero (three times, number of states plus 1), to bring the state to the origin in a minimum time. Such a time optimal control law has the form

$$\begin{cases} u(t) = \tau \cdot \text{sign}(f_{to}(x_e) - v) \\ f_{to}(x_e) = \text{sign}(x_e) \cdot \sqrt{2 \cdot \tau \cdot |x_e|} \end{cases} \tag{6.12}$$

where x_e is the error between the input reference and the feedback.

The control law can be illustrated in cascaded form as shown in Figure 6.5.

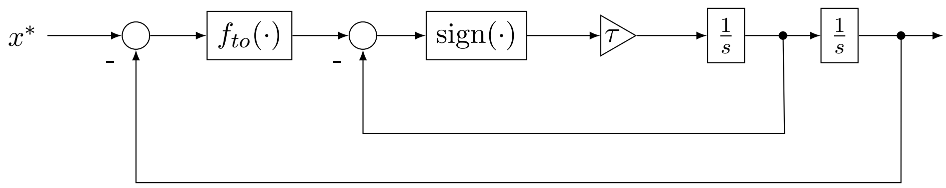

Figure 6.5: Signal flow diagram of the time optimal control of the double integrator.

Figure 6.6 shows the results of a small simulation of time optimal control of the double integrator (assuming $\tau = 1$).

The double integrator system is an ideal representation of the real system. The time optimal control law cannot be realistically implemented on a real system. One simple difference for example, would be the presence of damping (viscous friction). Figure 6.7 shows the results of the same simulation but when a slight damping is added to the double integrator. The chattering of the input can be seen clearly after the switch from minimum to maximum.

Another difference would be actuation, where on some systems it is not possible to instantaneously switch the input from one maxima to another. Therefore, small model uncertainties in the real system make the time optimal controller unrealistic. These drawbacks are addressed in the next section.

6.2.2 Proximate Time Optimal Control

In order to address these drawbacks, Workman et. al [62] have proposed a proximate time optimal (can also be found in literature as "near" or "quasi" time optimal) for systems with dynamics similar to the double integrator and called it PTOS. The outer sign

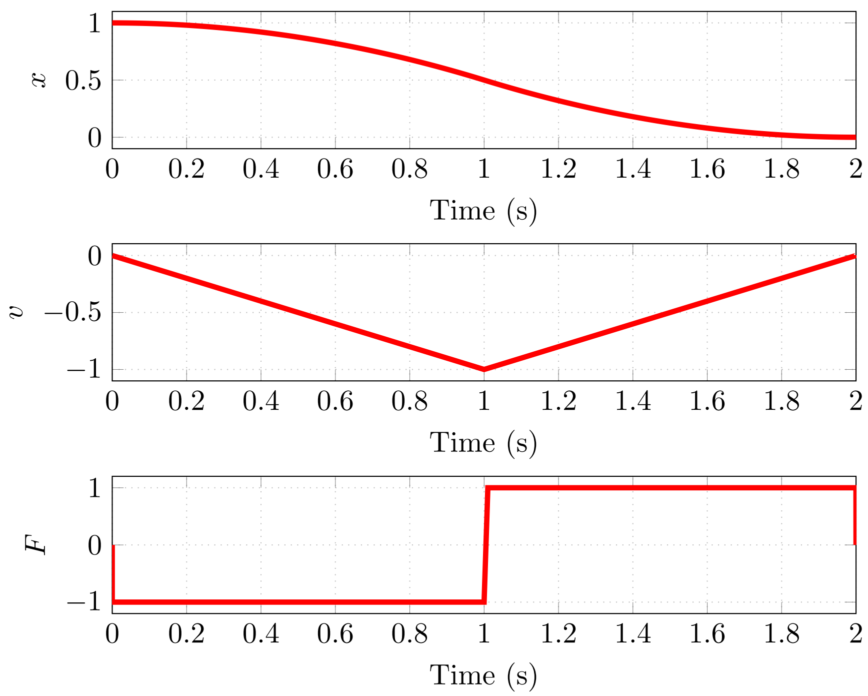

Figure 6.6: Time optimal simulation of the double integrator system.

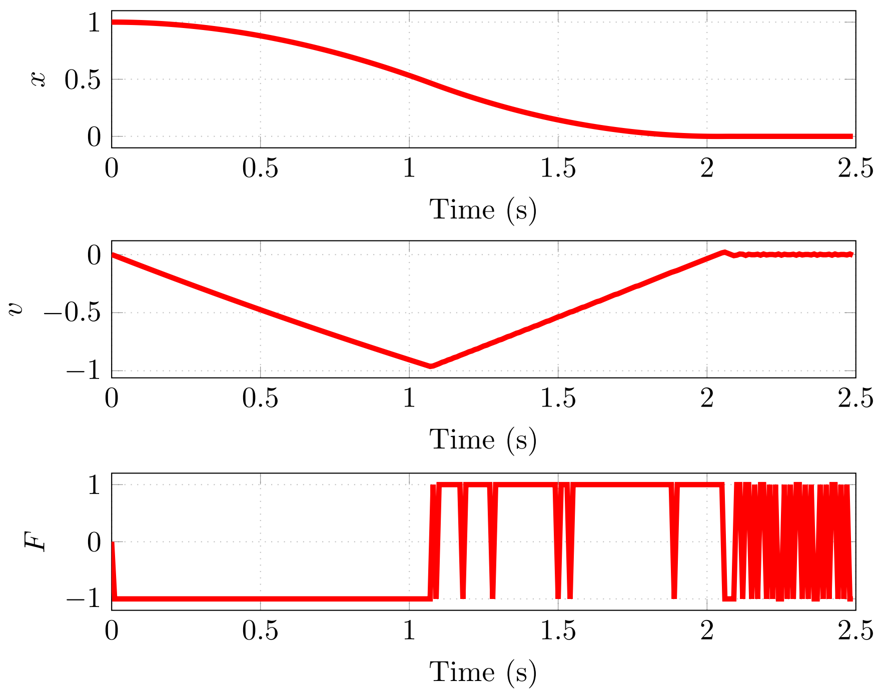

Figure 6.7: Time optimal simulation of the damped double integrator system.

function is replaced with a sat function, where the output of the controller can change linearly with a defined slope between the upper and lower boundaries and saturates at the boundaries. In addition to that, the inner sign function is only applied when the error in the control variable is larger than a defined value. If the error is small enough, the controller switches to linear controller as a function of the states. The control of (6.12) becomes

$$\begin{cases} u(t) = \tau \cdot \mathrm{sat}(k_2 \cdot (f_{pto}(x_e) - v)) \\ f_{pto}(x_e) = \begin{cases} \frac{k_1}{k_2} \cdot x_e & if|x_e| <= x_l \\ \mathrm{sign}(x_e) \cdot (\sqrt{2\tau\alpha|x_e|} - \frac{1}{k_2}) & if|x_e| > x_l \end{cases} \end{cases} \tag{6.13}$$

where k_2 defines the finite slope approximation of the outer sign function, x_l is error threshold below which the controller switches to a linear controller, α is called the "acceleration discount factor" and is between zero and one, and k_1 is the proportional controller gain (in the region close to the origin the controller is the well known linear quadratic regulator with gains k_1 and k_2).

Figure 6.8 shows the signal flow diagram of the PTOS controller where the two major changes can be seen: the f_{to} function is replaced with the f_{pto} function from (6.13), and the sign function after the speed error calculation has been replaced with the gain k_2 and a sign function.

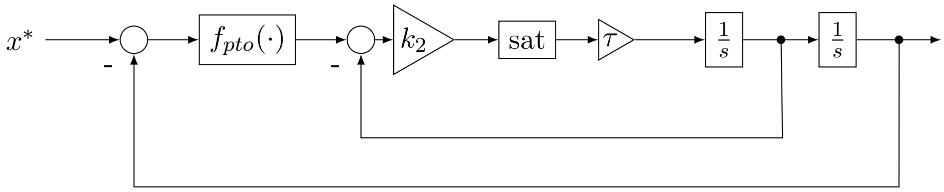

Figure 6.8: Signal flow diagram of the PTOS control of the double integrator.

Stability of the control system is ensured by imposing the following conditions [62] on the factors

$$\begin{cases} k_2 = \sqrt{\frac{2k_1}{\alpha\tau}} \\ x_l = \frac{1}{k_1} \end{cases} \tag{6.14}$$

Figure 6.9 shows simulation results for the two controllers when applied to a double integrator system with $\tau = 1$, where the aim of the controller is to drive the system from the initial state to the origin. The simulation shows that the time optimal controller has faster response with the chattering effect clearly seen when the system reaches the final state. It also shows the abrupt switching from the minimum to the maximum has been replaced by a smoother transition with the PTOS controller, which would represent more closely a real world system, such as the change of current in the actuator.

Replacing the speed error sign function with a gain and saturation function addresses the abrupt actuation limitation of a real system, where instead of the sudden switch of

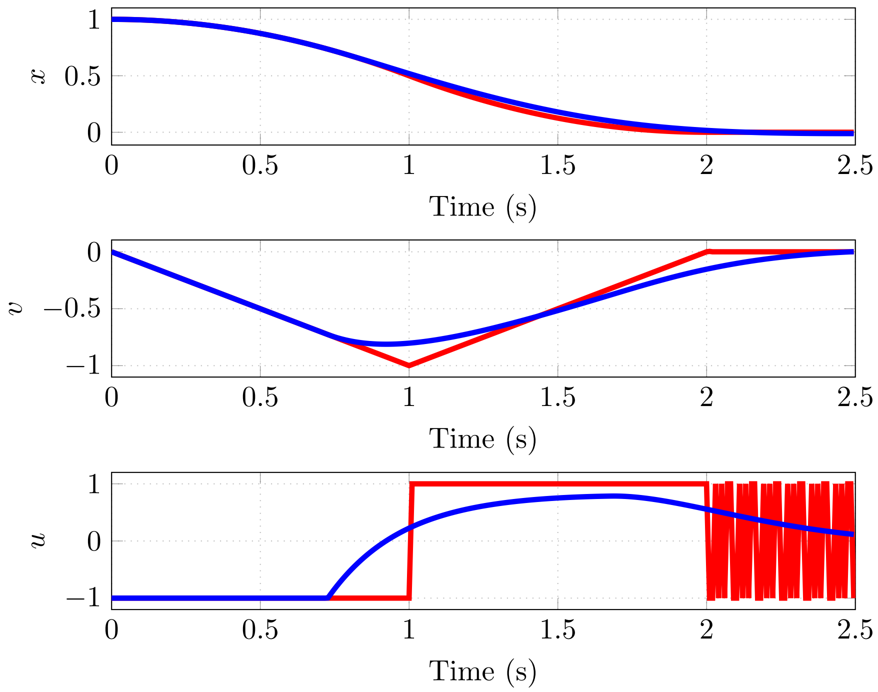

Figure 6.9: Time optimal (red) vs. PTOS (blue) of the double integrator system.

the input from one maxima to the other, the switch is with a small time duration, as can be seen from Figure 6.9.

The new switching function f_{pto} introduces the acceleration discount factor α. Figure 6.10 shows the results of three different simulations when α is changed keeping all other independent parameters the same. As α decreases, the applied input during the deceleration phase decreases, and with it the deceleration rate decreases and the state reaches the origin at a delayed time.

6.2.3 Proximate Time Optimal Control of the Actuator

The PTOS controller presented before is a position controller aimed for systems that have double integrator like dynamics. However, the model of the actuator from the input voltage to output position is a third order system. Here the PTOS controller is adopted for the position and speed control, and is cascaded with the linear proportional integral control to control the current of the actuator as shown in Figure 6.11. This cascaded type of control models the actuator as one system with the current as input and position as output.

The transfer function from the input current to the output position is not linear according to the model of the actuator. However, the electrical dynamics are around ten times faster than the mechanical dynamics allows for such a controller design. Prerequisite here is a highly dynamic current controller.

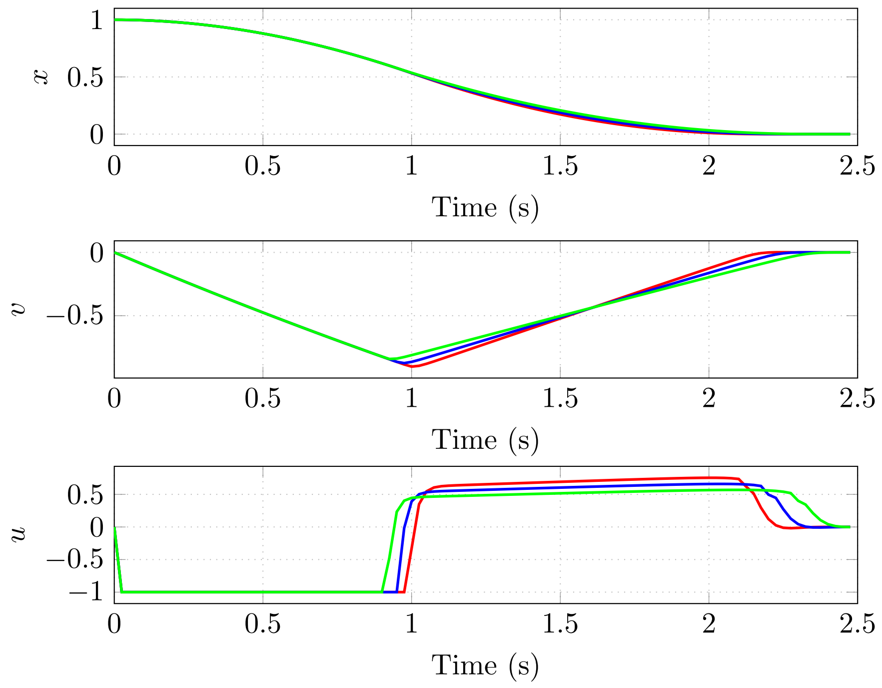

Figure 6.10: Simulation of PTOS for different values of α (red $\alpha = 0.9$, blue $\alpha = 0.8$, green $\alpha = 0.7$).

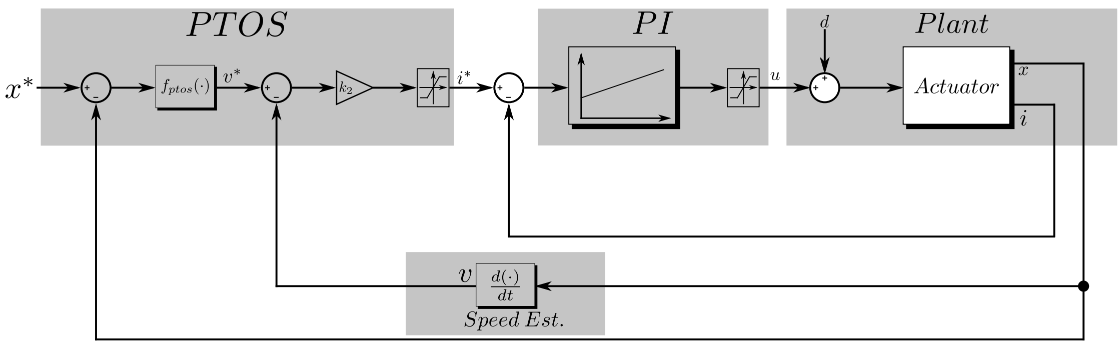

Figure 6.11: Cascaded PTOS position and speed controller, and current PI controller.

Another reason for implementing the PTOS controller is sensorless control. The PTOS controller enforces a maximum input during the acceleration phase. Since the position of the mover is not observable at zero speed, by applying full acceleration at the start, the EKF is able to estimate the speed and the position after a short time duration.

6.3 Experimental Results

The two controllers presented before were implemented on the control system, once by using the position sensor signal directly as feedback and once by using the estimated position signal instead.

6.3.1 Position Control with Position Sensor

Figures 6.12 and 6.13 show a comparison of the results of the LQR and PTOS controller for the up and down cycles respectively.

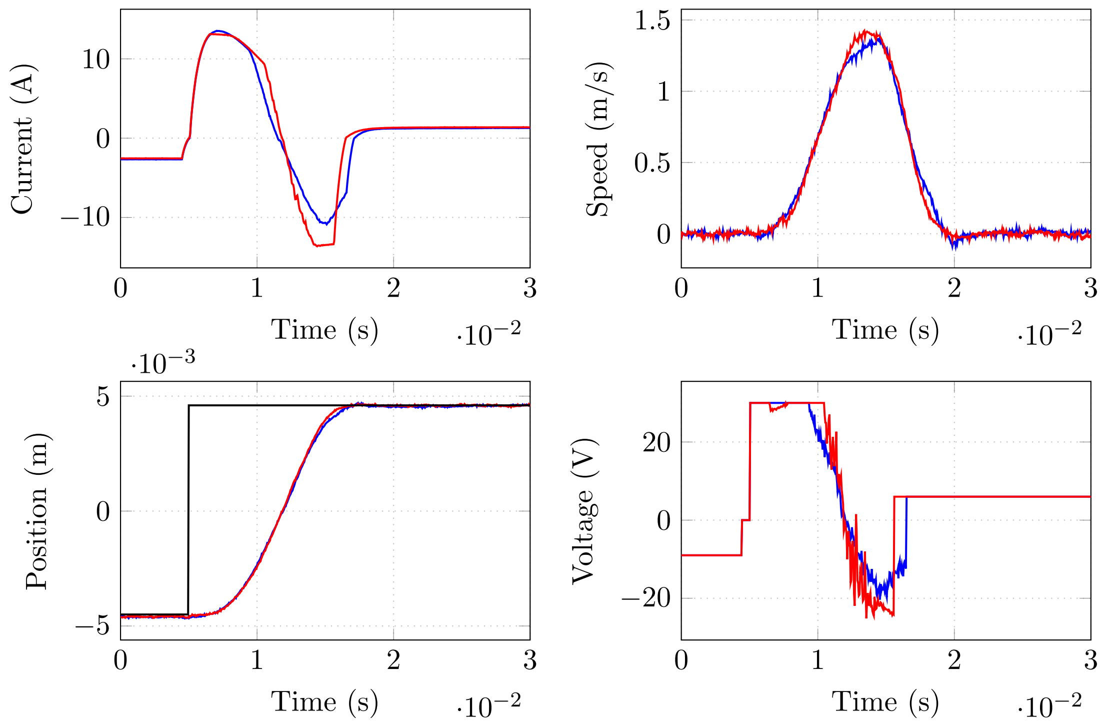

Figure 6.12: Comparison of the results of the two controllers for the up cycle (PTOS in red, LQR in blue, position reference in black).

The performance of both controllers is very close. This is due to a limitation on the current from the voltage source inverter. The PTOS controller is more dynamic which leads to faster transition time on the expense of more ripple in the voltage. The PTOS

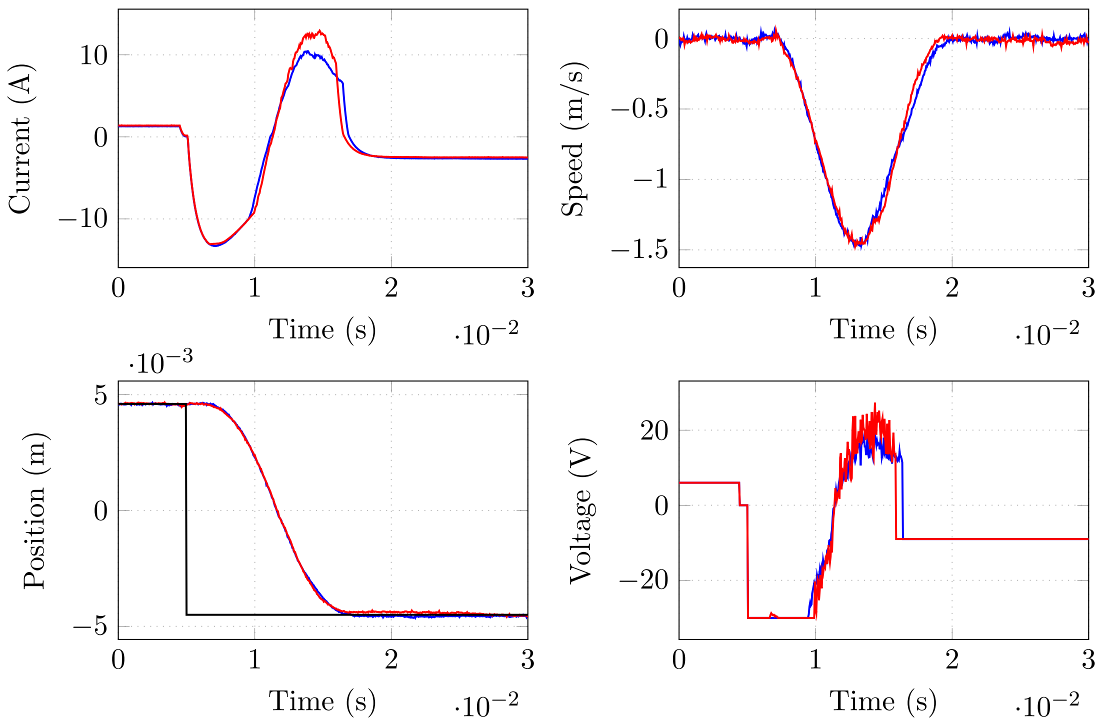

Figure 6.13: Comparison of the results of the two controllers for the down cycle (PTOS in red, LQR in blue, position reference in black).

controller uses the limits of the current and voltage more than the LQR controller. This can be seen during the acceleration and deceleration phases in the current and voltage waveforms.

6.3.2 Position Control without Position Sensor

Figures 6.14 shows the results of the LQG controller and PTOS controller with position estimation feedback, with no external load acting on the actuator. The two top plots show the reference and measured position and the two bottom plots show the error between the reference and measured position, for the up and down transition cycles.

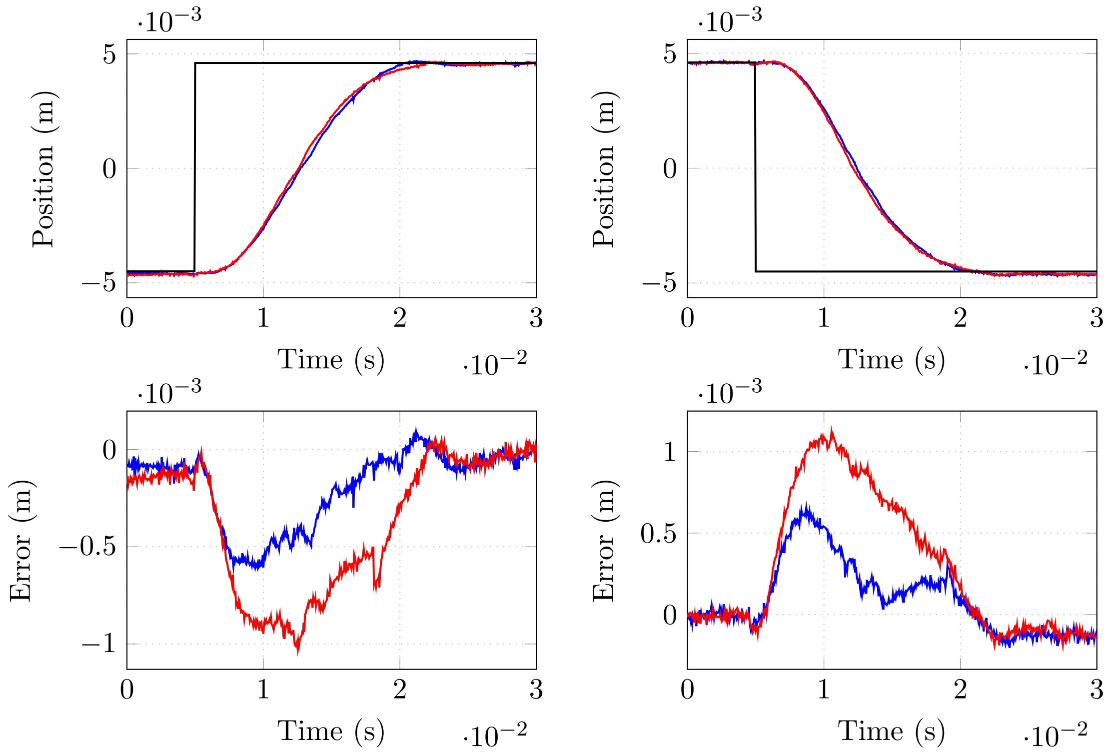

Figure 6.14: Comparison of the two controllers with estimated position as feedback (PTOS in red, LQR in blue, position reference in black).

Since the design of the controller is independent from the design of the observer, it was expected that the results would be close. For the up cycle, the maximum error between the measured and estimated position for the LQR controller was 0.612 mm and the PTOS controller 1.019 mm, while for the down cycle the maximum error was 0.654 mm and 1.116 mm for the LQR and PTOS respectively.

These results show the potential of the state observer in estimating the position of the mover during the transient phase. Even though at the start and end of the actuation the speed is minimal, the back e.m.f. is still strong enough to be able to estimate the speed of the mover and derive the position from the speed.

The limitations of the implemented state observer are mainly: assumption of the linear model and load disturbance. As was shown in the modelling section, the model of the actuator is highly nonlinear especially with the force and back e.m.f. constants and the cogging and reluctance forces. To identify the nonlinear model of the actuator, better measurement equipment would be needed as well as a more linear voltage source, in addition to system identification methods for nonlinear systems. The other limitation of the state observer is the load disturbance, which was not taken into account in the mechanical model. Should the load profile be known before hand, this can be added into the model of the state observer.

7 Conclusion and Future Work

In this project, control and position estimation for linear electromagnetic actuators with permanent magnets was investigated. First, a hybrid modelling methodology was adopted to model such kind of actuators where a combination of analytical and FEM modelling of the actuator was performed. After that, the electrical, magnetic, and mechanical parameters of the real actuators were measured and identified. A new method, based on measurement of the current switching instant was developed to measure the electrical parameters online, during the stop phase (zero speed) of actuation. The magnetic and mechanical parameters were calculated offline based on position, current, and reference voltage measurements.

After the parameters were identified, two controllers were investigated, the Linear Quadratic Regulator (LQR) controller and the Proximate Time Optimal controller for Servomechanisms (PTOS). The PTOS controller is a nonlinear type of controller based on the principle of time optimal control. It solves the drawbacks of time optimal control such chattering and steady state error with small increase in the transition time. Compared to the LQR controller it is more dynamic and utilizes the constraints on the input voltage and current better, on the expense of having a more noisy voltage reference (this could be an issue in EMC sensitive applications).

The Luenberger observer, which is a state observer of the predictor corrector type was implemented to estimate the speed of the mover based on the calculated voltage reference, measured current, and a simplified linear model of the actuator. The results have shown that the estimator can well estimate the speed of the mover during the transient state. This is due to the strong back e.m.f. signal. The speed signal is then mainly integrated to get the position signal. The estimator suffers from two limitations: assumptions of linear model and load disturbance estimation.

The work done in this project has a potential effect in the industry by addressing two points: position sensors and low cost microcontrollers.

Position sensors are expensive, add complexity to the system, and suffer from mechanical wear. An actuator control system can in theory operate in open loop control without a position sensor (On/Off operation) with the drawback of having a high impact speed which leads to fast mechanical wear of the actuator. In this project, a solution is proposed which combines position estimation with feedback control to minimize impact speeds.

The controllers developed in this work are simple enough to run on low cost microcontrollers. In addition to that, current measurement at the switching instant is very common in the industry in the field of field oriented control (FOC) for brushless DC motors (BLDC). Thus the method developed for electrical parameter estimation can be implemented on a low cost microcontroller. Since the exponential function is expensive (from a computation point of view), the exponential model can be approximated with the second order Taylor series approximation.

The future work for this topic will focus on improving the controller and estimator through the following points:

- Implement Proximate Time Optimal control for the triple integrator plant which can better utilize the constraints on the voltage and current
- Identify the nonlinear parameters of the actuator and use in the state estimator
- Investigate other types of nonlinear control such as Model Predictive Control (MPC)

Bibliography

[1] A. Flockett. How does a linear induction motor (lim) work? February 2017. URL: https://www.engineeringspecifier.com/drives-motors/how-does-a-linear-induction-motor-lim-work.

[2] R. R. Chladny and C. R. Koch. Flatness-based tracking of an electromechanical variable valve timing actuator with disturbance observer feedforward compensation. *IEEE Transactions on Control Systems Technology*, 16(4):652–663, July 2008. doi:10.1109/TCST.2007.912121.

[3] LG. Lg refrigerator with inverter linear compressor earns industry recognition. April 2014. URL: http://www.lgnewsroom.com/2014/04/lg-refrigerator-with-inverter-linear-compressor-earns-industry-recognition/.

[4] W. Commons. File:relay principle vertical.jpg — wikimedia commons, the free media repository, 2017. [Online; accessed 26-October-2018]. URL: https://commons.wikimedia.org/w/index.php?title=File:Relay_principle_vertical.jpg&oldid=254694313.

[5] D. Wiedemann. *Permanent Magnet Reluctance Actuators for Vibration Testing.* Dissertation, Technische Universitt Mnchen, Mnchen, 2013.

[6] Actuate. (n.d.). Retrieved March 1, 2018, from https://www.merriam-webster.com/dictionary/actuate.

[7] Williams fw15c renault, 2017. [Online; accessed 23-March-2018]. URL: http://www.ultimatecarpage.com/car/1241/Williams-FW15C-Renault.html.

[8] P. Upadhayay. How many electric motors are in a car?, 2016. [Online; accessed 1-March-2018]. URL: http://etn-demeter.eu/how-many-electric-motors-are-in-a-car/.

[9] W. Commons. File:engine movingparts.jpg — wikimedia commons, the free media repository, 2017. [Online; accessed 2-March-2018]. URL: https://commons.wikimedia.org/w/index.php?title=File:Engine_movingparts.jpg&oldid=236108620.

[10] S. Mraz. Eco-friendly hydraulic shock absorbers, August 2013. [Online; accessed 23-March-2018]. URL: http://www.machinedesign.com/hydraulics/eco-friendly-hydraulic-shock-absorbers.

[11] B. Hanson and M. Levesley. Self-sensing applications for electromagnetic actuators. *Sensors and Actuators A: Physical*, 116(2):345 – 351, 2004. URL: http://www.sciencedirect.com/science/article/pii/S0924424704003206, doi:http://dx.doi.org/10.1016/j.sna.2004.05.003.

[12] S. Paul and R. Paul. *Grundlagen der Elektrotechnik und Elektronik 2: Elektromagnetische Felder und ihre Anwendungen.* Springer, 2012.

[13] D. Schröder. *Elektrische Antriebe - Grundlagen.* Springer, 2013.

[14] M.-J. Chung and D.-G. Gweon. Optimal design and development of electromagnetic linear actuator for mass flow controller. *KSME International Journal*, 17(1):40–47, Jan 2003. URL: https://doi.org/10.1007/BF02984284, doi:10.1007/BF02984284.

[15] W. Hoffmann, K. Peterson, and A. Stefanopoulou. Iterative learning control for soft landing of electromechanical valve actuator in camless engines. *Control Systems Technology, IEEE Transactions on*, 11(2):174–184, Mar 2003. doi:10.1109/TCST.2003.809242.

[16] S. Chung, C. Koch, and A. Lynch. Flatness-based feedback control of an automotive solenoid valve. *Control Systems Technology, IEEE Transactions on*, 15(2):394–401, March 2007. doi:10.1109/TCST.2006.886440.

[17] A. Fabbrini, A. Garulli, and P. Mercorelli. A trajectory generation algorithm for optimal consumption in electromagnetic actuators. *Control Systems Technology, IEEE Transactions on*, 20(4):1025–1032, July 2012. doi:10.1109/TCST.2011.2159006.

[18] P. Mercorelli, K. Lehmann, and S. Liu. Robust flatness based control of an electromagnetic linear actuator using adaptive PID controller. In *Decision and Control, 2003. Proceedings. 42nd IEEE Conference on*, pages 3790–3795, Dec 2003. doi:10.1109/CDC.2003.1271739.

[19] S. Wendel, P. Lhdefink, M. Hoerner, A. Dietz, and R. Kennel. Dynamic model predictive position control for linear actuators in automotive applications. In *2018 Thirteenth International Conference on Ecological Vehicles and Renewable Energies (EVER)*, pages 1–6, April 2018. doi:10.1109/EVER.2018.8362362.

[20] P. Karamanakos, E. Liegmann, T. Geyer, and R. Kennel. Model predictive control of power electronic systems: Methods, results, and challenges. *IEEE Open Journal of Industry Applications*, 1:95–114, 2020. doi:10.1109/OJIA.2020.3020184.

[21] J. Rodriguez, M. P. Kazmierkowski, J. R. Espinoza, P. Zanchetta, H. Abu-Rub, H. A. Young, and C. A. Rojas. State of the art of finite control set model predictive control in power electronics. *IEEE Transactions on Industrial Informatics*, 9(2):1003–1016, May 2013. doi:10.1109/TII.2012.2221469.

[22] W. Commons. File:vectorbd.jpg — wikimedia commons, the free media repository, 2017. [Online; accessed 29-October-2018]. URL: `https://commons.wikimedia.org/w/index.php?title=File:VectorBD.jpg&oldid=230715626`.

[23] D. Byrd. Closed-loop motor control: An introduction to rotary resolvers and encoders. *Precision Data Converters, Texas Instruments*, 2014. URL: `http://www.ti.com/lit/an/slyt568/slyt568.pdf`.

[24] P. Jansen and R. Lorenz. Transducerless position and velocity estimation in induction and salient ac machines. *Industry Applications, IEEE Transactions on*, 31(2):240–247, Mar 1995. `doi:10.1109/28.370269`.

[25] M. Corley and R. Lorenz. Rotor position and velocity estimation for a salient-pole permanent magnet synchronous machine at standstill and high speeds. *Industry Applications, IEEE Transactions on*, 34(4):784–789, Jul 1998. `doi:10.1109/28.703973`.

[26] D. G. Luenberger. Observing the state of a linear system. *IEEE Transactions on Military Electronics*, 8(2):74–80, April 1964. `doi:10.1109/TME.1964.4323124`.

[27] S. Bolognani, R. Oboe, and M. Zigliotto. Sensorless full-digital pmsm drive with ekf estimation of speed and rotor position. *IEEE Transactions on Industrial Electronics*, 46(1):184–191, Feb 1999. `doi:10.1109/41.744410`.

[28] R. Kumar, S. Das, P. Syam, and A. K. Chattopadhyay. Review on model reference adaptive system for sensorless vector control of induction motor drives. *IET Electric Power Applications*, 9(7):496–511, 2015. `doi:10.1049/iet-epa.2014.0220`.

[29] M. Schroedl. Sensorless control of ac machines at low speed and standstill based on the ldquo;inform rdquo; method. In *Industry Applications Conference, 1996. Thirty-First IAS Annual Meeting, IAS '96., Conference Record of the 1996 IEEE*, volume 1, pages 270–277 vol.1, Oct 1996. `doi:10.1109/IAS.1996.557028`.

[30] M. Linke, R. Kennel, and J. Holtz. Sensorless speed and position control of synchronous machines using alternating carrier injection. In *Electric Machines and Drives Conference, 2003. IEMDC'03. IEEE International*, volume 2, pages 1211–1217 vol.2, June 2003. `doi:10.1109/IEMDC.2003.1210394`.

[31] R. Bojoi, M. Pastorelli, J. Bottomley, P. Giangrande, and C. Gerada. Sensorless control of pm motor drives 2014; a technology status review. In *Electrical Machines Design Control and Diagnosis (WEMDCD), 2013 IEEE Workshop on*, pages 168–182, March 2013. `doi:10.1109/WEMDCD.2013.6525177`.

[32] M. Rahman, N. Cheung, and K. W. Lim. Position estimation in solenoid actuators. *Industry Applications, IEEE Transactions on*, 32(3):552–559, May 1996. UNSW, Sydney. `doi:10.1109/28.502166`.

[33] S.-T. Wu and W.-N. Chen. Self-sensing of a solenoid valve via phase detection. In *Advanced Intelligent Mechatronics, 2009. AIM 2009. IEEE/ASME International Conference on*, pages 1165–1170, July 2009. `doi:10.1109/AIM.2009.5229744`.

[34] J. Maridor, N. Katic, Y. Perriard, and D. Ladas. Sensorless position detection of a linear actuator using the resonance frequency. In *Electrical Machines and Systems, 2009. ICEMS 2009. International Conference on*, pages 1–6, Nov 2009. LAI, EPFL. `doi:10.1109/ICEMS.2009.5382641`.

[35] I. Dulk and T. Kovacshazy. A sensorless method for detecting spool position in solenoid actuators. *Carpathian Journal of Electronic and Computer Engineering*, pages 36–43, 2013. MIS, Budapest.

[36] T. Braun, J. Reuter, and J. Rudolph. Position observation for proportional solenoid valves by signal injection. In *7th IFAC Symposium on Mechatronic Systems (Mechatronics 2016)*, 2016.

[37] P. Mercorelli. A two-stage sliding-mode high-gain observer to reduce uncertainties and disturbances effects for sensorless control in automotive applications. *IEEE Transactions on Industrial Electronics*, 62(9):5929–5940, Sept 2015. `doi:10.1109/TIE.2015.2450725`.

[38] P. Mercorelli. A motion sensorless control for intake valves in combustion engines. *IEEE Transactions on Industrial Electronics*, PP(99):1–1, 2016. `doi:10.1109/TIE.2016.2598314`.

[39] M. I. BV. Actuator, 2010. URL: `https://register.epo.org/application?number=EP08766747&lng=en&tab=main`.

[40] D. Meeker. Magnetic circuit derivation of energy stored in a permanent magnet. April 2007. URL: `http://www.femm.info/wiki/pmenergy`.

[41] A. Shiri and A. Shoulaie. A new methodology for magnetic force calculations between planar spiral coils. *Progress In Electromagnetics Research*, PIER(95):39–57, 2009. `doi:10.2528/PIER09031608`.

[42] W. Robertson. *Modelling and design of magnetic levitation systems for vibration isolation*. PhD thesis, Faculty of Engineering, Computer and Mathematical Sciences School of M;echanical Engineering, November 2013.

[43] R. Ravaud, G. Lemarquand, S. Babic, V. Lemarquand, and C. Akyel. Cylindrical magnets and coils: Fields, forces, and inductances. *IEEE Transactions on Magnetics*, 46(9):3585–3590, Sept 2010. `doi:10.1109/TMAG.2010.2049026`.

[44] W. Robertson, B. Cazzolato, and A. Zander. A simplified force equation for coaxial cylindrical magnets and thin coils. *IEEE Transactions on Magnetics*, 47(8):2045–2049, Aug 2011. `doi:10.1109/TMAG.2011.2129524`.

[45] David Meeker, Ph.D. . Finite element method magnetics. URL: http://www.femm.info/.

[46] A. Namboodiri and H. S. Wani. Unipolar and bipolar pwm inverter. *International Journal for Innovative Research in Science and Technology*, 1(7):237–243, 2014. URL: http://www.ijirst.org/articles/IJIRSTV1I7111.pdf.

[47] Y. Ji, Y. Yang, J. Zhou, H. Ding, X. Guo, and S. Padmanaban. Control strategies of mitigating dead-time effect on power converters: An overview. *Electronics*, 8(2), 2019. URL: https://www.mdpi.com/2079-9292/8/2/196, doi:10.3390/electronics8020196.

[48] V. van Geffen. A study of friction models and friction compensation. 2009. URL: https://api.semanticscholar.org/CorpusID:9975924.

[49] A. Kebairi, M. Becherif, and M. E. Bagdouri. Overview on modeling of systems with friction: Application to diesel engine actuator. In *2011 IEEE Vehicle Power and Propulsion Conference*, pages 1–5, 2011. doi:10.1109/VPPC.2011.6043127.

[50] J.-S. Bae, J.-H. Hwang, J.-S. Park, and D.-G. Kwag. Modeling and experiments on eddy current damping caused by a permanent magnet in a conductive tube. *Journal of Mechanical Science and Technology*, 23:3024–3035, 11 2010. doi:10.1007/s12206-009-0819-0.

[51] K. Liang. A review of linear compressors for refrigeration. *International Journal of Refrigeration*, 84:253–273, 2017. URL: https://www.sciencedirect.com/science/article/pii/S0140700717303377, doi:https://doi.org/10.1016/j.ijrefrig.2017.08.015.

[52] M. Papoutsidakis, A. Chatzopoulos, and C. Drosos. Linear position sensors a brief guide of use of the most common types. *International Journal of Computer Applications*, 179:9–14, 03 2018. doi:10.5120/ijca2018916685.

[53] Y. Zhong and Y. Luo. Comparative study of single-loop control and cascade control of third-order object. *Procedia Engineering*, 15:783–787, 2011. CEIS 2011. URL: https://www.sciencedirect.com/science/article/pii/S187770581101647X, doi:https://doi.org/10.1016/j.proeng.2011.08.146.

[54] D. M. Soares, H. A. M. Calil, and R. M. Stephan. Cascade control vs full-state feedback. In *2019 IEEE 15th Brazilian Power Electronics Conference and 5th IEEE Southern Power Electronics Conference (COBEP/SPEC)*, pages 1–6, Dec 2019. doi:10.1109/COBEP/SPEC44138.2019.9065696.

[55] L. Biagiotti and C. Melchiorri. *Trajectory Planning for Automatic Machines and Robots*. Springer Berlin Heidelberg, 2008. doi:10.1007/978-3-540-85629-0.

[56] M. Fliess, J. Lvine, and P. Rouchon. Flatness and defect of nonlinear systems: Introductory theory and examples. *International Journal of Control*, 61:1327–1361, 1995. doi:10.1080/00207179508921959.

[57] M. Zeitz. Differential flatness: A useful method also for linear SISO systems. *Automatisierungstechnik*, 58(1):5–14, 2010. URL: `http://dblp.uni-trier.de/db/journals/at/at58.html#Zeitz10`.

[58] X. Gong, Y. Hu, P. Sun, and H. Chen. A nonlinear feedforward-feedback controller design for electronic throttle based on flatness. In *Control and Decision Conference (CCDC), 2012 24th Chinese*, pages 1542–1547, May 2012. `doi:10.1109/CCDC.2012.6244249`.

[59] F. Suryawan, J. De Don, and M. Seron. Minimum-time trajectory generation for constrained linear systems using flatness and B-splines. *International Journal of Control*, 84(9):1565–1585, 2011. URL: `http://dx.doi.org/10.1080/00207179.2011.618514`, `arXiv:http://dx.doi.org/10.1080/00207179.2011.618514`, `doi:10.1080/00207179.2011.618514`.

[60] F. Antritter. On the relations between different flatness based design methods for tracking controllers. In *American Control Conference, 2008*, pages 1740–1745, June 2008. `doi:10.1109/ACC.2008.4586743`.

[61] L. Bittner. L. s. pontryagin, v. g. boltyanskii, r. v. gamkrelidze, e. f. mishechenko, the mathematical theory of optimal processes. viii + 360 s. new york/london 1962. john wiley & sons. preis 90/. *ZAMM - Journal of Applied Mathematics and Mechanics / Zeitschrift fr Angewandte Mathematik und Mechanik*, 43(10-11):514–515, 1963. URL: `https://onlinelibrary.wiley.com/doi/abs/10.1002/zamm.19630431023`, `arXiv:https://onlinelibrary.wiley.com/doi/pdf/10.1002/zamm.19630431023`, `doi:https://doi.org/10.1002/zamm.19630431023`.

[62] M. L. Workman, R. L. Kosut, and G. F. Franklin. Adaptive proximate time-optimal servomechanisms: Discrete-time case. In *26th IEEE Conference on Decision and Control*, volume 26, pages 1548–1553, 1987. `doi:10.1109/CDC.1987.272675`.

A Appendix

A.1 Exponential Model

In this section, the derivation of the exponential model (3.44) will be presented.

Starting with the model of an R-L circuit and assuming the speed of the actuator within one sampling is constant, the input $u(t) = U_{DC} - k_e \cdot v(t)$ can also be assumed constant $u(t) = U$. Thus the voltage equation becomes

$$R \cdot i(t) + L \cdot \frac{di}{dt} = U$$

Rearranging

$$\frac{di}{dt} \cdot \frac{1}{\frac{U}{R} - i(t)} = \frac{R}{L} \cdot dt$$

Integrating both sides

$$\int \frac{di}{dt} \cdot \frac{1}{\frac{U}{R} - i(t)} = \int \frac{R}{L} \cdot dt$$

results in

$$-ln|\frac{U}{R} - i(t)| = \frac{R}{L}t + C$$

Solving for i

$$i(t) = \frac{U}{R} \pm e^{-C} \cdot e^{-\frac{R}{L}t}$$

Let the initial value of the current be $i(0) = i_1$, then

$$i_1 = \frac{U}{R} \pm e^{-C}$$

or

$$\pm e^{-C} = i_1 - \frac{U}{R}$$

Then the current as a function of time and initial current becomes

$$i(t) = i_1 \cdot e^{-\frac{R}{L}t} + \frac{U}{R} - \frac{U}{R} \cdot e^{-\frac{R}{L}t}$$

A.2 Elliptic Integrals

As shown in Section 3.1.4.1 elliptic integrals are used in calculating the force experienced by a current carrying loop on another current carrying loop. Here a brief introduction on elliptic integrals is given.

Elliptic integrals are a class of integrals that arise in the calculation of the arc length of an ellipse and in many other problems in physics and mathematics. Unlike elementary integrals (such as those of polynomials, exponential functions, or trigonometric functions), elliptic integrals cannot be expressed in terms of elementary functions. Instead, they are classified into different types and are often related to elliptic functions.

A.2.1 General Form of Elliptic Integrals

Elliptic integrals generally involve the square root of a polynomial of degree 3 or 4 in the denominator. A typical form of an elliptic integral is:

$$\int \frac{R(x, \sqrt{P(x)})}{Q(x)}\, dx$$

where $R(x, \sqrt{P(x)})$ is a rational function, and $P(x)$ is a polynomial of degree 3 or 4.

A.2.2 Types of Elliptic Integrals

Elliptic integrals are classified into three standard forms, called elliptic integrals of the first, second, and third kinds. These forms correspond to different mathematical and physical situations.

Elliptic Integral of the First Kind

The elliptic integral of the first kind $F(\phi, k)$ is defined as:

$$F(\phi, k) = \int_0^{\phi} \frac{d\theta}{\sqrt{1 - k^2 \sin^2 \theta}}$$

where ϕ is the amplitude and k is the elliptic modulus (a parameter between 0 and 1).

This integral arises when calculating the arc length of an ellipse, or when solving certain problems in mechanics, such as the motion of a simple pendulum.

Elliptic Integral of the Second Kind

The elliptic integral of the second kind $E(\phi, k)$ is defined as:

$$E(\phi, k) = \int_0^{\phi} \sqrt{1 - k^2 \sin^2 \theta}\, d\theta$$

This integral is also related to the arc length of an ellipse but comes up in different geometric and physical contexts, such as finding the length of the complete arc of an ellipse or in calculating the work done in certain mechanical systems.

Elliptic Integral of the Third Kind

The elliptic integral of the third kind $\Pi(n, \phi, k)$ is given by:

$$\Pi(n, \phi, k) = \int_0^{\phi} \frac{d\theta}{(1 + n \sin^2 \theta)\sqrt{1 - k^2 \sin^2 \theta}}$$

where n is an additional parameter known as the characteristic. This type of integral appears in more complex physical scenarios, such as calculating certain potential fields or electrostatic problems.

A.2.3 Complete Elliptic Integrals

When the upper limit ϕ of the integral is $\frac{\pi}{2}$, the elliptic integrals are called complete elliptic integrals:

- Complete elliptic integral of the first kind:

$$K(k) = F\left(\frac{\pi}{2}, k\right) = \int_0^{\frac{\pi}{2}} \frac{d\theta}{\sqrt{1 - k^2 \sin^2 \theta}}$$

- Complete elliptic integral of the second kind:

$$E(k) = E\left(\frac{\pi}{2}, k\right) = \int_0^{\frac{\pi}{2}} \sqrt{1 - k^2 \sin^2 \theta}\, d\theta$$

A.2.4 Applications

Elliptic integrals are important in various fields:

- Geometry: They are used to calculate arc lengths of ellipses and other curves.
- Mechanics: In the study of pendulum motion, the integral that describes the motion of a pendulum for large amplitudes is an elliptic integral of the first kind.
- Electromagnetism: Elliptic integrals describe potential fields around certain distributions of charges and in problems involving elliptic cylinders.
- Physics of waves: Elliptic integrals describe certain types of wave propagation and oscillation phenomena.